UNIVERSITY OF CALIFORNIA, SAN DIEGO

# The mechanisms of flash sintering of ZnO and $TiO_2$ based ceramics

A dissertation submitted in partial satisfaction of the
requirements for the degree Doctor of Philosophy

in

Materials Science and Engineering

by

Yuanyao Zhang

Committee in charge:

Professor Jian Luo, Chair
Professor Olivia Graeve
Professor Vitali Nesterenko
Professor Kenneth Vecchio
Professor Kesong Yang

2016

The Dissertation of Yuanyao Zhang is approved, and it is acceptable in quality and form for publication on microfilm and electronically:

_____

_____

_____

_____

_____

Chair

University of California, San Diego

2016

## DEDICATION

To Huaizhao Zhang, Yeli Wu and Dan Shao

## TABLE OF CONTENTS

## LIST OF FIGURES

## LIST OF TABLES

## ACKNOWLEDGEMENTS

First of all, I would like to appreciate my advisor, Dr. Jian Luo, for proving all the opportunities, financial supports, and great guidance. I was sincerely honored to meet and work with him. I shall never forget his endless advice and help. I would like to express the deepest gratitude to my other committee members: Dr. Olivia Graeve, Dr. Vitali Nesterenko, Dr. Kenneth Vecchio, and Dr. Kesong Yang for their time and guidance.

Secondly, I would like to acknowledge my collaborators and co-authors in UCSD, Prof. Kenneth Vecchio, Dr. Tao Hu, Dr. Shengfeng Yang, Jiuyuan Nie, Joshua Gild, Jiajia Huang, Naixie Zhou, Jonathan Chan, Tyler Harrington, Mojtaba Samiee, and Zane Rice, with whom I had many useful and stimulating discussions. I'm also grateful to all my group mates who have helped and inspired me in many ways.

Finally, I would like to express my special thanks to my collaborators and co-authors, Dr. Jae-Il Jung at Ulsan National Institute of Science & Technology, Hantian Gao and Dr. Leonard Brillson at Ohio State University, Dr. Zhiyang Yu, Denise Yin, and Dr. Martin Harmer at Lehigh University for their invaluable help throughout the projects.

I would like to acknowledge the financial support from Aerospace Materials for Extreme Environments Program of the U.S. Air Force Office of Scientific Research (AFOSR) under the grants No. FA9550-10-1-0185 (05/2010

– 04/2013) and No. FA9550-14-1-0174 (09/2014 – 08/2019), and U.S. Office of Naval Research, under a MURI Grant (No. N00014-11-1-0678).

For the last but not least, my deepest gratitude goes to my parents Huaizhao Zhang and Yeli Wu for their love, patience and never-ending support. I specially thank to my fiancée, Dan Shao, for her endless support and encouragement during my Ph.D.

Chapter 3, in part, is a reprint of the material “Thermal Runaway, Flash Sintering and Asymmetrical Microstructural Development of ZnO and ZnO-$Bi_2O_3$ under Direct Currents” as it appears in the Acta Materialia, Yuanyao Zhang, Jae-Il Jung, and Jian Luo, Acta Materialia, 2015, 94, 87-100. The dissertation author was the primary investigator and author of this paper. All experiments and data analysis were performed by the author except for some SEM images.

Chapter 4, in full, is a reprint of the material “Promoting the flash sintering of ZnO in reduced atmospheres to achieve nearly full densities at furnace temperatures of <120 ºC” as it appears in the Scripta Materialia, Yuanyao Zhang, and Jian Luo, Scripta Materialia, 2015, 106, 26-29. The dissertation author was the primary investigator and author of this paper. All experiments and data analysis were performed by the author.

Chapter 5, in full, is a reprint of the material “Effects of Phase and Doping on Flash Sintering of $TiO_2$” as it appears in the Journal of Ceramic Society of Japan, Yuanyao Zhang, Jiuyuan Nie, and Jian Luo, Journal of Ceramic Society of Japan, 2016, 124, 296-300. The dissertation author was the primary

investigator and author of this paper. All experiments and data analysis were performed by the author except for the powder specimen preparation.

Chapter 6, in full, is currently in preparation for submission for publication "Probing the densification mechanisms during flash sintering of ZnO" Yuanyao Zhang, Jiuyuan Nie, Jonathan Michael Chan, and Jian Luo. The dissertation author was the primary investigator and author of this paper. All experiments and data analysis were performed by the author except for the powder specimen preparation.

Chapter 7, in full, is a reprint of the material "Observation of an unusual case of triple-line wetting by a gas phase" as it appears in the Scripta Materialia, Yuanyao Zhang, and Jian Luo, Scripta Materialia, 2014, 88, 45-48. The dissertation author was the primary investigator and author of this paper. All experiments and data analysis were performed by the author.

## VITA

| | | |
|---|---|---|
| 2009 | B.S. | Wuhan University of Technology, China |
| 2009-2011 | Process Engineer | Yangtze Optical Fibre and Cable Company, China |
| 2014 | M.S. | University of California, San Diego, USA |
| 2016 | Ph.D. | University of California, San Diego, USA |

## PUBLICATIONS

1. **Y. Zhang**, J. Nie, J. Chan, and J. Luo, “Probing the densification mechanisms during flash sintering of ZnO,” in preparation.

2. J. Gild, **Y. Zhang**, T. Harrington, K. Vecchio, and J. Luo, “High-entropy metal diborides: a new class of high-entropy materials and a new type of ultrahigh temperature ceramics,” *Scientific Reports* (submitted)

3. L. Brillson, W. Ruane, H. Gao, **Y. Zhang**, J. Luo, H. Wenckstern, and M. Grundmann, “Spatially-resolved cathodoluminescence spectroscopy of ZnO defects,” *Materials Science in Semiconductor Processing,* (submitted)

4. H. Gao, T. Asel, J. Cox, **Y. Zhang**, J. Luo, and L. Brillson, “Native point defect formation in flash sintered ZnO studied by depth-resolved cathodoluminescence spectroscopy,” *Journal of Applied Physics*, 120: 105302 (2016)

5. **Y. Zhang,** J. Nie, and J. Luo, “Effects of phase and doping on flash sintering of $TiO_2$,” *Journal of Ceramic Society of Japan,* 124: 296-300 (2016)

6. W. Cao, C. Marvel, D. Yin, **Y. Zhang**, P. Cantwell, M. Harmer, J. Luo, and R. Vinci, “Correlations between microstructure, fracture morphology, and fracture toughness of Ni-W alloys,” *Scripta Materialia*, 113: 84-88 (2016)

7. **Y. Zhang** and J. Luo, “Promoting the flash sintering of ZnO in reduced atmospheres to achieve nearly full densities at furnace temperatures of <120 ºC,” *Scipta Materialia*, 106: 26-29 (2015)

8. **Y. Zhang**, J. Jung and J. Luo, “Thermal Runaway, flash Sintering and asymmetrical microstructural development of ZnO and ZnO-$Bi_2O_3$ under direct currents,” *Acta Materialia*, 94: 87-100 (2015)

9. **Y. Zhang** and J. Luo, “Observation of an unusual case of triple-line wetting by a gas phase,” *Scripta Materialia*, 88: 45-48 (2014)

## ABSTRACT OF THE DISSERTATION

The mechanisms of flash sintering of ZnO and $TiO_2$ based ceramics

by

Yuanyao Zhang

Doctor of Philosophy in Materials Science and Engineering

University of California, San Diego, 2016

Professor Jian Luo, Chair

Flash sintering of ZnO, $TiO_2$ and a few other oxide systems has been investigated. A quantitative model has been developed to forecast the thermal runaway conditions. The predicted thermal runaway temperatures from the measured conductivities are in excellent agreements with the observed onset flash temperatures for at least 15 cases with different base materials, doping and surface treatments, particle sizes, and sintering atmospheres, attesting that the "flash" starts as a thermal runaway.

Specifically, using ZnO as a model system, a strong dependence of the onset flash sintering temperature on the atmosphere has been discovered. In a set of optimized conditions, ZnO specimens have been sintered to >97% relative densities in ~30 s at furnace temperatures of <120 °C in Ar + 5 mol. % $H_2$, with uniform microstructures and fine grain sizes of ~1 um. The enhanced conductivities of ZnO powder specimens in reduced atmospheres are responsible for the substantial decreases of the onset flash sintering temperatures.

More recently, using ZnO as a model system, the densification mechanisms of flash sintering are investigated. Controlled experiments via limiting the maximum current or the effective ramp rate suggest that both the maximum specimen temperature (determined by the Joule heating) and the high heating rate (on the order of 200 °C/sec) have major effects in densification during flash sintering. Moreover, rapid thermal annealing (RTA) experiments have been conducted to mimic the heating profiles in flash sintering, which achieved similar densification rates and grain growth as the flash sintering (with similar heating profiles between flash sintering and RTA). The combination of these experiments suggest that, at least for ZnO, the rapid heat profile is the key for high densification rates in flash sintering, while a number of electric field/current effects should exist.

Observation of an unusual case of triple-line wetting by a gas phase is discussed. The Bi vapor penetrates along the triple lines in the electrodeposited Ni to form open channels at 800 and 900 °C. This is interpreted as a case of

triple-line wetting by a gas phase, which has never been reported before. This unusual wetting phenomenon is related to the formation of a bilayer complexion and grain boundary embrittlement in the Ni-Bi system [Science 333: 1730 (2011)]. Further controlled experiments using high-purity Ni specimens with and without S doping suggest that the presence of S impurities is essential for the occurrence of this wetting phenomenon. This discovery has practical importance for understanding and controlling the microstructural stability and corrosion resistance.

# Chapter 1. Introduction

## 1.1. Introduction of sintering

Sintering has been part of human civilization since prehistoric times. It likely originated in the firing of clay into ceramic pottery. There are no records of the discovery; archeological findings show that the early use of sintering probably dates to about 24,000 BC [1, 2]. The earliest valuable sintered product of porcelain was found in China about 1,600 BC. Sintering of metallic items such as bronze, iron, gold, and silver has also been discovered dating from 3,000 BC found in mid-east [3, 4].

The terminology of “Sinter” was applied to describe mineral particle bonding, metallic bonding, and thermal bonding back from 1800s to 1900s [5]. After World War II, sintering became important because of military applications. Sintering techniques received 700 publications and 600 patents in 1943 according to US Library of Congress [4]. After that time, sintering was commonly to describe thermally induced particle bonding [6-9]

Sintering is the process of compacting and forming a solid mass of materials by heat and/or pressure without melting it to the point of liquefaction [10]. In another words, sintering is a thermal treatment for bonding particles into a coherent, predominantly solid, structure via mass transport events that often occur on the atomic scale. The bonding leads to improved strength and lower system energy [5].

Some terms are listed as follows: density is mass per unit volume,

theoretical density is porous free solid density, relative density is the ratio of measured density to the theoretical density, and green specimen represents specimen before sintering.

Sintering occurs through atomic diffusion at grain boundary and is achieved by heat treatment of powder compact in order to accelerate mass transport. Fig. 1.1 shows a typical example of different stages of sintering. Stage 1 represents green specimen before sintering, where the particles are just physically contacted. Stage 2 is a process of neck formation; individual particles are connected to form concave necks. In this stage, the structure is still very porous. Stage 3 is evolution of necks and grain boundaries as well as the elimination of pores; nevertheless, there is network of open pores. Stage 4 is the final stage in sintering. Open pores are isolated to form closed pores or are removed.

From the point of view of energy, sintering is a process where materials try to reduce free energy by decreasing surface area. This is named as the driving force in sintering. The driving force will reduce surface area to decrease free energy. This occurs between two or more particles, as shown in Fig. 1.1, by forming a “neck” between them [12-13].

Besides microstructure evolution such as neck formation, the sintering stage could also be divided into three different stages according to the relative density evolution during sintering, as shown in Fig. 1.2. In the initial stage, which corresponds to neck formation in microstructure evolution, there is only a ~3% relative density increase. The second or intermediate stage is where major

densification occurs. It covers stage 2 to 4 in the fig 1.1. The final stage is the last a few percentage of relative density increasing up to fully dense (roughly the last 7%-10%).

Grain growth is always accompanied with sintering; it is a natural process to lower surface free energy. However, densification rate is strongly dependent on the grain size, enlarged grain size could lower densification rate drastically [15]. This can be expressed as: $p \propto \frac{1}{d^n}$, *p* is densification rate, d is grain size and n depends on whether the densification rate is controlled by lattice diffusion (n=3) or by grain boundary diffusion (n=4). From this equation, if grain size doubled, the densification rate would reduce 8 times (lattice diffusion) or 16 times (grain boundary diffusion).

Grain size is also related to the materials mechanical and electrical properties [16-21]. For instance, enlarged grain size would dismiss the advantage of ultrafine grain or nanocrystalline materials that have some specific properties, e.g. strength, high specific volume [22, 23]. It is always a challenge to sinter materials with small grain size; there are a multitude of studies reporting many sintering methods to achieve this goal [24-28]. Likewise, literature inspection reveals that there is a vast body of studies focusing on the sintering of nanocrystalline materials. However, sintering of nanocrystalline materials still possesses great challenges and difficulties. In order to achieve fine grain size microstructure after sintering, a few things could be done. Firstly, high heating rate can skip the step of grain growth in low temperature. Keeping the grain size

relatively small at high temperature accelerates densification rate. Secondly, the addition of dopants to lower interfacial energy or reduce grain boundary mobility could lower grain growth driving force, thus preventing grain growth [29]. Thirdly, sintering with external pressure usually increases densification rate and results in smaller grains.

## 1.2. Sintering techniques

### 1.2.1. Conventional sintering

Conventional sintering method is a traditional sintering technique. That is, only temperature is controlled during the whole sintering process. The green specimen (powder compact) is placed in a furnace with a constant heating rate to a pre-set temperature and then isothermally annealed for a set amount of time. Sintering temperature is determined by the materials properties, usually at $0.5T_m$ to $T_m$, where $T_m$ is the melting temperature of the material. The appropriate temperature is crucial during sintering, which has effects on diffusion rate (densification rate) and misconstruction evolution. Besides temperature, initial particle size, purity, time, and heating rate also play important roles during sintering. Conventional sintering method could be applied in almost all the materials, including ceramics and metals.

### 1.2.2. Pressure assisted sintering

Pressure assisted sintering is also named as hot pressing. Additional pressure, which should have some effects on particle contact, is applied on the specimen during sintering process. Required sintering temperature could be

lowered in hot pressing compared with conventional sintering process [30]. The application of pressure during sintering leads various mass transport mechanisms, such as plastic yielding, diffusion control creep, and grain boundary sliding [31-32]. Hot pressing also affects microstructure evolution and it could be applied to make nanocrystalline materials [33-35].

Applied pressure could be varied from 20MPa to 8GPa [36, 37], it depends on the properties of equipment. For high temperature application, using graphite die the applied pressure is typically less than 100 MPa, even with tungsten carbide die, the pressure is typically less than 200 MPa. The ultra high pressure (more than GPa) could only be applied in low temperature, usually lower than 1000 °C. Hot pressing could also be divided into uni-axis hot pressing and hot isostatic pressing according to the direction of applied pressure. In hot isostatic pressing, the pressure is applied to the materials from all direction (hence the term “isostatic), and it can reach pressure of ~300 MPa with temperature lower than 1500 °C in most situations.

### 1.2.3. Field assisted sintering technology (FAST)

Field assisted sintering technology (FAST) also named as spark plasma sintering (SPS) [38], plasma-assisted sintering (PAS) [39], pulsed electric current sintering (PECS) [40], and electric pulse assisted consolidation (EPAC) [41], was developed in 1950s. The main characteristics of FAST is that the pulsed DC current passes through the graphite or tungsten carbide die and power compact to heat the material via joule heating, and pressure (<200 MPa in most situations)

is always applied during this process.

There are many advantages of FAST such as low sintering temperature, short holding time, and improvement of materials properties. Lower temperature and short time also affect microstructure evolution especially on grain growth. Tremendous amount of publications report fabrication of nanocrystalline materials using FAST. Many reports also mentioned that materials characteristics could be improved through FAST process, such as mechanical properties [42], oxidation and corrosion resistance [43], optical transmission [44], and electrical properties [45].

### 1.3. Flash sintering

In 2010, Raj and colleagues invented “flash sintering” [46, 47], in which they used an electric field (20-100 V/cm) to initiate rapid densification of 3YSZ (3 mol. % $Y_2O_3$-stabilized $ZrO_2$) in just a few seconds at hundreds of degrees below the normal sintering temperatures. Flash sintering differs from FAST because the applied electric field is typically higher, the sintering time is shorter, and the furnace temperature is lower. Thus, flash sintering can in principle be more cost-effective and energy-efficient. A comparison of time for sintering and furnace temperature between conventional sintering, hot press, SPS and flash sintering for 3YSZ was shown in Fig. 1.3. Sintering of 3YSZ needs ~1500 °C for hours, ~1200 °C for minutes to hours, ~1000 °C for minutes, and 850 °C for seconds in conventional sintering, hot press, SPS and flash sintering, respectively.

In flash sintering, a constant electric filed is applied on the heated

materials, Fig. 1.4 shows direct current (dc) electrical fields enhance the rate of sintering in yttria-stabilized zirconia (3YSZ). However, an instability occurs when the field is greater than a threshold value, estimated to be about 40 V/cm in the present experiments, leading to sintering in just a few seconds at unusually low temperatures. This kind of sintering process is called flash sintering [46]. The phenomenon of flash sintering also manifests in a power surge when the critical sintering temperature is reached, confirming that it is an instability in the process. The onset of the power instability coincides with the onset of flash sintering shown in Fig. 1.4.

Since 2010, flash sintering was demonstrated for 3YSZ (an ionic conductor) [47], 8YSZ (an ionic conductor) [48], $Co_2MnO_4$ (an electronic conductor) [49, 50], $La_{0.6}Sr_{0.4}Co_{0.2}Fe_{0.8}O_3$ (LSCF, a mixed ionic electronic conductor) [51], $SrTiO_3$ (a dielectric oxide) [52], MgO-doped $Al_2O_3$ (but not pure $Al_2O_3$) [53], $MnO_2$-doped $SnO_2$ (but not pure $SnO_2$) [54], SiC-$Al_2O_3$-$Y_2O_3$ (but not pure SiC or SiC-Al-$B_4C$-C) [55], $TiO_2$ [56], $Ce_{0.8}Gd_{0.2}O_{1.9}$ (GDC) [57], $Y_2O_3$ [58], and other materials. Not all the materials could be applied by flash sintering; there some limitations based on the materials properties, such as conductivity, heat capacity. Since flash sintering was invented a couple of years ago, it is still uncertain what kinds of materials could be applied by flash sintering. No one has yet set criteria for materials that would be suitable for flash sintering.

A mechanism for flash sintering must explain the simultaneous and discontinuous increases in mass transport kinetics and electrical conductivity. Originally, Raj *et al.* proposed three possible mechanisms [47]: flash sintering

may be related to:

1) Joule heating at grain boundaries that enhances grain boundary diffusion and electrical conductivity;

2) An avalanche nucleation of Frenkel pairs driven by the applied field;

3) A non-linear interaction between intrinsic fields (space charges at grain boundaries) and the applied field that produces “a catastrophic change in self-diffusion at grain boundaries” [47].

More recent studies attributed the rapid sintering to a combination of Joule heating and defect generation (including possibly unconventional avalanches of Frenkel defects) [46, 53, 58, 59] or enhanced ionic and electronic transport long selectively-heated (and even selectively-melted) grain boundaries and dislocations [60]; it was argued that that Joule heating alone is not sufficient for accounting for the observed fast densification [46, 53, 58, 59]. Chen and co-workers proposed electro-sintering of 8YSZ is due to ionomigration of pores resulting from surface diffusion of cations [61-63].

### 1.4. Motivations

While flash sintering has many technological advantages and potential applications, a systematic understanding of underlying mechanisms is crucial for the further development of this new sintering method and the selection of materials and processing recipes. There are some crucial and significant scientific questions that need to be answered in order to understand mechanism of flash sintering, as follows:

1. How does “flash” start? This question is related to the occurrence of flash sintering. Fig. 1.5 shows power increases abruptly at certain temperature and “flash” occurs in the same time. To answer this question, we want to understand the mechanism of onset of flash.
2. How does the densification occur/complete? In flash sintering, densification could be completed in just a few seconds; we want to know more about the densification mechanisms.
3. What are electric field/current (as well as non-equilibrium) effects on densification, grain growth/coarsening, microstructural development, etc.? The field effects on densification and microstructure evolution is open scientific questions. It is not only related to the flash sintering, but also plays an important role in SPS.

To answer the first question, we proposed a model to predict the thermal runaway temperature that is coincidental with the observed onset flash temperature, thereby attesting that the flash (at least) starts as thermal runaway [64-66]. This model has been tested in ZnO based system with different atmospheres and different grain size (including initial powder size difference and single crystal), in $TiO_2$ based system (different starting phases and dopants), and in 8YSZ. Similar thermal runaway models have been proposed by Todd et al. [67] and by Dong and Chen [68-70], which are based on the same physical concepts but used somewhat different mathematical approaches to solve the thermal runaway conditions (noting that the reports [67-70] from both groups were submitted after the initial submission, but before the publication, of our first report

of this quantitative thermal runaway model; thus, all three models have been developed independently). Several publications follow the same idea to test the onset flash temperature in their proposed materials [71]. This demonstrates that idea of thermal runaway as onset flash is well accepted.

As for the second question, Raj reported that estimated specimen temperature from Joule heating was not high enough to make densification completed in that short time [59]. There might be some other effects under electric field could affect densification rate such as Frenkel pairs, space charge layer, and local grain boundary heating. Majidi and Benthem reported that the shrinkage of particle agglomerates under noncontacting electric filed, which could exclude effects of Joule heating, was observed in an in-situ STEM [72]. However, we believe that densification mechanism is varied among materials properties. The electric field effect is different in ion-conductor and electron conductor materials. We are using ZnO (electron conductor, different from prior proposed ion-conductor of YSZ) as a model system to discuss the mechanisms of densification in flash sintering. An in situ shrinkage measurement of flash sintering was conducted in a modified dilatometer. Controlled experiments via limiting the maximum current or the effective ramp rate suggest that both the maximum specimen temperature (determined by the Joule heating) and the high heating rate (on the order of 200 °C/sec) have major effects in densification during flash sintering. Moreover, the shrinkage data is compared with densification rate in rapid thermal annealing, which excluded electric filed effects but had the same heating profile. We found that the densification rates and grain

size are almost the same in rapid thermal annealing and flash sintering at a similar specimen temperature. The combination of these experiments suggest that, at least for ZnO, the rapid heat profile is the key for high densification rates in flash sintering, while a number of electric field/current effects should exist.

With respect to the third questions, recent “two-electrode experiments” revealed interesting and intriguing observations of the field effects on grain growth [73]. Conrad and colleagues showed that a relatively weak applied DC or AC field could inhibit grain growth of 3YSZ significantly [74-78]. Consequently, sintering is enhanced because a smaller grain size provides a greater driving force. In a separate controlled experiment, Raj and colleagues also suggested that an applied modest DC field of ~4 V/cm can inhibit the grain growth in 3YSZ [79]. Two mechanisms have been proposed: Conrad explained this field phenomenon by the reduction in the grain boundary energy through interactions of the applied fields with the space charges near grain boundaries [76, 77]. An alternative explanation was that Joule heating at grain boundaries raised the local temperature and reduces grain boundary energy by an entropic effect; this not only reduced the driving force, but also created a pinning effect [79]. More recently, Chen and colleagues demonstrated that an applied electric current (of ~50 A/cm$^2$) could enhance the grain boundary mobility (by >10 times) in the cathode side discontinuously in 8YSZ, leading to abnormal grain growth [80]. They attributed this effect to the accumulation of supersaturated oxygen vacancies on the cathode side that caused cation reduction to lower its migration barrier [80]. We have observed a somewhat opposite effect: discontinuous

(abnormal) grain growth and/or coarsening in the anode side in ZnO during the flash sintering, which can be explained from the possible occurrence of an electric-potential-induced grain boundary (defect) structural transition by extending and combining Chen and colleagues' concept (discussed above) [80], Tuller's theory of grain boundary defect chemistry in ZnO [81], and the idea of grain boundary complexion transitions [82].

**Chapter 2** introduces the thermal runaway model we developed; it can predict onset flash sintering temperature and has been tested in the experiments in following chapters. **Chapter 3** discusses flash sintering on ZnO and ZnO-$Bi_2O_3$, and it includes model discussion and observation of interesting microstructure. **Chapter 4** is application of flash sintering in different atmosphere. In the best case, ZnO could achieve >97% of theoretically density at furnace temperature less than 120 °C. **Chapter 5** introduces flash sintering of $TiO_2$ in different starting phases (anatase and rutile), and different dopants (undoped, nitride doped and vanadium doped). **Chapter 6** discusses densification mechanisms in flash sintering; it shows temperature and rapid heating rate are the crucial points in flash sintering at least in ZnO. **Chapter 7** introduces another project I involved and it discussed observation of an unusual case of triple-line wetting by a gas phase. **Chapter 8** summarizes the work in this thesis and proposes the research plan for the future study.

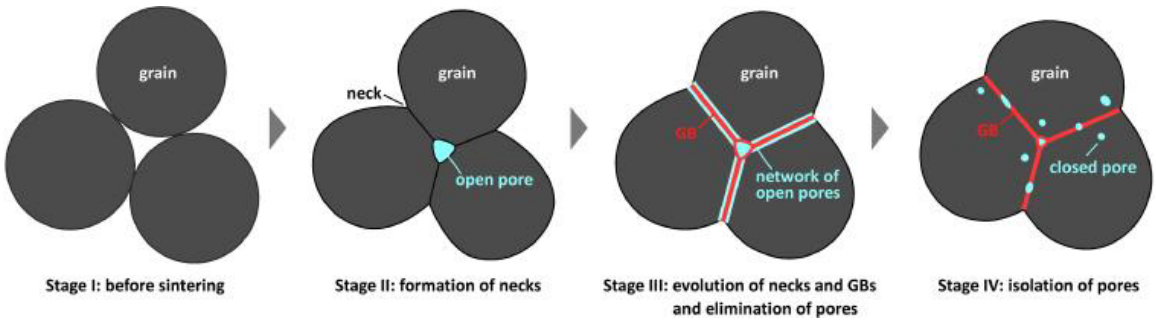


Figure 1.1 Three particles for showing different stages of Sintering [11].

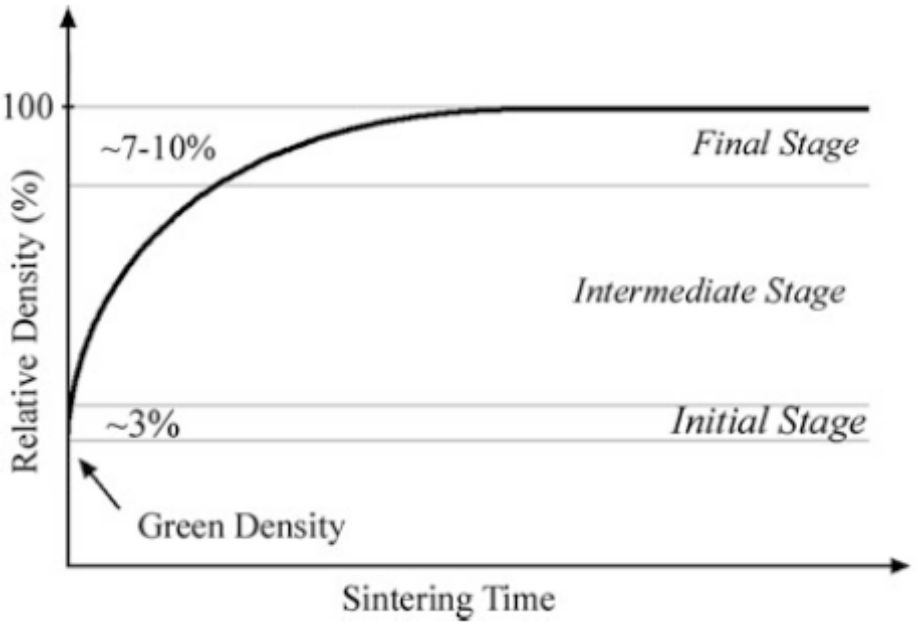


Figure 1.2 Densification curve vs. sintering time illustrates the stages of sintering. Green density represents the density of a compact before sintering starts. [14]

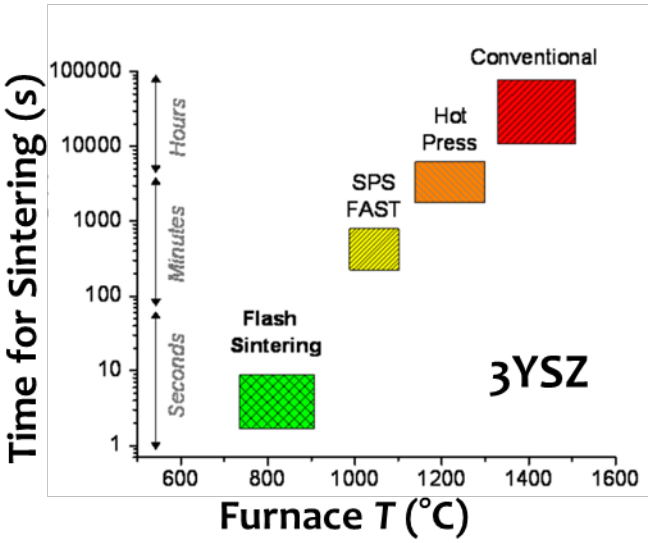


Figure 1.3 A comparison of time for sintering and furnace temperature between conventional sintering, hot press, SPS and flash sintering for 3YSZ. [Rishi Raj, University of Colorado]

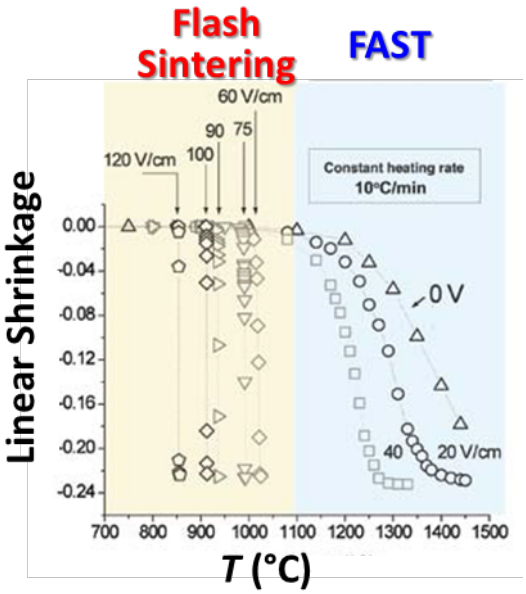


Figure 1.4 DC electrical fields enhance the rate of sintering in yttria-stabilized zirconia (3YSZ). This kind of sintering process is called flash sintering. Instability occurs when the field is greater than a threshold value, estimated to be about 40 V/cm in the present experiments, leading to sintering in just a few seconds at unusually low temperatures. [Image adapted from [47]]

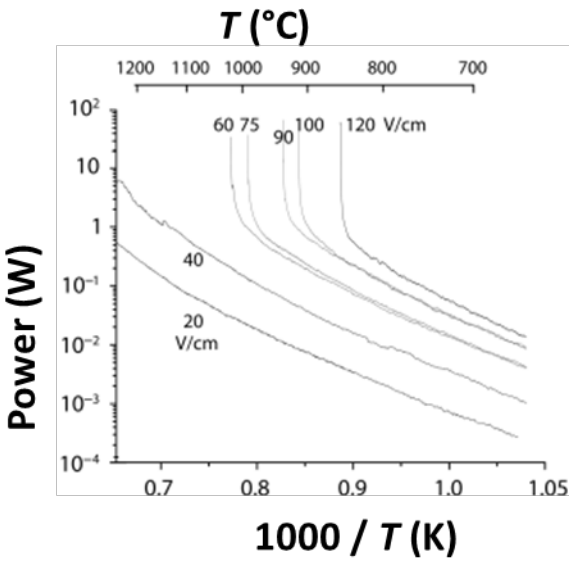


Figure 1.5 The phenomenon of flash sintering manifests in a power surge when the critical sintering temperature is reached, confirming that it is an instability in the process. The onset of the power instability coincides with the onset of flash sintering shown in Fig. 1.4. [Image adapted from [47]]

**References:**

[1] W.D. Kingery, Sintering from prehistoric times to the present, in: A.C.D. Chaklader, J.A. Lund (Eds.), Sintering '91, Trans Tech Publ., Brookfield, VT, 1992, pp. 1-10.

[2] J.E. Burke, A history of the development of a science of sintering, in: W.D. Kingery (Ed.), Ceramics and Civilization, Ancient Technology to Modern Science, vol. 1, Amer. Ceramic Society, Columbus, OH, 1985, pp. 315 -332.

[3] R.F. Mehl, The historical development of physical metallurgy, in: R.W. Cahn (Ed.), Physical Metallurgy, North Holland Publishing, Amsterdam, Netherlands, 1965, pp. 1-31.

[4] C.G. Goetzel, Treatise on Powder Metallurgy, vol. 1, Interscience Publishers, New York, NY, 1949, pp. 259-312.

[5] Sintering: from empirical observations to scientific principles / Randall German, New York: Elsevier Butterworth-Hein, 2014.

[6] B.F. Klugh, Trans. TMS-AIME 45 (1913) 330-345.

[7] F.A. Vogel, Trans. TMS-AIME 43 (1912) 381-386.

[8] J. Gayley, TMS-AIME 42 (1912) 180-190.

[9] D.W. Kingery, H.K. Bowen, and D.R. Uhlmann, Introduction to Ceramics (2nd ed.), (April 1976).

[10] "sinter, v." Oxford English Dictionary Second Edition on CD-ROM (v. 4.0) Oxford University Press 2009.

[11] H. Tanaka, A. Yamamoto, J. Shimoyama, H. Ogino, and K. Kishio, Supercond Sci Technol 25 (2012) 115022.

[12] Ricardo H.R. Castro, and Klaus van Benthem, Sintering, Mechanism of Convention Nanodensification and Field Assisted Processes, Springer, 2013.

[13] S.S. Indrakanti, V.F. Nesterenko, M.B, Maple, and N.A. Frederick, W.H. Yuhasz, and Shi Li, Philosophical Magazine Letters, 81 (2001) 849-857.

[14] S.L. Kang, Sintering: Densification, Grain Growth and Microstructure, Elsevier, 2005.

[15] J. Wang, and R. Raj, J. Am. Ceram. Soc. 73 (1990) 1172-1175.

[16] R. W. Siegel, S. Ramasamy, H. Hahn, L. Zongquan, L. Ting and R. Gronsky, J. Mater. Research. 3 (1988) 1367-1372.

[17] Z. Z. Fang, X. Wang, T. Ryu, K.S. Hwang, and H.Y. Sohn, International Journal of Refractory Metals and Hard Materials. 27 (2009) 288-299.

[18] T. El-Raghy, M. W. Barsoum, A. Zavaliangos, and S. R. Kalidindi, J. Am. Ceram. Soc. 82 (1999) 2855-2860.

[19] X.J. Chen, K.A. Khor, S.H. Chan and L.G. Yu, Mater. Sci. Eng. A 374 (2004) 64-71.

[20] L. Zhou, Z. Zhao, A. Zimmermann, F. Aldinger and M. Nygren, J. Am. Ceram. Soc. 87 (2004) 606-611.

[21] L. A. Stanicu, V. Y. Kodash, and J. R. Groza, Metall. Mater. Trans. A 32A (2001) 2633-2638.

[22] H. Gleiter, Progress. Mater. Sci. 33 (1989) 223-315.

[23] M.A. Meyer, A. Mishra, and D.J. Benson, Progress Mater. Sci. 51 (2006) 427-556.

[24] I.W. Chen, and X.H. Wang, Nature 404 (2000) 168-171.

[25] M. Park, and C. A. Schuh, Nat. Comm. 6 (2015)

[26] B. Sirinivasarao, K. Oh-Ishi, T. Ohkubo, and K. Hono, Acta Mater. 57 (2009) 3277-3286.

[27] H. Zhang, R. Gopalan, T. Mukai, and K. Hono, Scripta Mater. 53 (2005) 863-868.

[28] Z. Zhou, Y. Ma, J. Du, and J. Linke, Mater. Sci. and Eng. 505 (2009) 131-135.

[29] N. Zhou, and J. Luo, Materials Letters, 115 (2014) 268-271.

[30] R. Chaim, M. Levin, A. Shlayer, and C. Estournes, Advanced in Applied Ceramics, 107 (2008) 159-169.

[31] M. G. McKimpson, Mater. Manufac. Process, 11 (1996) 935–949.

[32] R. Suryanarayanan Iyer and S. M. L. Sastry, Acta Mater., 47 (1999) 3079–3098.

[33] H. Zhu and R. S. Averback: Mater. Sci. Eng. A, 1995, A204, 96–100.

[34] R. Chaim and M. Hefetz: J. Mater. Res., 13 (1998) 1875–1880.

[35] E. J. Gonzalez, B. Hockey and G. J. Piermarini: Mater. Manufact. Process., 1996, 11, 951–967.

[36] Y.J. He, J. Winnubst, H. Verweij, and J. Burggraaf, Mater. Sci. 12 (1994) 6505–6512.

[37] M.R. Gallas, R. Rosa, T.H. Costa, and H.D. Jornada, J. Mater. Res. 12 (2011) 764–768.

[38] M. Tokita, Mater. Sci. Forum, 83 (1999) 308–311.

[39] I.J. Shon and Z.A. Munir, Mater. Sci. Engin. A 202 (1995) 256-261.

[40] G. Xie, O. Ohashi, M. Song, K. Mitshushi, and K. Furuya, Appl. Surf. Sci. 241 (2005) 102-106.

[41] W.M. Goldberger, B. Merkle, and D. Boss, Adv. Powder Metall. Particulate

[42] M. Nygren and Z. Shen, Silicates Industr. 69 (2004) 211-218.

[43] B. Basu, J .H. Lee, and D.Y. Kim, J. Amer. Ceram. Soc. 87 (2004) 1771-1774.

[44] X. Su, P. Wang, W. Chen, Z. Shen, M. Nygren, Y. Cheng, and D. Yan, J. Mater. Sci., 39 (2004) 6257-6262.

[45] L. Zhou, Z. Zhao, A. Zimmermann, F. Aldinger, and M. Nygren, J. Amer. Ceram. Soc. 87 (2004) 606-611.

[46] R. Raj, M. Cologna, and J.S.C. Francis, J. Am. Ceram. Soc. 94 (2011) 1941-1965.

[47] M. Cologna, B. Rashkova, and R. Raj, J. Am. Ceram. Soc. 93 (2010) 3556-3559.

[48] M. Cologna, A.L.G. Prette, and R. Raj, J. Am. Ceram. Soc. 94 (2011) 316-319.

[49] A.L.G. Prette, M. Cologna, V. Sglavo, and R. Raj, J. Power Sources 196 (2011) 2061-2065.

[50] A. Gaur, and V.M. Sglavo, J. Eur. Ceram. Soc. 34 (2014) 2391-2400.

[51] A. Gaur, and V.M. Sglavo, J. Mater. Sci. 49 (2014) 6321-6332.

[52] A. Karakuscu, M. Cologna, D. Yarotski, J. Won, J.S.C. Francis, R. Raj, and B.P. Uberuaga, J. Am. Ceram. Soc. 95 (2012) 2531-2536.

[53] M. Cologna, J.S.C. Francis, and R. Raj, J. Eur. Ceram. Soc. 31 (2011) 2827-2837.

[54] R. Muccillo, and E.N.S. Muccillo, J. Eur. Ceram. Soc. 34 (2014) 915-923.

[55] E. Zapata-Solvas, S. Bonilla, P.R. Wilshaw, and R.I. Todd, J. Eur. Ceram. Soc. 33 (2013) 2811-2816.

[56] S.K. Jha, and R. Raj, J. Am. Ceram. Soc. 97 (2014) 527-534.

[57] X. Hao, Y. Liu, Z. Wang, J. Qiao, and K. Sun, J. Power Sources 210 (2012) 86-91.

[58] H. Yoshida, Y. Sakka, T. Yamamoto, J.-M. Lebrun, and R. Raj, J. Eur. Ceram. Soc. 34 (2014) 991-1000.

[59] R. Raj, J. Eur. Ceram. Soc. 32 (2012) 2293-2301.

[60] J. Narayan, Scr. Mater. 69 (2013) 107-111.

[61] S.-W. Kim, S.-J.L. Kang, and I.W. Chen, J. Am. Ceram. Soc. 96 (2013) 1090-1098.

[62] S.-W. Kim, S.-J.L. Kang, and I.W. Chen, J. Am. Ceram. Soc. 96 (2013) 1398-1406.

[63] I.W. Chen, S.-W. Kim, J. Li, S.-J.L. Kang, and F. Huang, Advanced Energy Materials 2 (2012) 1383-1389.

[64] Y. Zhang, J. Jung and J. Luo, Acta Materialia, 94 (2015) 87-100.

[65] Y. Zhang and J. Luo, Scipta Materialia, 106 (2015) 26-29.

[66] Y. Zhang, J. Nie, and J. Luo, Journal of Ceramic Society of Japan, 124 (2016) 296-300.

[67] R. I. Todd, E. Zapata-Solvas, R. S. Bonilla, T. Sneddon, and P. R. Wilshaw, J. Eur. Ceram. Soc., 35 (2015) 1865-1877.

[68] Y. Dong and I. W. Chen, J. Am. Ceram. Soc., 98 (2015) 2333-2335.

[69] Y. Dong and I. W. Chen, J. Am. Ceram. Soc. 98 (2015) 3624-3627.

[70] Y. Dong and I. W. Chen, J. Am. Ceram. Soc., in press (2016).

[71] J. G. P. D. Silvaa, H. A. Al-Qureshib, F. Keila, and R. Janssena, J Euro. Ceram. Soc. 36 (2016) 1261-1267.

[72] H. Majidi and K. V. Benthem, Phy. Rev, Letter, 114 (2015) 195503 1-5.

[73] R. Raj, M. Cologna, and J.S.C. Francis, J. Am. Ceram. Soc. 94 (2011) 1941-1965.

[74] H. Conrad, and D. Yang, Properties Microstructure and Processing 528 (2011) 8523-8529.

[75] D. Yang and H. Conrad, Microstructure and Processing 528 (2011) 1221-1225.

[76] J. Obare, W.D. Griffin, H. Conrad, J. Mater. Sci. 47 (2012) 5141-5147.

[77] H. Conrad, J. Am. Ceram. Soc. 94 (2011) 3641-3642.

[78] D. Yang and H. Conrad, Scr. Mater. 63 (2010) 328-331.

[79] S. Ghosh, A.H. Chokshi, P. Lee, and R. Raj, J. Am. Ceram. Soc. 92 (2009) 1856-1859.

[80] S.W. Kim, S.G. Kim, J.I. Jung, S.J.L. Kang, and I.W. Chen, J. Am. Ceram. Soc. 94 (2011) 4231-4238.

[81] H.L. Tuller, Journal of Electroceramics 4 (1999) 33-40.

[82] P.R. Cantwell, M. Tang, S.J. Dillon, J. Luo, G.S. Rohrer, and M.P. Harmer, Acta Mater. 62 (2014) 1-48.

## Chapter 2. A model to predict onset flash sintering temperature

### 2.1. Model description

A typical flash sintering process could be described as follow:

Firstly, the sample was put in the furnace with a constant heating ramp rate, and a constant electric field (voltage control mode) was applied on the specimen simultaneously. Secondly, at a certain point or temperature, the power source with a pre-set current limit switched from the voltage-control mode to a current-control mode because of electric conductivity increased and the resultant current reach a pre-set maximum value. This is the process of “flash” occurrence, and densification could be completed in seconds to minutes subsequently if an appropriate field and current limit are applied. The purpose of this model is to predict onset flash sintering temperature, where it could be expressed as figuring out the point/temperature when power source switched from voltage-control to current-control (equal as current reaches maximum).

We first present a model to predict the occurrence of a thermal (coupled with electric) runaway. We wish to point out that there are two fundamental scientific questions about the underlying mechanisms of the flash sintering, *i.e.*,

(1) How does the “flash” start?

(2) How do densification and sintering occur after the start of the flash?

The current modeling approach aims to address only the first (but not the second) question, which is an important open scientific question by itself.

We want to further emphasize that thermal runaway is one (but perhaps not the only) possible mechanism by which a flash can start. Yet, in the next chapters, we will show that the predicted thermal runaway temperatures are coincidental with observed onset flash temperatures for all ZnO based powder specimens in different atmospheres, ZnO single-crystal specimens, and $TiO_2$ based powder specimens with various doping, thereby suggesting that the flash indeed starts as thermal runaway in at least these ZnO and $TiO_2$ based specimens.

For a specimen under an applied electric field in a furnace, the rise of the specimen temperature is determined by the energy conservation law. The necessary and essential conditions for a stable temperature rise are:

$$\sigma(T_S)\cdot E^2\cdot V_S = \dot{Q}(T_S,T_F), \tag{2.1}$$

and

$$E^2 V_S \left.\frac{d\sigma}{dT}\right|_{T_S} \le \frac{\partial \dot{Q}(T_S,T_F)}{\partial T_S}, \tag{2.2}$$

where $T_S$ and $T_F$ are the specimen (S) and furnace (F) temperatures, respectively, $E$ is the applied electric field, and $V_S$ is the volume of the specimen. In Eq. (2.1), the left side, $\sigma(T_S)E^2V_S$, is the rate of heat generation from joule heating, whereas the right side, $\dot{Q}(T_S,T_F)$ is the rate of heat dissipation (including contributions from heat conduction, convection and radiation) that depends on the particular geometrical configuration and heat transfer environment. $\sigma(T)$ is the electric conductivity, which should include both the normal temperature-

dependent conductivity and any contribution from non-equilibrium defects generated by the flash process (if there is any).

The heat dissipation should vanish when $\Delta T \equiv T_S - T_F = 0$, while the left side of Eq. (2.1) is always positive. Eq. (2.2) represents the condition for a stable temperature rise. Thus, the specimen temperature will rise. Moreover, if a positive and finite solution of $T_F$ ($\Delta T$) exists for Eq. (2.1), the temperature rise is stable.

The thermal runaway condition (Eq. (2.3)) implies that an unstable arise of temperature will occur if more heat is generated than can be dissipated with an increase in the specimen temperature. In such a case, a temperature rise will lead to an increase in conductivity, which will subsequently increase electric power dissipation/heat generation and heat the specimen further in a positive feedback loop, which will essentially leads to a thermal runaway. A necessary condition for an unstable temperature rise (*a.k.a.* a thermal runaway) is given by:

$$E^2 V_S \left.\frac{d\sigma}{dT}\right|_{T_S} > \alpha, \tag{2.3}$$

where

$$\alpha \equiv \frac{\partial \dot{Q}(T_S, T_F)}{\partial T_S}, \tag{2.4}$$

is a general parameter that characterizes the increase of heat transfer (dissipation) rate with the increasing specimen temperature, and it can be quantified for heat conduction, convention, and radiation, if all heat transfer

parameters are known. This thermal runaway condition can be rewritten as:

$$\left.\frac{d\sigma}{dT}\right|_{T_S} > \frac{\alpha}{E^2 V_S}, \tag{2.5}$$

where the left side is a material property (which also depends on the microstructure) and the right side depends on the specimen geometry and other experimental conditions (the applied field and the specific heat dissipation environment).

We should also recognize the possibility that the left side of Eq. (2.3) ($E^2 V_S d\sigma/dT$) may fall below $\alpha$ again after first exceeding $\alpha$; in such a case, the thermal runaway will stop at a higher temperature where a stable thermal equilibrium is achieved. Such a case is theoretically possible. Thus, the full conditions for the occurrence of a coupled thermal and electric runaway are:

$$\begin{cases} \sigma(T_S) E^2 V_S = \dot{Q}(T_S, T_F) \\ E^2 V_S \left.\dfrac{d\sigma}{dT}\right|_{T_S} = \dfrac{\partial \dot{Q}(T_S, T_F)}{\partial T_S} \equiv \alpha \\ E^2 V_S \left.\dfrac{d^2\sigma}{dT^2}\right|_{T_S} > \dfrac{\partial \alpha}{\partial T_S} = \dfrac{\partial^2 \dot{Q}(T_S, T_F)}{\partial T_S^2} \end{cases}, \tag{2.6}$$

For a case of blackbody radiation (more discussion on chapter 3.3), a simple analytic equation exists:

$$\alpha = 4\sigma_{\text{Stefan}} T_S^3 A_S, \tag{2.7}$$

where $\sigma_{\text{Stefan}}$ (= $5.67 \times 10^{-8}$ W/m$^2$K$^4$) is the Stefan-Boltzmann constant, and $A_S$ is

the surface area of the specimen. It is interesting to note that $\alpha$ only depends on the specimen temperature ($T_S$) for this case (Eq. (2.7)), as well as cases where simple linear laws ($\dot{Q}(T_S,T_F)=K(T_S-T_F)$) for the heat conduction and convention are applicable and $K$ can be assumed only to depend on $T_S$ (but not $T_F$, which a valid approximation for small $\Delta T$). This allows Eq. (2.6) to be solved numerically by a graphic construction method, which will be described and implemented in the following section.

In this simplified case (that is used as an approximation for the current study), Eq. (2.6) is only a function of specimen temperature ($T_S$); thus, the coupled thermal and electric runaway condition can be determined by the following two conditions:

$$\begin{cases} E^2 V_S \left.\dfrac{d\sigma}{dT}\right|_{T_S} = \alpha \approx 4\sigma_{\text{Stefan}} T_S^3 A_s \\ E^2 V_S \left.\dfrac{d^2\sigma}{dT^2}\right|_{T_S} > \dfrac{d\alpha}{dT_S} \end{cases}, \tag{2.8}$$

The above equations can be solved graphically by plotting $E^2V_S(d\sigma/dT)_{T_S}$ and $4\sigma_{\text{Stefan}}T_S^3A_s$ vs. $T_S$ curves and finding their intersections to obtain the specimen temperature ($T_S$) at the onset flash/thermal runaway.

Thermal runaway will start if both Eq. (2.1) and Eq. (2.8) are satisfied simultaneously. In the current case where Eq. (2.8) is independent of the furnace temperature $T_F$, we can use Eq. (2.8) to first solve the specimen temperature $T_S$, and then use Eq. (2.1) to solve the furnace temperature $T_F$ from the specimen

temperature $T_S$. Thus, the actual solution (of $T_F$ and $T_S$) that we obtained via this procedure (used in the next chapters) will satisfy both Eq. (2.1) and Eq. (2.8) simultaneously; in other words, Eq. (2.1) is automatically satisfied by using this solution method that we adopted for our numerical analysis in the next chapters. In a more general case where Eq. (2.8) is a function of both $T_F$ and $T_S$, Eq. (2.1) and Eq., (2.8) should be used together to solve both $T_F$ and $T_S$ simultaneously.

In the next chapters, we will demonstrate that the above model can predict the thermal runaway temperatures of ZnO based powder specimens in different atmospheres, ZnO single-crystal specimens, and $TiO_2$ based powder specimens with various doping that are coincidental with the observed onset flash temperatures in all cases. The excellent agreements between the predictions and experiments ascertain the underlying hypothesis, *i.e.*, a flash event starts as a simple case of thermal runaway (without the need of avalanching non-equilibrium defects as previously assumed) at least for the case of ZnO; however, we emphasize that this does not exclude the possible formation of non-equilibrium defects after the occurrence of the flash/thermal runaway in the activated state to accelerate sintering (to achieve fast densification rates that do not appear to be possible from simple extrapolations of temperature-dependent sintering rates, as prior studies have demonstrated [1-4]) and affect microstructural development.

Specifically, we will use the experimentally-measured $\sigma(T)$ to predict the thermal runaway conditions and to compare them with the experimentally-measured onset flash temperatures in the next chapters. The excellent agreement between the predicted thermal runaway conditions and observed

onset flash temperatures is strong evidence to support that the flash starts as a thermal runaway in these systems.

We acknowledge that the current modeling approach aims to explain how flash starts, but does not provide mechanistic understanding of the densification during the flash sintering. In addition, the thermal runaway model presented here is phenomenological in terms that it works regardless whether the underlying conductivity $\sigma(T)$ is electronic or ionic. Nonetheless, the predictions are genuine without using of any free parameters (despite that we fit experimentally-measured $\sigma(T)$ to Arrhenius functions in the current cases of ZnO; we recognize that other $\sigma(T)$ functions may be needed for materials with non-Arrhenius behaviors).

**2.2. Model Discussion**

We are the first to report a model to predict onset flash sintering temperature, an other study was published simultaneously by Todd et al. in early 2015 [5] after the initial submission of this manuscript, where a similar thermal runaway model was proposed independently (with a slightly later submission date) to explain the occurrence of flash in 3YSZ (the most extensively studied flash sintering systems). Some other reports by Dong and Chen [6-7], and Silva et al. [8] were essentially based on the same physical concepts as our prior model, although the specific mathematical approaches (the specific equations and methods used) to solve the onset flash sintering (thermal runaway) temperatures are somewhat different.

Todd et al. [5]'s SU (static uniform) model is largely equivalent to the thermal runaway model presented here, although they formulated the criteria using slightly different equations and plot the "heating/cooling" diagrams differently. Todd et al. [5] also proposed a DNU (dynamic, non-uniform) model to explain the transit behaviors, particularly the incubation time, with success. 3YSZ is usually an ionic conductor (although the relevant conduction mechanisms can be different with the high field/current involved in the flash sintering, as discussed previously) and ZnO is an electronic conductor (a semiconductor self-doped with Zn interstitials and/or oxygen vacancies). The facts that similar thermal runaway models can be used to predict the onset of flash in both cases (as discussed in more details in the next section) demonstrates the general applicability of the thermal runaway mechanism for the start of flash beyond one system. Dong and Chen's model [6-7] introduced heat capacitance to calculate temperature evolution under additional applied electric power, and they also summarized their model in most of the reported flash sintered materials systems. It demonstrated that the model could be applied in most of materials that could be applied by flash sintering. Silva et al. reported a model involved the critical conditions for thermal runaway and a critical non-linear behavior after a threshold condition.

**References:**

[1] R. Raj, M. Cologna, and J.S.C. Francis, J. Am. Ceram. Soc. 94 (2011) 1941-1965.

[2] M. Cologna, J.S.C. Francis, and R. Raj, J. Eur. Ceram. Soc. 31 (2011) 2827-2837.

[3] H. Yoshida, Y. Sakka, T. Yamamoto, J.-M. Lebrun, and R. Raj, J. Eur. Ceram. Soc. 34 (2014) 991-1000.

[4] R. Raj, J. Eur. Ceram. Soc. 32 (2012) 2293-2301.

[5] R.I. Todd, E. Zapata-Solvas, R.S. Bonilla, T. Sneddon, and P.R. Wilshaw, J. Eur. Ceram. Soc. 35 (2015) 1865-1877.

[6] Y. Dong and I. W. Chen, J. Am. Ceram. Soc., 98 (2015) 2333-2335.

[7] Y. Dong and I. W. Chen, J. Am. Ceram. Soc. 98 (2015) 3624-3627.

[8] João Gustavo Pereira da Silva, Hazim Ali Al-Qureshi, Frerich Keil, and Rolf Janssen, J. Euro. Cera. Soc., 36 (2016) 1261-1267.

# Chapter 3. Flash sintering of powder specimen of ZnO, $Bi_2O_3$ doped ZnO and single crystal of ZnO

## 3.1. Introduction

Zinc Oxide (ZnO) is a very promising material for semiconductor device application [1-3], and it has a direct and wide band gap of 3.3 eV. It has many applications, such as transparent electrodes [4], varistors [5-6], piezoelectric devices [7], phosphors [8], transparent oxide thin film transistors [9] and spintronics [10].

Sintering is common method to make ZnO based varistor since sintering a cost effect method compared with thin/thick film deposition or other methods. More recently, flash sintering of nanocrystalline pure ZnO under AC fields between 0 and 160 V/cm was reported, where normal grain growth was observed [11]. In this chapter, we applied DC currents at a higher field of 300 V/cm to high-purity ZnO single crystals as well as pure, 2 wt. % $Al_2O_3$ doped ZnO and 0.5 mol. % $Bi_2O_3$-doped ZnO powder specimens. We have observed a number of interesting and intriguing phenomena, including the flash (thermal runaway) of ZnO single crystals, reduction of the onset flash temperature in powder specimens, anode-side abnormal grain growth (in contrast of the cathode-side abnormal grain growth reported for 8YSZ [12]), growth of aligned single-crystalline rods, and doping effects on deferring the onset flash sintering and homogenizing microstructures, which have greatly deepened and enriched our

fundamental understanding of the sintering and microstructural development under electric currents.

## 3.2. Experimental

### 3.2.1. Green pellets preparation

The pure and 0.5 mol. % $Bi_2O_3$-doped powder samples were fabricated by using purchased ZnO (Sigma Aldrich, St. Louis, Missouri, USA: >99.9% purity, <0.5 μm particle size, named as P1) and $Bi_2O_3$ (Sigma Aldrich: ≥99.8% purity, 90-210 nm particle size) powders. Nominally pure ZnO powders were ball milled with alumina media for 2 hours in isopropyl alcohol with 0.5 wt. % of binder (10 wt. % of polyvinyl alcohol or PVA dissolved in isopropyl alcohol).

To further test our model with high precision, we performed a second experiment on a new ZnO powder specimen with an improvement, and it is a high-purity ZnO powder (Sigma Aldrich, St. Louis, Missouri, USA: >99.99% purity; grain/particle size of the green specimen: 120 ± 50 nm, named as P2). This powder was divided into two groups, one group is without any heat treatment, and the other group is annealed at 800 °C for 8 hours in order to make the initial particle coarsening (grain/particle size of the green specimen after initial coarsening is ~ 700 nm) and the powder was hand granulated subsequently.

0.5 mol. % $Bi_2O_3$-doped ZnO powders (P1) were prepared by ball milling mixtures of the oxide powders and 0.5 wt. % of binder in isopropyl alcohol for 10 hours. All powders were subsequently dried in an oven chamber at 80 °C for 12 hours after milling. The 0.5 mol. % $Bi_2O_3$-doped ZnO powders were calcined at

600 °C for two hours in air in a covered Pt crucible, followed by another round of 2-hour ball milling in isopropyl alcohol with 0.5 wt. % of binder and subsequent drying. Dried pure and 0.5 mol. % $Bi_2O_3$-doped ZnO powder cakes were pulverized in a mortar and sieved under 150 mesh of sieve.

2 wt. % $Al_2O_3$ doped ZnO powder was purchased from US Research Nanomaterials, Inc (purity of 99.99+%, and grain size is 15 nm). $Al_2O_3$ doped ZnO (AZO) is a potential materials for transparent conductivity oxides (TCO) with the application of touch screen display, LED, and photovoltaic.

The resultant granulated powders were uniaxially pressed at ~300 MPa in a mold (¼ inch diameter) into green specimens (disks) with the approximate dimensions: *D* (diameter) = 6.4 mm and *H* (thickness) = 4 mm. The average bulk densities (± one standard deviations) of pure, 0.5 mol. % $Bi_2O_3$-doped ZnO and 2 wt.% $Al_2O_3$ doped ZnO green specimens were 63.5 ± 0.8 %, 65.0 ± 2.2 %, and 57.3 ± 0.2 % of the theoretical densities, respectively. The green specimens were then heated at the ramping rate of 5 °C per minute to 500 °C and baked at 500 °C isothermally for one hour to burn out the binders (except AZO, no binder was added).

After measuring the dimensions and weight of each sample (P1 powder and $Bi_2O_3$ doped ZnO), both sides of the specimen were pasted by Pt inks (Heraeus Inc, West Conshohocken, PA; catalog number: 116668009) with Pt wire buried underneath. The pasted specimens were then heated at the ramping rate of 20 °C per minute and baked at 500 °C for 20 minutes. This baking

process was repeated approximately eight times (to attach Pt wires firmly without going to a higher baking temperature to avoid any shrinkage of ZnO specimens) until the Pt wire was connected solidly to the dried Pt pastes.

The new ZnO powder specimen (P2 powder) and $Al_2O_3$ doped ZnO specimens were sputtered of platinum using Denton Discovery 18 Sputter System. The surrounding areas were slightly ground by SiC papers after sputtering.

### 3.2.2. Typical flash sintering

The electroded sample was placed close to the thermocouple within a tube furnace, with Pt wire connected to the power source. Each specimen was heated at the ramping rate of 5 °C per minute under an (initial) electric field at 300 V/cm (calculated based on the initial specimen thickness). Similar to a typical flash sintering experiment, the applied voltage was kept a constant until the resultant current reach a pre-set maximum value ($I_{max}$ = 1 and 4 A, respectively, for this study), at which point the power source switched from the voltage-control mode to a current-limited mode. The maximum current densities and final electric fields in the activated state were estimated based on the actual measured dimensions of sintered specimens are listed in Table 3.1, along with other experimental conditions and results. When the power density reached the maximum, the electric power source was kept on for an additional 30 seconds, with furnace being turned off (the furnace temperature did not change significantly with the 30 seconds). Then, the electric power was switched off and

the specimen was cooled down within the furnace. The weight and dimension of the sintered specimens were measured to obtain the final bulk density.

High-purity ZnO single crystals (>99.99% purity, 5 mm $\times$ 5 mm $\times$ 0.5 mm, double-side polished) were purchased from MTI Corporation (Richmond, California, USA). Platinum was sputtered on the both sides of the single crystal specimens using a Denton Discovery 18 Sputter System. The surrounding areas (sides of the single crystals) were slightly ground by SiC papers after sputtering. The specimen was placed in a horizontal tube furnace and attached with Pt wires on both sides to apply a 300 V/cm electric field to conduct a benchmark experiment with identical heating scheme as the powder specimens. The maximum allowed currents ($I_{max}$) were again set to be 1 and 4 A, respectively, although the actual current only reached ~1.45 A in the latter case.

### 3.2.3. Characterization

Scanning electron microscopy (SEM) was carried out using a field-emission microscope (Hitachi SU6600, Japan) to characterize the microstructures. Grain sizes were measured using a standard intercept method by drawing 30 lines in the vertical, horizontal and diagonal directions of the SEM micrographs (excluding the lengths of intercept sections with voids) and assuming a geometric factor 1.5 (for ideal spherical grains).

## 3.3. Results and discussion

### 3.3.1. Flash of ZnO single crystal

A main character of flash sintering is represented by abrupt and simultaneous increases in both the specimen temperature and the electric current. To establish a baseline, we measured the electric current and voltage as functions of furnace temperature and calculated the electric power/heat generation rates and conductivities for two ZnO single crystals with an (initial) applied electric field of 300 V/cm. Fig. 3.1 shows the nominal electric powder density (= the volumetric heat generation rate) vs. furnace temperature curves. For high-purity ZnO single crystals, the electric power density increased gradually and reached ~0.1W/mm3 at ~870 °C. A thermal runaway or "flash" occurred at $T_F$ = 870 °C and $T_F$ = 877 °C, respectively, for the two ZnO single crystals (Fig. 3.1; Table 3.1), where the electric power density increased abruptly to >1 W/mm3.

In the current experiments, it was difficult to directly measure the specimen temperature. Thus, we adopted an approach proposed by Raj *et al.* to estimate the specimen temperatures by the black body radiation model [13]:

$$T_S^4 - T_F^4 = \frac{W}{\sigma_{\text{Stefan}} A_S}, \tag{3.1}$$

where $W$ is the input electric power that was obtained experimentally. Subsequently, we plotted the measured conductivity (in a logarithmic scale) vs. the reciprocal of the absolute specimen temperature curves in Fig. 3.2. While we recognize that this approach of estimating specimen temperature ignores the contributions of heat conduction and convection and the specimen is hardly an

ideal blackbody (and, unfortunately, we do not have the available parameters to do better estimations), a good Arrhenius relation (good linearity in Fig. 3.2) has been obtained for the data obtained from the single crystals before the occurrence of the flash events. This provides us with some confidence on the estimated specimen temperatures and it further allows us to fit the conductivity vs. temperature curves to an empirical Arrhenius equation for ZnO specimens (but not for some other ceramic materials, where the underlying conduction mechanisms are complex and the temperature-dependent conductivity is non-Arrhenius):

$$\sigma(T) = \sigma_0 \cdot e^{-\frac{h}{kT}}, \tag{3.2}$$

where $k$ is the Boltzmann constant and $\sigma_0$ is a pre-exponential constant. The activation enthalpy, $h$, was fitted to be 1.98 ± 0.05 eV (190 ± 5 kJ/mol) and 1.89 ± 0.03 eV (182 ± 3 kJ/mol), respectively, for two single-crystal specimens (by excluding the first two data points, where the measurements were less accurate because of the low currents, and data points after the flash events).

It is important to note that the Arrhenius equation also applies well for the ZnO powder specimens, as demonstrated in Fig. 3.2(b). Thus, Eq. (2.8) is adopted here for ZnO specimens in this study (as well as Todd *et al.*'s study [13] of 3YSZ), while we fully recognize that Eq. (2.8) or a simple Arrhenius relation does not apply to many other ceramic materials.

In Fig. 3.2, we also plotted the measured conductivities vs. estimated specimen temperatures for the activated state (after the occurrence of the flash

events). For ZnO single crystals, the measured conductivities are lower than what would be extrapolated from the Arrhenius equation. This implies the absence of the abnormally-high conductivities due to non-equilibrium defects (such as an abnormal avalanche of Frenkel defects) in ZnO; however, it does not exclude the possible generation of some non-equilibrium defects in the activated state. It should be noted that estimated specimen temperatures could have relatively larger errors for the specimens in the activated state (with great $\Delta T$), which may account for the lower measured conductivities.

Using the fitted temperature-dependent conductivity relation, we calculated the differential heat generation rates (the left side of first equation in Eq. (2.8)) vs. specimen temperature curves for two ZnO single crystals and plotted them in Fig. 3.3(a). In the same figure, we also plotted the differential heat dissipation rate ($\alpha$) vs. specimen temperature curve that was calculated based on the specific specimen geometry and the applied electric field of 300 V/cm, assuming the black body radiation model (using Eq. (3.1)). The intersection of the curves of differential heat generation and dissipation rates represents the solutions of second equation in Eq. (2.8) of Chapter 2, or the flash condition, above which more heat is generated than that can be dissipated, leading to an unstable temperature rise (thermal runaway) or flash.

Specifically for the two ZnO single crystals, the predicted specimen temperatures for a thermal runaway (presumably the onset of the flash) are $T_S$ = 940 °C and $T_S$ = 952 °C, respectively, whereas the estimated specimen temperatures right before the flash from experiments are $T_S$ = 962 °C and $T_S$ =

967 °C (Table 3.1), respectively, which are only 15-22 °C higher, representing good agreements between the model and experiments (Fig. 3.3(a)). Furthermore, the furnace temperatures for the thermal runaway can be predicted from Eq. (2.8) and Eq. (3.1) by using the predicted $T_S$ and the electric power dissipation computed from the fitted $\sigma(T)$; the predicted furnace temperatures for thermal runaway are $T_F$ = 870 °C and $T_F$ = 877 °C, respectively, which are virtually identical to the experimentally-observed onset flash temperatures (Table 3.1, Fig. 3.3(a)).

While such surprisingly-good agreements may be somewhat coincidental, we want to point out three major reasons for the accuracy of the predictions (particularly for $T_F$). First, in the current procedure, the $\sigma(T)$ function was measured in situ while the specimens were in the same furnace/configuration as the flash sintering experiments, and the measured $\sigma(T)$ function was used (extrapolated) to predict the onset flash sintering temperatures subsequently. Thus, any error due to the temperature measurements using the thermocouple in the furnace is largely canceled. Second, the exponential nature of the $\sigma(T)$ function for the current case also made the predictions less sensitive to various approximations and errors.

Third, perhaps the most important underlying reason for the more accurate prediction of the furnace temperature ($T_F$) is that the error for predicted $T_F$ should be (much) less than that for the predicted specimen temperature ($T_S$). This is because the error caused by ignoring the heat conduction and convection,

which are the major error for the current model, can be (partially) canceled in estimating $T_F$. Specifically, we note that the main error for the current calculation comes from the estimation of the heat dissipation terms ($\dot{Q}(T_S,T_F)$ and $\alpha$) by using an overly-simplified blackbody radiation model. As $T_F = T_S - \Delta T$, the errors in the estimation of the heat dissipation terms would change in the estimated $T_S$ and $\Delta T$ in the same direction; in other words, if we over/under estimate the heat dissipation (e.g., by using a simple blackbody radiation model), it will increase/decrease the estimated values of $T_S$ and $\Delta T$ in the same direction, so that the error in the final predicted $T_F$ (= $T_S - \Delta T$) can be (much) less. Consistently, the differences between the predicted and experimentally-estimated $T_S$ values are generally greater (~20 K in general), while predicted $T_F$ values agree with the experiments to higher precisions (± 1 K in three of five cases), as shown in Fig. 3.3 (for both single crystals and powder specimens).

In summary, excellent agreements of the predicted thermal runaway temperatures and the observed onset flash temperatures have been achieved for single-crystal specimens (Fig. 3.3(a)), which has ascertained the proposed model and the underlying hypothesis that the flash starts as thermal runaway.

### 3.3.2. Flash sintering of ZnO powder specimens

We observed that flash sintering started at $T_F$ = 565 °C and $T_F$ = 553 °C, respectively, for two ZnO powder specimens (Fig. 3.1; Table 3.1). Since the most recent study of AC flash sintering of ZnO found the onset flash temperatures to

be at ~670 °C under 80 V/cm and ~620 °C under 160 V/cm, respectively [12], the current observation of onset flash sintering at ~553-565 °C under 300 V/cm DC (instead of AC) field shows a consistent trend of decreasing onset flash sintering temperature with the increasing applied field, regardless of whether a AC or DC field is applied (although the results presented in the next section will show that DC and AC fields can have very different effects on grain growth and microstructural development).

This study demonstrates that the onset flash sintering temperatures of powder specimens ($T_F$ = 550-600 °C) are more than 300 °C lower than the flash temperatures of ZnO single crystals ($T_F$ = 870-877 °C) under the same applied DC electric field of 300 V/cm. This comparison suggests the important role of free surfaces (and/or grain boundaries) in initiating and sustaining the flash sintering. Specifically, it is well established that ZnO often contains surface conduction layers with high concentrations of free electrons (on the order of $10^{12}$ electrons per $cm^2$) [15]; thus, it is possible that the flash in ZnO powder specimens can occur via enhanced electric conduction along the free surfaces of ZnO particles. Based on Arrhenius extrapolations, the apparent conductivities of ZnO powder specimens are one order of magnitude higher than those of single crystals at the same temperatures (Fig. 3.2), which is consistent with the hypothesis that enhanced conduction along free surfaces reduces the onset temperature of flash sintering.

Using the (only) two measured conductivity data for first two ZnO powder specimens before the flash (Fig. 3.2(a)), we fitted the $\sigma(T)$ to Eq. (2.8) and

calculated the differential heat generation and dissipation rates to predict the flash conditions via the same method used for single crystals. The results are shown in Fig. 3(b) as the Specimens #1 and #2, where the predicted and experimentally-estimated specimen temperatures at the thermal runaway/onset flash sintering are $T_S^{(predicted)}$ = 650-662 °C and $T_S^{(exp.)}$ = 675-680 °C, respectively; the corresponding predicted and measured furnace temperatures are $T_F^{(predicted)}$ = 524-545 °C and $T_F^{(exp.)}$ = 553-565 °C, respectively. The agreements (<30 °C in all cases) are satisfactory, given the relative large errors for measuring conductivities at low currents (that are measured using a low-resolution ammeter).

A major error source for predicting the thermal runaway conditions for ZnO powder Specimens #1 and #2 in Fig. 3.3(b) came from the fact that we could measure only two data points before the flash for the powder specimens due to the low resolution of our prior ammeter (Fig. 3.1). Thus, we further conducted an additional experiment using a new high-resolution ammeter that allowed us to measure many data points before the occurrence of the flash. These new data are represented by the open squares in Fig. 3.1 and Fig. 3.2 (referred to as the "new ZnO powder specimen") and the Specimen #3 in Fig. 3.3(b). There are three main observations. First, this new experiment used a higher-purity ZnO (99.99%) powder with smaller starting particle/grain size, which resulted in a somewhat higher onset flash temperature (Fig. 3.1). Second, this new experiment clearly showed the conductivity of ZnO powder specimen follows the Arrhenius relation (Eq. (3.1)), as shown in Fig. 3.2(b). Finally, this new set of data,

where we can measure/fit $\sigma(T)$ to a higher accuracy, lead to the prediction of the thermal runaway temperature that matches the measured onset flash temperature to a higher precision: specifically, the predicted $T_F$ for a thermal runaway is 598 °C vs. the measured $T_F$ for the onset of flash is 599 °C (Fig. 3.3(b)), while the difference in the predicted and experimentally-estimated $T_S$ is ~28 °C. The three reasons for the excellent (and somewhat surprising) agreement in the predicted and observed values of $T_F$ (~1 °C in this specific case) are discussed the last part of §3.3.1.

The above agreements (Fig. 3.3(b)) suggest that the flash sintering in ZnO powder specimens also starts as a result of thermal runaway (similar to the flash of ZnO single crystals) and the model proposed in Chapter 2 is applicable. We further note that a similar thermal runaway model proposed by Todd *et al.* [14] independently (which was submitted ten days later than the original submission of this manuscript) can also quantitatively explain the occurrence of flash in 3YSZ, an ionic conductor and the most extensively-studied flash sintering system, implying the general applicability of the thermal runaway mechanism for the start of flash beyond ZnO (an electronic conductor or a semiconductor self-doped with Zn interstitials and/or oxygen vacancies).

The specimen temperatures at the activated state have also been estimated based on Eq. (3.1). The measured conductivities for the activated state are higher than those extrapolated from a simple Arrhenius relation using the low-temperature data measured before the sintering; however, a simple Arrhenius relation is not expected for this case because the relative densities of

the specimens increased from ~63.5% to ~90% after the flash sintering, accompanying with grain growth, which should affect (increase) conductivity in a nonlinear fashion that is difficult to predict. Alternatively, we estimated the conductivities based on the estimated specimen temperatures and an empirical relation obtained for polycrystalline ZnO specimens in prior studies [16, 17]; these estimated conductivities are listed in Table 3.1, along with the measured conductivities. Specifically, the estimated specimen temperature is 1002 °C for the specimen with $I_{max}$ = 1A, which is more than 400 °C higher than the furnace temperature (~565 °C); the corresponding estimated conductivity at 1002 °C based on Ref. [5] is $8.4 \times 10^{-2}$ S/cm, which is close to the actual measured conductivity of $6.9 \times 10^{-2}$ S/cm. For the specimen with $I_{max}$ = 4A, the estimated specimen temperature is 1407 °C, more than 850 °C higher than the furnace temperature (~553 °C); the corresponding estimated conductivity at 1407 °C is $3.9 \times 10^{-2}$ S/cm, which is again close to the measured conductivity of $3.1 \times 10^{-2}$ S/cm. In both cases, the differences are only ~20% (even if the prior study measured ZnO polycrystal specimens with different/unknown microstructures [16]), suggesting that the conductivities at the activated state during flash sintering are similar to those of normal ZnO polycrystal specimens; thus, the presence of a substantial amount of non-equilibrium defects are not needed to explain the observed conductivities, though some non-equilibrium defects may exist and accelerate sintering rates and affect microstructural development

When the maximum current was set to be 1 A, a relative density of 90.8 %

was achieved after the flash sintering (30 seconds in the activated state, where $J_{max} \approx 3.9$ A/cm$^2$ and $E \approx 52$ V/cm at the final steady state; noting that $E$ was set to 300 V/cm before the power source switched to the current-limited mode for all cases). When the maximum current was set to be 4 A ($J_{max} \approx 15.4$ A/cm$^2$ and $E \approx$ 44 V/cm at the final steady state), a slightly lower sintered density (87.3%) was achieved. The reduction of densification at the high current density is presumably caused by excess grain growth. Given the high specimen temperatures reached at 4A, the volatility of ZnO may also be a relevant factor. The measured grain size is >10 times greater and highly non-uniform in the latter case, which will be discussed in detail in the next section. The results of sintered densities and measured grain sizes are summarized in Table 3.1.

A comparison of grain size effects in flash sintering was conducted by comparison of different initial grain size and same relative density of green specimens. Measure conductivity (σ) vs. reciprocal specimen temperature (1/T) for the powder specimen with initial grain size of 120 nm and 700 nm, and single crystal specimen was shown in the Fig. 3.4 (a). It represents a good linear relationship between log(σ) and 1/T, indicating Eq. (3.2) is applicable for the conductivity of the ZnO specimen before the flash. The activation energy of powder specimen with initial grain size of 120 nm and 700 nm, and single crystal specimen is 1.32 eV, 1.40 eV and 1.89 eV. It supported our hypothesis that ZnO has a surface conduction layer with high concentrations of free electrons mentioned above because of in the same volume, larger particle/grain size, less surface area, and lower electric conductivity. Fig. 3.4 (b) shows measured

electric power dissipation vs. furnace temperature curves for the flash sintering of powder specimen with initial grain size of 120 nm and 700 nm (assuming no changes in the specimen volume in calculating electric power dissipation for simplicity) and ZnO single crystals, indicating the onset flash sintering temperatures are varied in these three specimens. Figure 3.5 shows computed differential heat generation and dissipation rates vs. specimen temperature curves for the powder specimen with initial grain size of 120 nm and 700 nm, and single crystal specimen. The thermal runaway (flash) condition (Eq. (2.8)) can be determined graphically by finding the intersection of the heat generation and dissipation rates curves, above which more heat is generated than that can be dissipated, leading to thermal runaway. The predicted onset flash sintering temperature from thermal runaway condition is 598 °C, 786 °C and 870 °C for powder specimen with initial grain size of 120 nm and 700 nm, and single crystal specimen, respectively. The experimental records of onset flash sintering temperature is 599 °C, 789 °C and 870 °C for powder specimen with initial grain size of 120 nm and 700 nm, and single crystal specimen, respectively. There is less than 3 °C difference between prediction and experimental record of onset flash sintering temperature in all these three different specimens, indicating that our model could be applied in specimens with different initial grain size.

### 3.3.3. Asymmetrical microstructural development: potential-induced abnormal grain growth

A particular intriguing and interesting observation of this study is

represented by the anode-side abnormal grain growth and/or coarsening during the flash sintering of pure ZnO powder specimens (noting that here the term “abnormal grain growth” is used to represent a case of abruptly faster grain growth in the anode side with an overall bimodal grain size distribution in the specimen); the measured grain sizes are substantially greater in the anode (+) side than those at the cathode (-) sides. When the maximum current was set to be 1 A ($J_{max} \approx 3.9$ A/cm$^2$), the average grain sizes of cathode (-) and anode (+) sides, respectively, were measured to be 0.4 ± <0.1 μm and 0.9 ± 0.1 μm, respectively; this grain size disparity is clearly evident in Figs. 3.6(a) vs. 4(b) and Fig. 3.7. Since the starting particle size was slightly smaller than 0.5 μm, essentially no grain growth occurred at the cathode side, while the grain size doubled at the anode side. When the maximum current was set to be 4 A ($J_{max} \approx$ 15.4 A/cm$^2$), the disparity increased further. The average grain sizes of the cathode and anode sides, respectively, were measured to be 3.5 ± 1.8 μm and 32.3 ± 5.6 μm, respectively (Fig. 3.8). In this case, there was substantial grain growth at the cathode size (by approximately 8×) and excess grain growth at the anode side (by approximately 80×); in the final state, the grains are about 10× larger at the anode side. In the most recent study of flash sintering of ZnO, AC fields (up to 160 V/cm) were used so that the asymmetric microstructural development and abnormal grain growth were not observed [12].

It is interesting to note that the grain growth was much greater with a current limit of 4A than that with 1A, with the identical maximum electric field

(before the switch to current control), which suggests that the maximum field experienced is not the determining factor in inducing grain growth.

The observation of enhanced grain growth at the anode side is somewhat in contrast to a prior report, where the grain growth was found to be enhanced at the cathode side in 8YSZ [18]. In that study, the grain growth occurred at the cathode side, which should not occur at that temperature without an electric current normally; Chen and co-workers attributed enhanced grain boundary mobility to the interaction of supersaturated oxygen vacancies and grain boundaries and a possible grain boundary reduction reaction that lowers the cation migration barriers [18]. Adapting and extending Chen and coworkers' theory from 8YSZ to ZnO, we propose that in the current case of ZnO, electrons accumulate at the anode size (due to the positive electric potential) and interact with surfaces and/or grain boundaries to enhance the interfacial transport rates via an oxidation reaction that increases the local cation vacancy concentration, which subsequently accelerates the coarsening of particles and/or grain growth during the flash sintering. Consistently, Tuller suggested that cations diffuse along ZnO grain boundaries via cation vacancies formed via an oxidation reaction at grain boundaries [19]. According to/adapting the grain boundary oxidation reaction originally proposed by Tuller [19], the following defect chemical reactions may occur at ZnO grain boundaries in the anode side, induced by the presence of excess electrons:

$$\begin{matrix} e' + \frac{1}{2}\mathrm{O}_2(\mathrm{gas}) \rightarrow \mathrm{O}_\mathrm{O}^\times + \mathrm{V}_\mathrm{Zn}{}' \\ e' + \mathrm{V}_\mathrm{Zn}{}' \rightarrow \mathrm{V}_\mathrm{Zn}{}'' \end{matrix} . \quad (3.3)$$

Tuller also pointed out that the formation of Zn vacancies at grain boundaries appears to be counterintuitive since ZnO is normally believed to be a metal excess (or oxygen deficient) material [15, 19]. However, this disparity between the bulk and grain boundary defect structures can be well rationalized since the thermodynamic states [20-22] and (therefore) the defect structures [23, 24] of grain boundaries can often differ markedly from those of the corresponding bulk materials. If the above hypothesis of forming cation vacancies at ZnO grain boundaries (and free surfaces) induced by the positive electric potential and the corresponding accumulation of electrons is true, the grain growth and/or coarsening can be enhanced at the anode side, corroborating with the experimental observations made in the current study (Figs. 3.6-3.8).

Moreover, Fig. 3.7 shows an abrupt (discontinuous) transition between the large and small grains and this transitional line is located at ~56 μm away from the anode edge of the pure ZnO sample that was flash-sintered with $I_{max}$ = 1 A (noting that that the abnormal grain growth only occurred within a short distance to the anode in this specimen). A similar discontinuous transition was observed in 8YSZ by Kim *et al.* [18]. A discontinuous increase in grain boundary mobility and the associated abnormal grain growth indicate the possible occurrence of a grain boundary structural (complexion) transition [9], which, in the current case, is presumably a subtle structural transition associated with the formation of excess

cation vacancies at grain boundaries (Eq. (3.3)) (that is difficult to be verified directly via experiments). Similar abnormal grain growth behaviors have been previously attributed to the formation of intergranular films [25] and complexion transitions [26-28] in two separate studies.

This abrupt transition (Fig. 3.7) also suggests that the disparity in grain growth is unlikely to be a simple result of temperature non-uniformity (in addition, the geometrical and heat transfer conditions were kept symmetric with respect to the anode and the cathode in our experiments); otherwise, a gradual change in the grain sizes would generally be expected (unless there is a temperature-induced discontinuous interfacial structural transition that occurs coincidentally).

### 3.3.4. Asymmetrical microstructural development: growth of single-crystalline rods against the direction of the electric field

At the high current density of $J_{max} \approx 15.4$ A/cm$^2$ ($I_{max} = 4$ A), the growth of aligned single-crystalline rods and fibers was observed in the pure ZnO powder specimen, which presumably occurred at the cracks. Fig. 3.9(a) shows the growth of an array of such rods at ~1.4 mm away from the anode, and Fig. 3.9(b) shows some fibers grown at another location in an expanded view. These fibers and rods ranged from ~5 to >30 μm in their lengths. Many rods and fibers are hexagonal, and Fig. 3.9(c) shows enlarged views of some hexagonal rods. This observation suggests a directional growth of ZnO rods and fibers along the *c* axis of the ZnO crystal structure; this directional growth along the <0001> direction is likely related to the polarity of the ZnO crystal structure, in which positively-

charged Zn-(0001) planes and negatively-charged O-(000$\bar{1}$) planes are packed alternatingly [29].

It should be pointed out that the growth of ZnO rods may be related to local melting at cracks (therefore liquid-phase growth locally). Nonetheless, it is interesting to note that the alignment of ZnO rods does show an electric field effect. We should note that this experiment was performed at a current density that is higher than those commonly used in normal flash sintering. Nonetheless, the growth of aligned ZnO rods represents yet another interesting observation.

It is also interesting to note that all ZnO fibers and rods grew towards to the anode direction (Fig. 3.9). In comparison, Chen and co-workers found that pores migrated against the direction of the electric field via an ionomigration mechanism, along with enhanced grain growth in the cathode side, in a series of systematic studies of 8YSZ [18, 30-32]. In the current case, the ZnO rods and fibers grew against the direction of the electric field (Fig. 3.9), while the coarsening and grain growth were enhanced at the anode side (Figs. 3.6-3.8).

### 3.3.5. The effects of $Bi_2O_3$ doping

We further conducted experiments to test the effects of $Bi_2O_3$ doping on the flash sintering and microstructural development, which had not been conducted before. We have revealed several interesting phenomena, as discussed below.

First, addition of minor (0.5 mol. %) amount of $Bi_2O_3$ dopants defers the onset of the flash sintering of ZnO powder specimens from ($T_F$ =) 553-565 °C to

($T_F$ =) 620-621 °C, despite that $Bi_2O_3$ is typically considered as a sintering aid that should lower the sintering temperature of ZnO [51]. Moreover, this observation appears to be in contrast to several prior studies, where doping enabled or promoted the occurrence of flash sintering in $Al_2O_3$ (with MgO doping) [33] and $SnO_2$ (with $MnO_2$ doping) [34]. However, the observation of deferring onset flash sintering of ZnO by $Bi_2O_3$ doping can be readily understood via the doping effects on forming potential barriers at grain boundaries. $Bi_2O_3$-doped ZnO is a prototype system for varistors, where double Schottky barriers (as a result of space charges) form at grain boundaries, leading to nonlinear I-V behaviors [35]. The formation of such potential barriers at grain boundaries reduced the conductivities of the powder specimens, as evident by the measured conductivities shown in Fig. 3.2(a), which subsequently deferred the onset of the flash sintering (Fig. 3.1, Table 3.1).

Second, although $Bi_2O_3$ can delay the onset of flash sintering by decreasing the conductivities (below the solidus line of ZnO-$Bi_2O_3$ binary system), the ZnO-$Bi_2O_3$ binary system has a eutectic reaction at 740 °C, above which a $Bi_2O_3$-based liquid phase forms; this can then significantly enhance sintering via liquid-phase (or solid-stare activated [36]) sintering mechanisms above (or near) the solidus line. Moreover, a series of prior studies demonstrated that nanometer-thick, premelting-like (quasi-liquid) films (that are 2-D interfacial “phases” and also called “complexions” [17, 20, 21, 26, 37-42]) can develop at both grain boundaries [43,44] and free surfaces [45-48] below the bulk eutectic temperature of 740 °C. All these facts suggest a modified flash sintering

mechanism in $Bi_2O_3$-doped ZnO, where $\sigma(T)$ can no longer be represented by a simple Arrhenius relation (as being assumed for pure ZnO single crystals and powder specimens). Experimentally, the onset flash sintering occurred at the furnace temperatures of $T_F$ = 620-621 °C in the current study; the corresponding specimen temperatures are estimated to be 667-734 °C (Table I), which are slightly below the bulk eutectic temperature of 740 °C. This suggests that the occurrence of flash sintering is resulted from the formation of either a small amount of $Bi_2O_3$-based bulk liquid phase or interfacial liquid-like complexions [36, 47, 48] which changes (increases) the conductivity of the specimens substantially. This hypothesis is consistent with and supported by the measured conductivities shown in Fig. 3.2.

Third, at the activated (flash sintering) state, the estimated specimen temperatures are 877 °C (for $J_{max} \approx 3.9$ A/cm$^2$) and 1254 °C (for $J_{max} \approx 15.2$ A/cm$^2$), respectively (Table I), well exceeding the eutectic temperature of 740 °C; thus, this is a case of liquid-phase sintering, which may be modified (enhanced) by applied electric currents. We should further note that the addition of $Bi_2O_3$ increased the conductivity above the solidus line (although it decreased the conductivity below the solidus line), as shown in Fig. 3.2(a), which subsequently reduced the specimen temperatures in the activated flash sintering state (by ~100-150 °C under identical $I_{max}$; see the estimated specimen temperatures in Table 3.1); yet substantial densification and grain growth were resulted from the liquid-phase sintering effects in the activated state (Table 3.1, Fig. 3.10).

Finally, $Bi_2O_3$ doping also made the grain growth and microstructural development uniform at both the cathode and anode sides. Fig. 3.10 (a) and (b) show the microstructures of cathode and anode sides of the 0.5 mol. % $Bi_2O_3$-doped ZnO specimen that was flash-sintered with $J_{max} \approx 3.9$ A/cm$^2$ (under the conditions identical to those used for the pure ZnO powder specimens); the measured grain sizes of cathode (-) and anode (+) sides, respectively, are 2.0 ± 0.2 μm and 1.7 ± 0.2 μm, respectively, which are essentially identical within the experimental errors. Furthermore, Fig. 3.10 shows a typical liquid-phase sintering microstructure with pores of ~0.5 μm in diameters being trapped at grain boundaries. A sintered density of 91.5 % has been achieved at this sintering condition ($J_{max} \approx 3.9$ A/cm$^2$), which is slightly higher than that of pure ZnO powder specimen flash-sintered at the identical conditions (Table 3.1). At a high current density of $J_{max} \approx 15.2$ A/cm$^2$, the sintered density reduced to 88.2% of the theoretically density, which could again be attributed to excess particle coarsening and grain growth during the initial stage of flash sintering; the measured final grain size are ~13 μm, being identical at the cathode and anode sides within the experimental errors (Table 3.1). The homogenization of microstructures and inhibition of the anode-side abnormal grain growth (that was observed for pure ZnO) can be attributed to a liquid-phase sintering effect.

### 3.3.6. The effects of $Al_2O_3$ doping

$Al_2O_3$ doped ZnO (AZO) specimen was applied by flash sintering in the same condition as pure ZnO under DC electric filed of 300 V/cm and current limit

at 1 A or 4 A. Figure 3.11 (a) shows measure conductivity (σ) vs. reciprocal specimen temperature (1/T) of pure ZnO (powder 2) and 2 wt.% $Al_2O_3$ doped ZnO. Fig. 3.11 (b) shows measured electric power dissipation vs. furnace temperature curves for the flash sintering of pure ZnO and AZO (assuming no changes in the specimen volume in calculating electric power dissipation for simplicity). Power density of flash sintering of AZO with current limit of 1 A and 4 A are shown as in red round symbol and triangle symbol, respectively. The onset flash sintering temperature in AZO with current limit of 1 A and 4 A has slightly difference because of specimen-to-specimen variation, at 524 °C and 530 °C, respectively. The final density of these two specimens are ~69% and ~97% of theoretical density for the specimen with current limit of 1 A and 4 A, respectively.

Figure 3.12 shows computed differential heat generation and dissipation rates vs. specimen temperature curves for pure ZnO and AZO. The predicted onset flash sintering temperature from thermal runaway condition is 521 °C, which is only 3 degrees lower than experimental record. It demonstrates that the model could be applied in $Al_2O_3$ doped ZnO.

One interesting phenomenon we observed on the specimen of AZO after flash sintering at cross section is high aluminum concentrated “white” particles accumulated in cathode side (Fig. 3.13 (a-e)). From the energy-dispersive X-ray spectroscopy (EDS) analysis, the composition of “grey” particles are ~ 49 mol. % of oxygen, ~ 3 mol.% of aluminum, and ~ 48 mol. % of zinc; the composition of “white” particles are ~ 54 mol. % of oxygen, ~ 24 mol.% of aluminum, and ~ 22 mol. % of zinc. The “white” particles are high Al concentration and it could be Al-

Zn-O compound according to phase diagram. The “white” particles are mostly accumulated in cathode area (Fig. 3.13 (c-e)). The possible reason could be movement of $Al_{Zn}^{\bullet}$ particle migrating towards cathode side because of positive charge under electric field. This could be an evidence of electric effects on microstructure evolution during flash sintering.

### 3.4 Conclusions

DC flash sintering experiments were conducted both pure ZnO, 0.5 mol. % $Bi_2O_3$-doped ZnO, and 2 wt.% $Al_2O_3$ doped ZnO, along with benchmark flash experiments of ZnO single crystals, at a relatively high fixed initial applied electric field of 300 V/cm. The main findings and conclusions are summarized as follows:

- The excellent agreements between the predicted thermal runaway temperatures and observed onset flash temperatures authenticate the key underlying hypothesis, *i.e.*, the flash starts as a thermal runaway for at least ZnO single crystals and powder specimens (as well as 3YSZ as demonstrated independently by Todd *et al.* in a publication [13] that was submitted shortly after the initial submission of this manuscript, which we noted during the revision of this manuscript) without the need of introducing an avalanche of non-equilibrium defects, although some non-equilibrium defects may form after the onset of the flash to accelerate the sintering and affect microstructural development; the $Bi_2O_3$ doping leads to the formation of a bulk eutectic liquid or liquid-like interfacial complexion that causes a discontinuous increase in conductivity to initiate the flash

sintering in a similar mechanism.

- Compared with single crystals, the flash of ZnO powder specimens occurs at a substantially lower temperature, indicating the important roles of surfaces and grain boundaries; in particular, the reduction of onset flash temperature is explained from the enhanced conduction along the surfaces of ZnO particles, and this mechanism is also supported by the conductivity measurements and the model-experimental comparison.
- One intriguing and interesting observation is represented by the enhanced coarsening and/or grain growth at the anode side during the flash sintering, in contrast to the enhanced grain growth at the cathode side that was previously reported for 8YSZ [18]; the observation of a discontinuous transition between small and large grains suggests the occurrence of abnormal grain growth/coarsening resulted from an interfacial (defect) structural transition [20]; this cathode-side abnormal grain growth can be explained from the electric-potential-induced accumulation of electrons and an associated oxidation reaction to form excess cation vacancies at ZnO grain boundaries that promote interfacial diffusion, following Tuller's theory of ZnO grain boundary defect chemistry [19], as well as extending and combining Chen and colleagues' original concept of potential-induced abnormal grain growth [18] and the idea of grain boundary complexion transitions [20].
- Aligned growth of single-crystalline ZnO rods and fibers towards the anode direction was observed at a high current density for the pure ZnO

powder specimen.

- $Bi_2O_3$ doping defers the onset of flash sintering, which is in contrast with prior studies where doping promoted flash sintering [33, 34]; however, this observation can be readily explained by the formation double Schottky barriers at grain boundaries of $Bi_2O_3$-doped ZnO, a prototype varistor material.
- $Bi_2O_3$ doping also homogenizes the microstructure (by eliminating the anode-side abnormal grain growth) via a liquid-phase sintering effect.
- $Al_2O_3$ doping promotes onset flash sintering because of increasing electric conductivity. An interesting phenomenon of $Al_{Zn}^{\bullet}$ particle migration towards cathode side under electric field was observed.

In summary, this study elucidates the flash mechanism, establishes a quantitative model and approach to predict the onset flash (thermal runaway) temperatures, and reports diversifying phenomena of sintering and grain growth under the influences of electric fields and currents.

Chapter 3, in part, is a reprint of the material “Thermal Runaway, Flash Sintering and Asymmetrical Microstructural Development of ZnO and ZnO-$Bi_2O_3$ under Direct Currents” as it appears in the Acta Materialia, Yuanyao Zhang, Jae-Il Jung, and Jian Luo, Acta Materialia, 2015, 94, 87-100. The dissertation author was the primary investigator and author of this paper. All experiments and data analysis were performed by the author except for some SEM images.

Table 3.1 Summary of key experimental results of flash sintering of ZnO in air. The maximum current densities ($J_{max}$) were calculated based on the final specimen dimensions and measured electric currents. The initial electric field ($E$) was always set to be 300 V/cm; the power source switched to the current-limited mode for most specimens and the final electric fields ($E$) were calculated based the measured voltages and the final specimen thickness. The estimated conductivities for ZnO powder specimens were calculated based on the estimated specimen temperatures and an empirical relation of $\sigma(T) = 54e^{-0.71eV/kT}$ S/cm, reported in a prior study [16] for ZnO polycrystals.

| Sample | $I_{max}$ (A) | Sintered Relative Density | Measured Mean Grain Size ± One Standard Deviation (μm) | | Thermal Runaway vs. Onset Flash $T$ | | After the Flash (in the Activated State) | | | | |
|---|---|---|---|---|---|---|---|---|---|---|---|
| | | | | | | | Estimated $T_S$ (°C) | $E$ (V/cm) | $J_{max}$ (A/cm$^2$) | Conductivity (S/cm) | |
| | | | Cathode (-) Side | Anode (+) Side | $T_F$ (°C) | Estimated $T_S$ (°C) | | | | Measured | Estimated |
| ZnO Single Crystals | 1 | - | - | - | 870 | 962 | 1270 | 300 | 4.0 | $1.4 \times 10^{-2}$ | - |
| | 1.45 | - | - | - | 877 | 967 | 1417 | 274 | 5.8 | $1.8 \times 10^{-2}$ | - |
| Pure ZnO (Powder) | 1 | 90.8% | 0.4 ± <0.1 | 0.9 ± 0.1 | 565 | 675 | 1002 | 52 | 3.9 | $6.9 \times 10^{-2}$ | $8.4 \times 10^{-2}$ |
| | 4 | 87.3% | 3.5 ± 1.8 | 32.3 ± 5.6 | 553 | 662 | 1407 | 44 | 15.4 | $3.3 \times 10^{-1}$ | $3.9 \times 10^{-1}$ |
| ZnO + 0.5 mol. % $Bi_2O_3$ (Powder) | 1 | 91.5% | 2.0 ± 0.2 | 1.7 ± 0.2 | 621 | 734 | 877 | 31 | 3.9 | $1.2 \times 10^{-2}$ | - |
| | 4 | 88.2% | 13.1 ± 1.6 | 12.6 ± 1.1 | 620 | 667 | 1254 | 28 | 15.2 | $5.1 \times 10^{-2}$ | - |

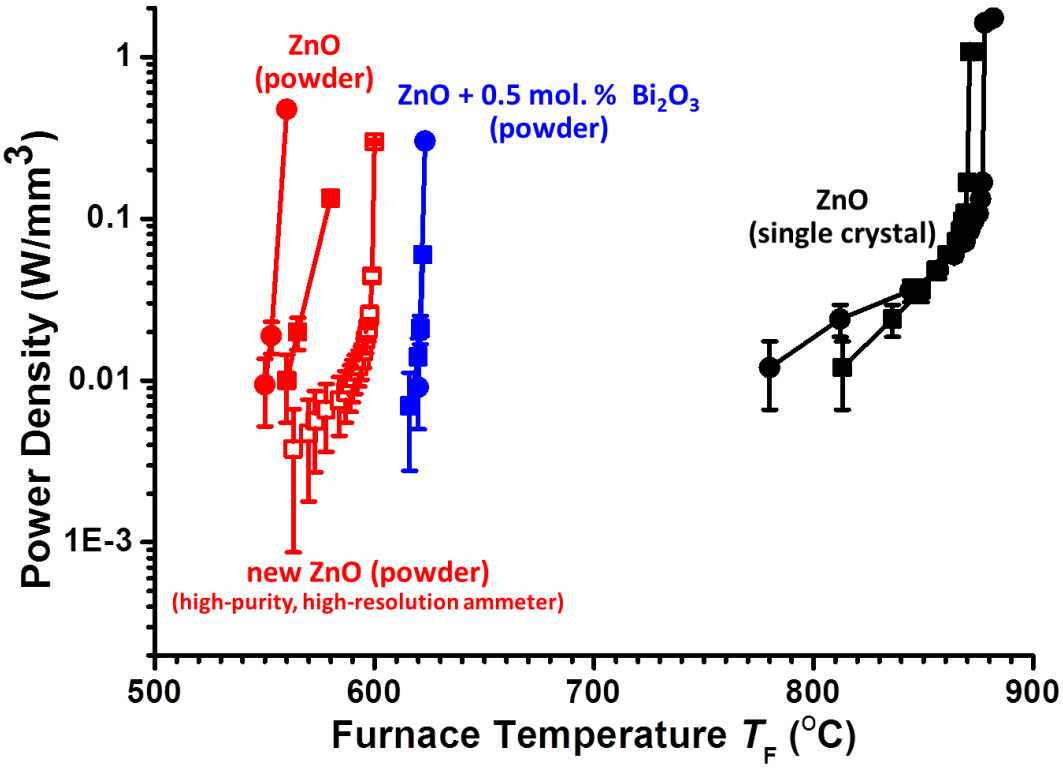


Figure 3.1 Measured electric power dissipation vs. furnace temperature curves for the flash sintering of pure and 0.5 mol. % $Bi_2O_3$-doped ZnO powder specimens (assuming no changes in the specimen volume in calculating electric power dissipation for simplicity) and ZnO single crystals. For each of the three cases, experiments were conducted for two specimens, where we set $I_{max} \leq 1$A (with the corresponding data points being represented by squares) and $I_{max} \leq 4$A (represented by circles), respectively (noting that the current did not reach 4A for the single crystal specimen). The open red squares represent an additional new experiment where we used a high-purity ZnO powder and a high-resolution ammeter so that we can measure more data points before the occurrence of the flash event (to allow a more critical test of the proposed thermal runaway model).

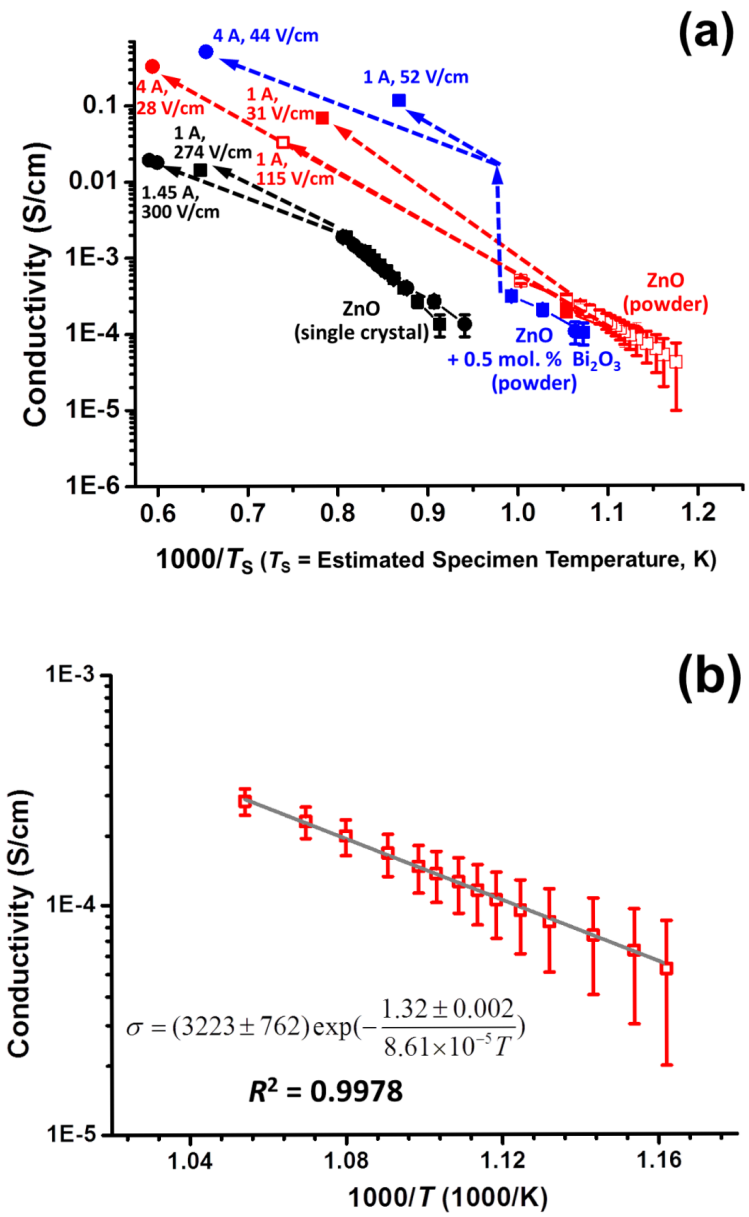


Figure 3.2 (a) Measured conductivity vs. the reciprocal of the estimated specimen temperature curves. (b) Measured conductivity vs. the reciprocal temperature for the new ZnO powder specimen, indicating Eq. (7) is applicable for the conductivity of the ZnO specimen before the flash.

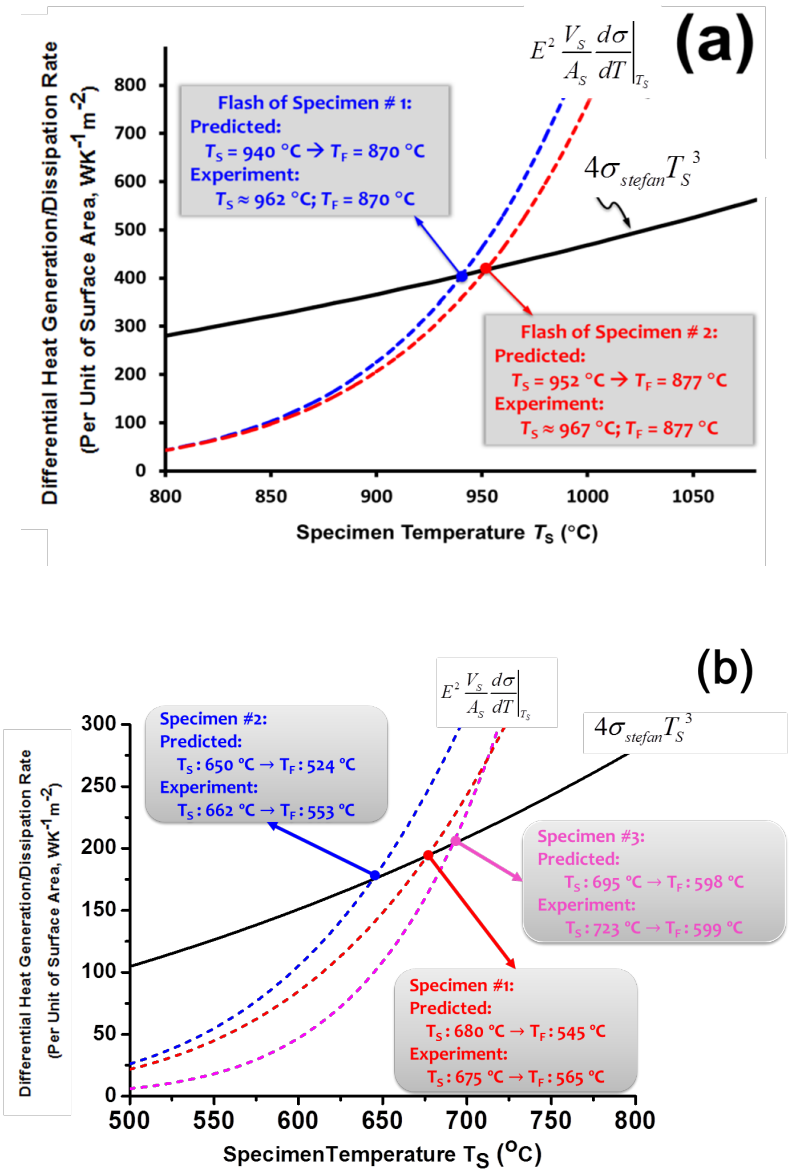


Figure 3.3 Computed differential heat generation and dissipation rates vs. specimen temperature curves for the pure ZnO (a) single crystals and (b) powder specimens, respectively. Each panel includes data from two or three specimens. The thermal runaway (flash) condition (Eq. (2.8)) can be determined graphically by finding the intersection of the heat generation and dissipation rates curves, above which more heat is generated than that can be dissipated, leading to thermal runaway. Noting that the second condition for determining the start point of thermal runaway (Eq. (2.8)) is automatically satisfied in the current model and numerical approach of solving $T_S$ and $T_F$; see text for explanation.

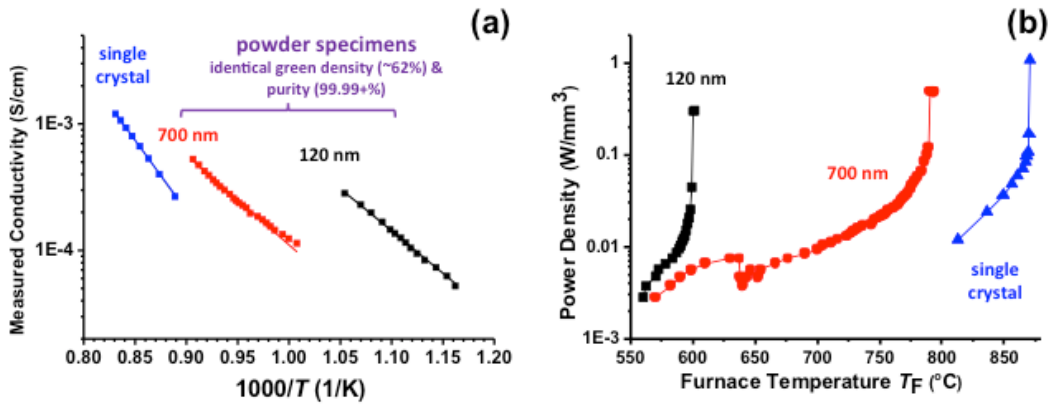


Figure 3.4 (a) Measure conductivity (σ) vs. reciprocal specimen temperature (1/T) for the powder specimen with initial grain size of 120 nm and 700 nm, and single crystal specimen. It represents a good linear relationship between log(σ) and 1/T. (b) Measured electric power dissipation vs. furnace temperature curves for the flash sintering of powder specimen with initial grain size of 120 nm, 700 nm (assuming no changes in the specimen volume in calculating electric power dissipation for simplicity) and ZnO single crystals, indicating the onset flash sintering temperatures are varied in these three specimens.

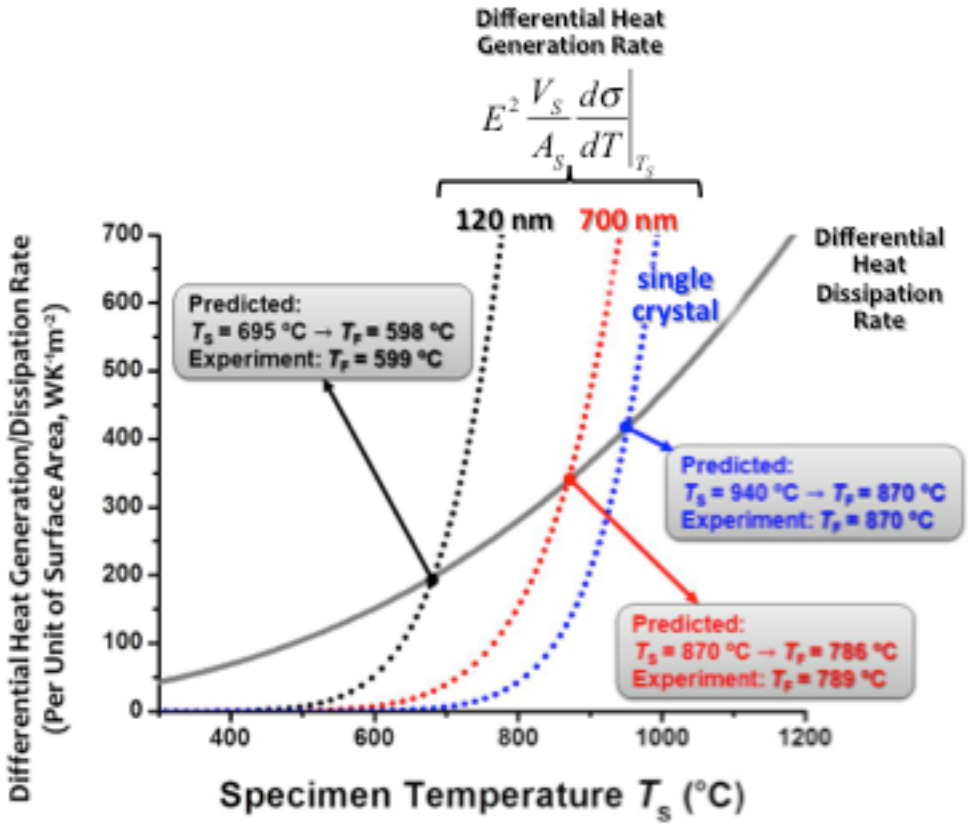


Figure 3.5 Computed differential heat generation and dissipation rates vs. specimen temperature curves, for the powder specimen with initial grain size of 120 nm and 700 nm, and single crystal specimen. The thermal runaway (flash) condition (Eq. (2.8)) can be determined graphically by finding the intersection of the heat generation and dissipation rates curves, above which more heat is generated than that can be dissipated, leading to thermal runaway.

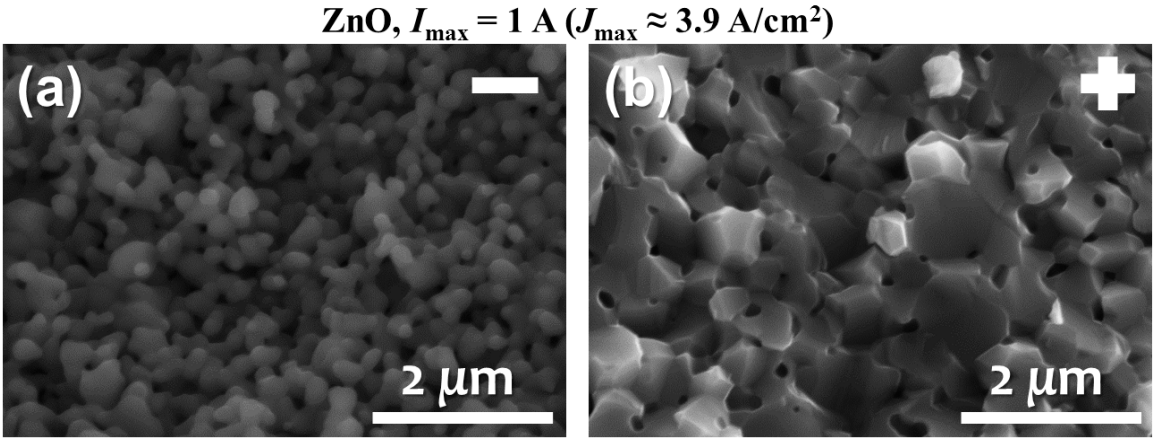


Figure 3.6 SEM micrographs of (a) the cathode (-) side and (b) the anode (+) side of a fractured surface of a pure ZnO specimen flash-sintered with a low current density.

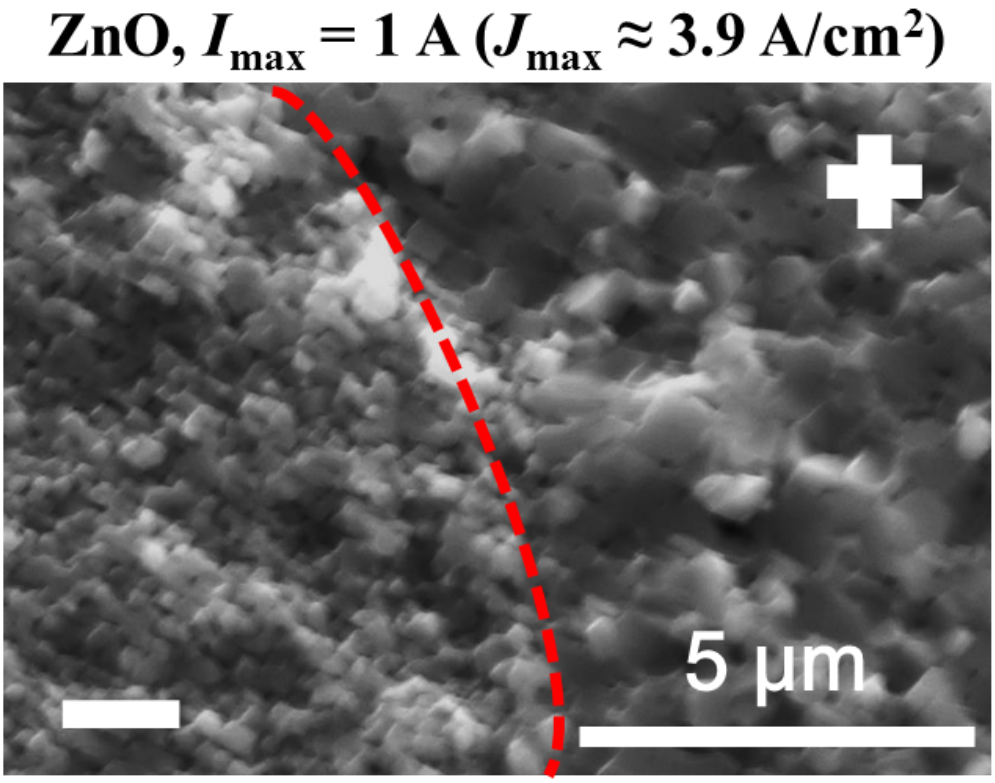


Figure 3.7 SEM micrograph of a fractured surface of a pure ZnO specimen flash-sintered with a low current density, showing an abrupt transition from small to large grains. This transition occurred at a region that was located at about 56 μm away from the anode edge.

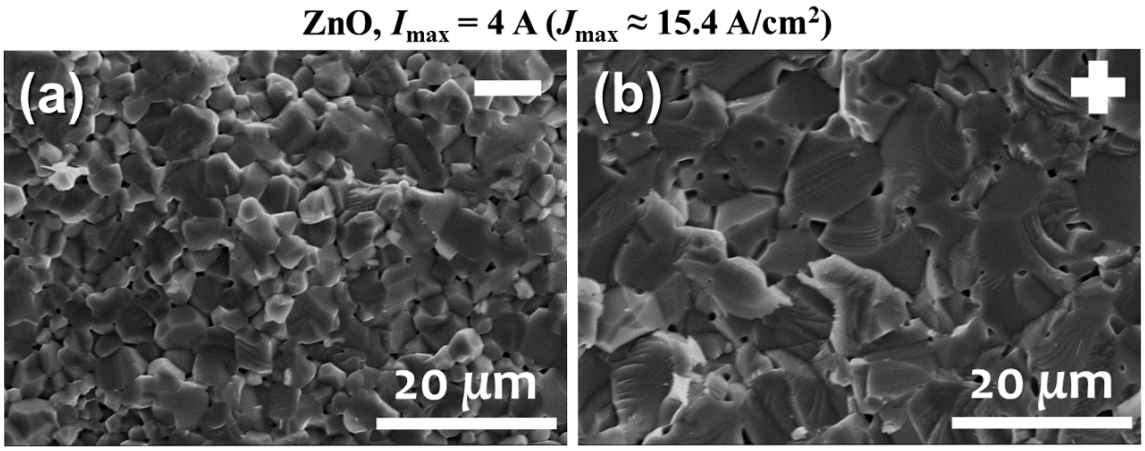


Figure 3.8 SEM micrographs of (a) the cathode (-) side and (b) the anode (+) side of a fractured surface of a pure ZnO specimen flash-sintered with a high current density.

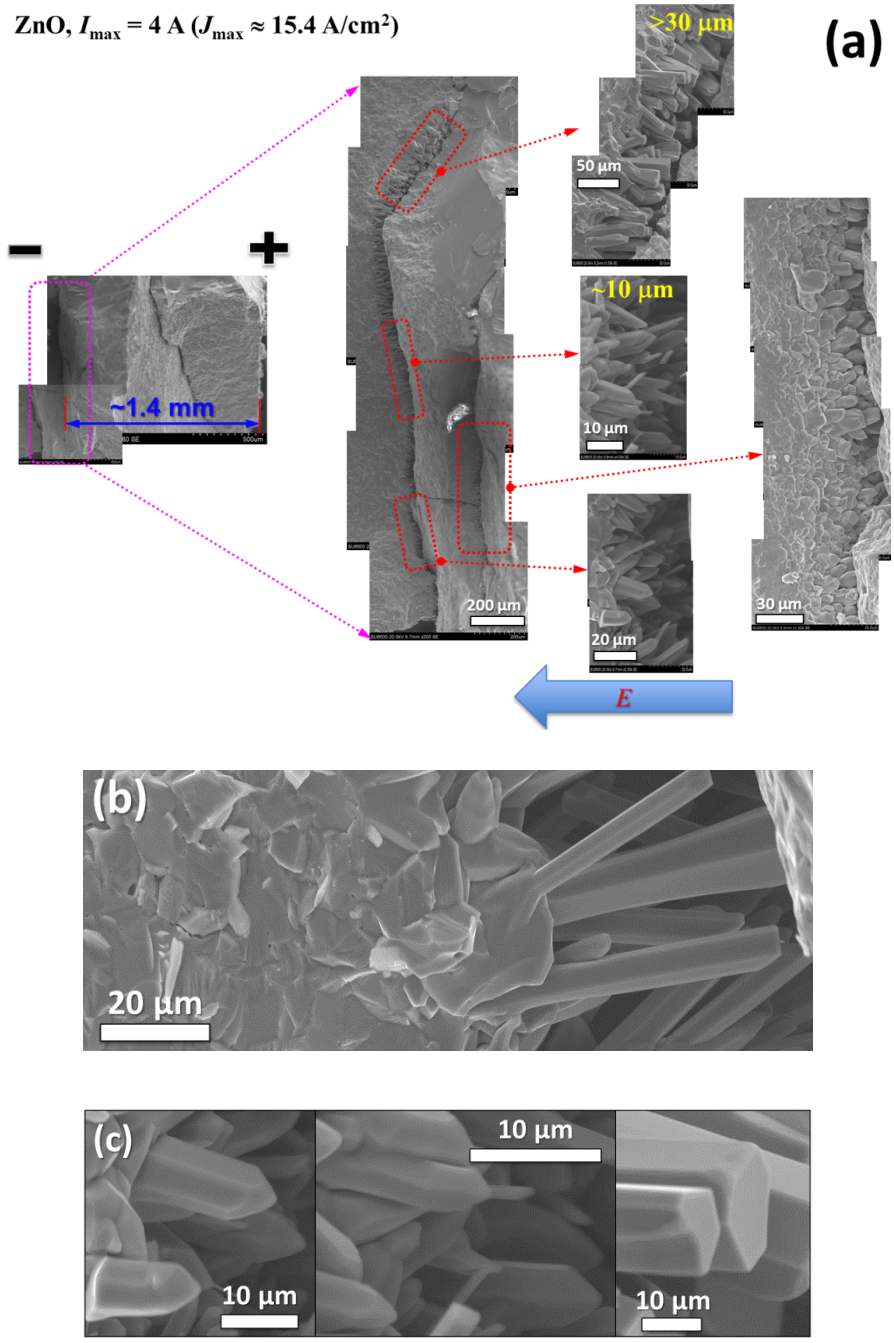


Figure 3.9 (a) SEM micrographs of crystal rods grown at about 1.4 mm away from the anode edge of a pure ZnO specimen flash-sintered with a high current density. (b) An enlarged image of the ZnO rods grown at a different region. (c) Enlarged views of some hexagonal rods. The growth of ZnO rods may be related to local melting at cracks (at a current density that is higher than those commonly used for normal flash sintering).

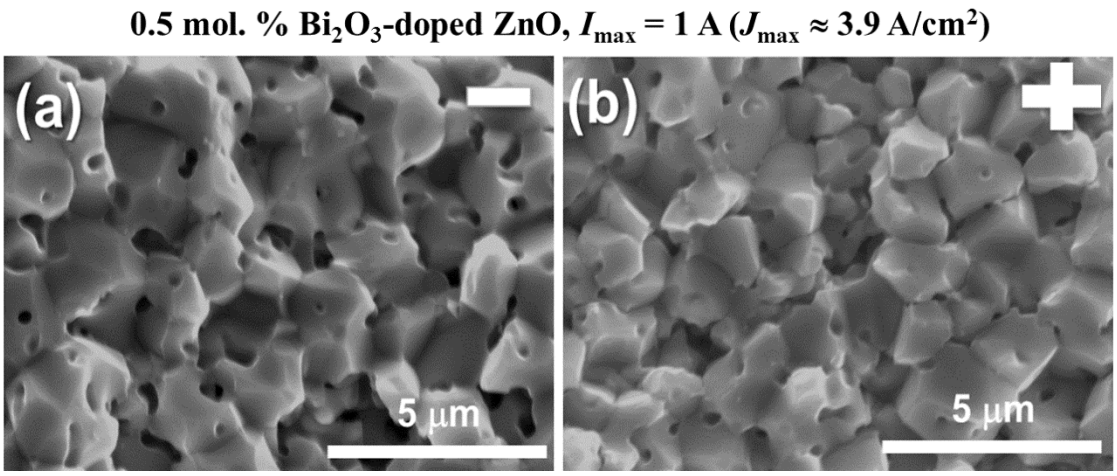


Figure 3.10 SEM micrographs of (a) the cathode (-) side and (b) the anode (+) side of a fractured surfaces of a 0.5 mol. % $Bi_2O_3$-doped ZnO specimen flash-sintered with a low current density.

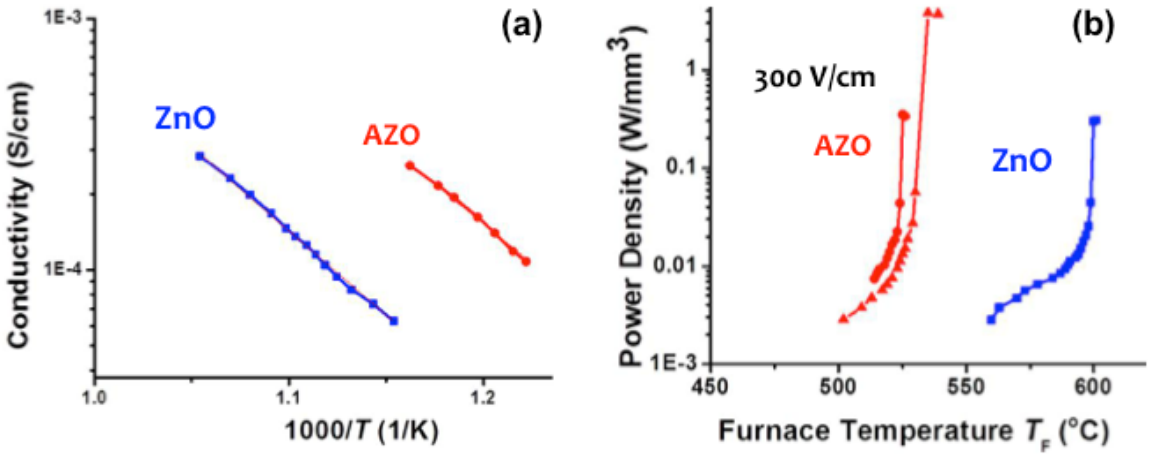


Figure 3.11 (a) Measure conductivity (σ) vs. reciprocal specimen temperature (1/T) of pure ZnO and 2 wt.% $Al_2O_3$ doped ZnO. (b) Measured electric power dissipation vs. furnace temperature curves, for the flash sintering of pure ZnO and 2 wt.% $Al_2O_3$ doped ZnO (assuming no changes in the specimen volume in calculating electric power dissipation for simplicity). Power density of flash sintering of AZO with current limit of 1 A and 4 A are shown as in red round symbol and triangle symbol, respectively.

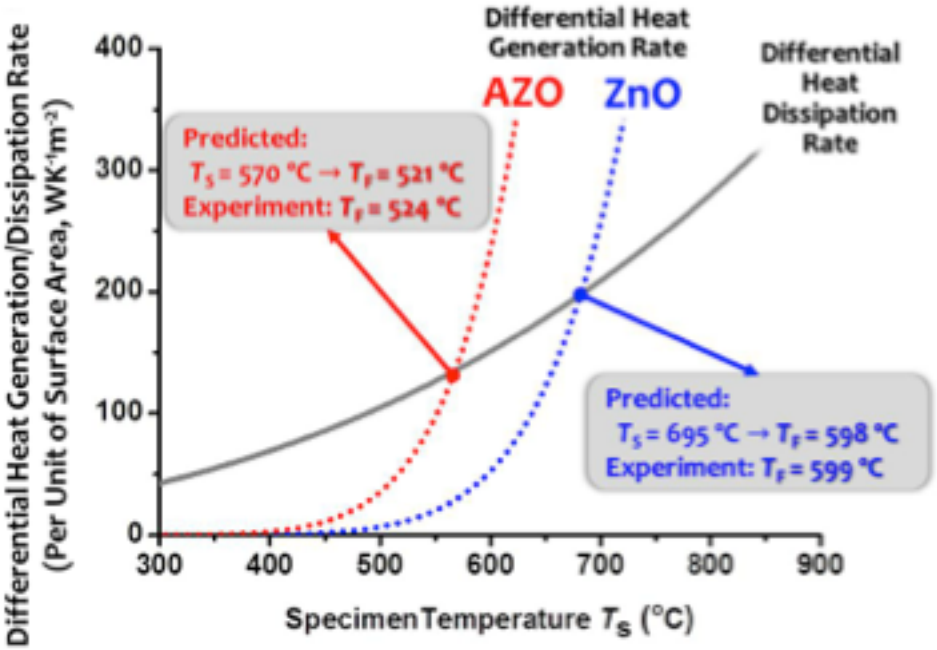


Figure 3.12 Computed differential heat generation and dissipation rates vs. specimen temperature curves for pure ZnO and AZO.

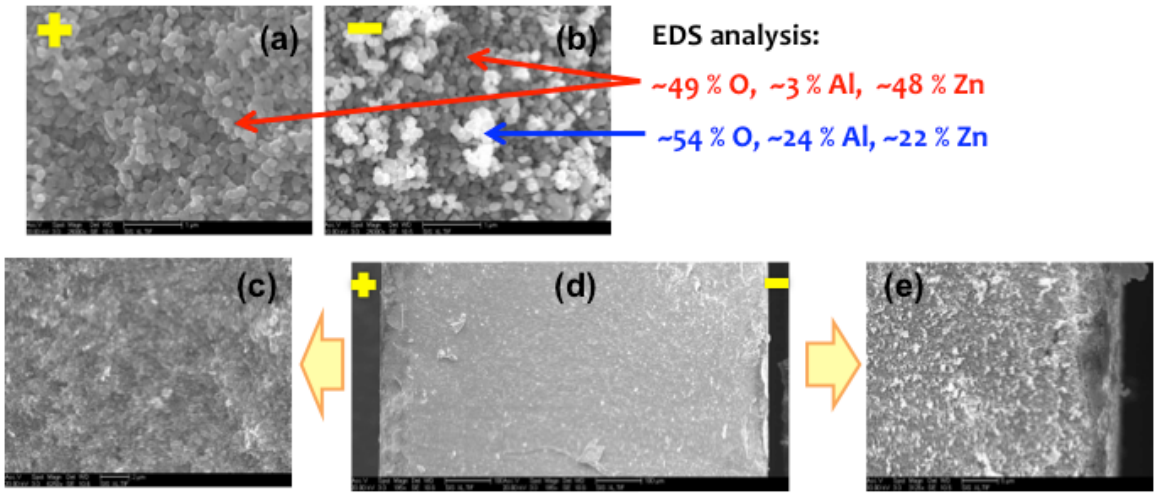


Figure 3.13 (a) and (b) represent SEM images of cross section of AZO specimen after flash sintering in anode and cathode side, respectively. (d) shows the cross section of a whole specimen, (c) and (e) are the enlarged images of anode and cathode area. From EDS analysis, the composition of “grey” particles are ~ 49 mol. % of oxygen, ~ 3 mol.% of aluminum, and ~ 48 mol. % of zinc; the composition of “white” particles are ~ 54 mol. % of oxygen, ~ 24 mol.% of aluminum, and ~ 22 mol. % of zinc. The “white” particles are high Al concentration and it could be Al-Zn-O compound according to phase diagram. The “white” particles are mostly accumulated in cathode area, (b) and (e).

**References:**

[1] D.C. Look 2001 Mater. Sci. Eng. B 80 (2001) 383-387.

[2] N.H.Nickel and E. Terukov Zinc Oxide—A Material for Micro- and Optoelectronic Applications (Netherlands: Springer) 2005

[3] C. Jagadish and S. J.Pearton Zinc Oxide Bulk, Thin Films, and Nanostructures (New York: Elsevier) 2006

[4] X. Jiang, F.L. Wong, M.K. Fung, and S.T. Lee, Appl. Phys. Lett. 83, (2003) 1875-1878.

[5] L.M. Levinson, and H.R. Philipp, Ceram. Bull. 65, (1986) 639-647.

[6] M. Rossinelli, G. Blatter, and F. Greuter, in Electrical Ceramics, vol. 36, ed. by

B.C.H. Steele (Inst. of Ceramics, Shelton, 1985), pp. 1–17.

[7] Y. Lu, N.W. Emanetoglu, and Y. Cheng, in Zinc Oxide. Bulk, Thin films and

Nanostructures, ed. by C. Jagadish, S.J. Pearton (Elsevier, Oxford, 2006), pp. 443–489.

[8] A.H. Kitai, Thin Solid Films 445, (2003) 367-376.

[9] G. Thomas, Nature 389, (1997) 907-908.

[10] I. Satoh, T. Kobayashi, K. Katayma, T. Okada, and T. Itoh, Appl. Phys. A 79, (2004) 1445-1447.

[11] C. Schmerbauch, J. Gonzalez-Julian, R. Roeder, C. Ronning, and O. Guillon, J. Am. Ceram. Soc. 97 (2014) 1728-1735.

[12] S.W. Kim, S.G. Kim, J.I. Jung, S.J.L. Kang, and I.W. Chen, J. Am. Ceram. Soc. 94 (2011) 4231-4238.

[13] R. Raj, J. Eur. Ceram. Soc. 32 (2012) 2293-2301.

[14] R.I. Todd, E. Zapata-Solvas, R.S. Bonilla, T. Sneddon, and P.R. Wilshaw, J. Eur. Ceram. Soc. 35 (2015) 1865-1877.

[15] M.D. McCluskey, and S.J. Jokela, J. Appl. Phys. 106 (2009) 071101.

[16] P.H. Miller, Physical Review 60 (1941) 890-895.

[17] J.P. Han, P.Q. Mantas, and A.M.R. Senos, J. Eur. Ceram. Soc. 22 (2002) 49-59.

[18] S.W. Kim, S.G. Kim, J.I. Jung, S.J.L. Kang, and I.W. Chen, J. Am. Ceram. Soc. 94 (2011) 4231-4238.

[19] H.L. Tuller, Journal of Electroceramics 4 (1999) 33-40.

[20] P.R. Cantwell, M. Tang, S.J. Dillon, J. Luo, G.S. Rohrer, and M.P. Harmer, Acta Mater. 62 (2014) 1-48.

[21] J. Luo, J. Am. Ceram. Soc. 95 (2012) 2358-2371.

[22] W.D. Kaplan, D. Chatain, P. Wynblatt, W.C. Carter, J. Mater. Sci. 48 (2013) 5681-5717.

[23] Y.M. Chiang, E.B. Lavik, and D.A. Blom, Nanostructured Materials 9 (1997) 633-642.

[24] Y.M. Chiang, E.B. Lavik, I. Kosacki, H.L. Tuller, and J.Y. Ying, Appl. Phys. Lett. 69 (1996) 185-187.

[25] I. MacLaren, R.M. Cannon, M.A. Gülgün, R. Voytovych, N.P. Pogrion, C. Scheu, U. Täffner, and M. Rühle, J. Am. Ceram. Soc. 86 (2003) 650-659.

[26] S.J. Dillon, M. Tang, W.C. Carter, and M.P. Harmer, Acta Mater. 55 (2007) 6208-6218

[27] M.P. Harmer, J. Am. Ceram. Soc. 93 (2010) 301-317.

[28] S.J. Dillon, and M.P. Harmer, J. Eur. Ceram. Soc. 28 (2008) 1485-1493.

[29] N.S. Ramgir, D.J. Late, A.B. Bhise, M.A. More, I.S. Mulla, D.S. Joag, and K. Vijayamohanan, J. Phys. Chem. B 110 (2006) 18236-18242.

[30] S.-W. Kim, S.-J.L. Kang, and I.W. Chen, J. Am. Ceram. Soc. 96 (2013) 1090-1098.

[31] S.-W. Kim, S.-J.L. Kang, and I.W. Chen, J. Am. Ceram. Soc. 96 (2013) 1398-1406.

[32] I.W. Chen, S.-W. Kim, J. Li, S.-J.L. Kang, and F. Huang, Advanced Energy Materials 2 (2012) 1383-1389.

[33] M. na, J.S.C. Francis, and R. Raj, J. Eur. Ceram. Soc. 31 (2011) 2827-2837.

[34] R. Muccillo, and E.N.S. Muccillo, J. Eur. Ceram. Soc. 34 (2014) 915-923.

[35] D.R. Clarke, J. Am. Ceram. Soc. 82 (1999) 485-502.

[36] J. Luo, H. Wang, and Y.-M. Chiang, J. Am. Ceram. Soc. 82 (1999) 916-920.

[37] J. Luo, H. Cheng, K.M. Asl, C.J. Kiely, and M.P. Harmer, Science 333 (2011) 1730-1733.

[38] M.P. Harmer, Science 332 (2011) 182-183.

[39] M. Tang, W.C. Carter, and R.M. Cannon, Phys. Rev. Lett. 97 (2006) 075502.

[40] M. Tang, W.C. Carter, and R.M. Cannon, Physical Review B 73 (2006) 024102.

[41] X. Shi, and J. Luo, Physical Review B 84 (2011) 014105.

[42] M. Baram, D. Chatain, and W.D. Kaplan, Science 332 (2011) 206-209.

[43] H. Wang, and Y.-M. Chiang, J. Am. Ceram. Soc. 81 (1998) 89-96.

[44] Y.-M. Chiang, H. Wang, and J.-R. Lee, J. Microsc. 191 (1998) 275-285.

[45] J. Luo, and Y.-M. Chiang, Annu. Rev. Mater. Res. 38 (2008) 227-249.

[46] J. Luo, Y.-M. Chiang, and R.M. Cannon, Langmuir 21 (2005) 7358-7365.

[47] J. Luo, and Y.-M. Chiang, Acta Mater. 48 (2000) 4501-4515.

[48] J. Luo, and Y.-M. Chiang, J. Eur. Ceram. Soc. 19 (1999) 697-701.

# Chapter 4. Flash sintering of ZnO in different atmospheres

## 4.1. Introduction

Flash sintering at ultra-low furnace temperatures can have significant technological advantages, *e.g.*, as an energy-saving fabrication method for consolidating ceramics. In an effort to greatly reduce the flash sintering temperature, Down and Sglavo applied a high electric field of 2250 V/cm to 8 mol. % $Y_2O_3$-stablized $ZrO_2$ (8YSZ); they showed that the onset flash sintering temperature could be decreased to 390 °C, but the specimen could not be sintered to a high density (having achieved only 8.5% linear shrinkage in comparison with achieving a maximum of 28.1% linear shrinkage with a lower applied field/higher onset flash sintering temperature) [1]. While both AC and DC flash sintering ZnO in air has been conducted recently [2,3], this study demonstrated, for the first time to our knowledge, a strong dependence of the onset flash sintering temperature on the atmosphere (air vs. $O_2$, Ar and Ar-$H_2$) using ZnO as a model system, suggesting a new method to control and induce flash sintering. Pursing along this line, we found a set of conditions to flash-sinter ZnO specimens to > 97% of the theoretical density in ~30 seconds at furnace temperatures of < 120 ºC in a reduced hydrogen atmosphere (Ar + 5 mol. % $H_2$).

## 4.2. Experimental

High-purity ZnO powders (>99.99%, purchased from Sigma Aldrich, initial grain size is 30 nm and around 100 nm after burning the binder measured from

the fracture surface of the specimen) were ground in $Al_2O_3$ media for 0.5 hour with 0.5 wt. % of a binder (3 wt. % of PVA dissolved in water). The granulated powders were uniaxially pressed at ~300 MPa to make green specimens with the approximate dimensions: D (diameter) = 6.4 mm and H (height) = 1 mm. The average bulk densities of the green specimens were measured to be 62.0 % (with a standard deviation of 1.0 %). The green specimens were baked at 500 °C for one hour to burn out the binders (with no significant shrinkages). Platinum was sputtered on the both sides of the green specimens using a Denton Discovery 18 Sputter. The sides of the sputtered specimens were slightly grounded by SiC papers after sputtering.

The specimens were then placed in a horizontal tube furnace and attached with Pt wires on both sides to apply an electric field. These flash sintering experiments were conducted either in air or in a flowing gas (Ar, Ar + 5 mol. % $H_2$ and $O_2$, respectively); in the latter case, the furnace tube was purged by the specific gas for half an hour before heating; then, this gas was continuously flowed into the tube furnace during the entire experiments. Similar to a typical flash sintering experiment, the applied voltage was kept a constant until the resultant current reach a preset maximum value ($I_{max}$ = 1 and 4 A, respectively; corresponding to estimated maximum current densities: $J_{max} \approx$ 39 or 153 mA/mm$^2$, respectively), at which point the power source switched from voltage to current control. The electric power source and furnace were shut down after 30 seconds when the power density reached the maximum, and the specimens were cooled down within the furnace. Final bulk densities were

measured by the standard Archimedes method. The microstructure was determined by the field emission environmental scanning electron microscope (SEM, Philips XL30). Grain sizes were measured at the fracture surfaces using a standard intercept method from the SEM micrographs.

## 4.3. Results and discussion

### 4.3.1. Flash sintering in different atmospheres

Fig. 4.1(a) shows the electric power density vs. the furnace temperature ($T_F$) curves for the ZnO samples sintered under an (initial) applied electric field of $E$ = 300 V/cm, with $I_{max}$ being set to 1 A. AC and DC flash sintering ZnO in air has been conducted before [2,3]; in this study, we further conducted flash sintering experiments of ZnO in three different flowing gases (Ar, Ar + 5 mol. % $H_2$, and $O_2$, respectively) to compare the results with that obtained in air under identical $E$ and $I_{max}$ conditions (Fig. 4.1(a)).

The most significant discovery of this study is that the onset flash temperature for the ZnO specimen depends strongly on the sintering atmosphere (Fig. 4.1(a) and Table 4.1). Specifically, sintering in an inert (reducing) Ar atmosphere decreased the onset of flash sintering temperature (from 590 ºC in air) to 236 ºC. Sintering in a more reducing hydrogen atmosphere (Ar + 5 mol. % $H_2$) further lowered the onset of flash sintering temperature to 185 ºC. Consistently, sintering in pure $O_2$ increased the onset flash sintering temperature slightly (from 590 ºC in air) to 611 ºC.

The dependence of the onset flash sintering temperature on the atmosphere can be explained from the increased conductivities of ZnO in reducing atmospheres. To illustrate this, we plotted the conductivity (in a logarithmical scale) vs. the reciprocal of (absolute) specimen temperature curves in Fig. 4.1 (b) for the virtually identical ZnO powder specimens measured in four different atmospheres (before the occurrence of a flash event); here, the specimen temperatures ($T_S$) were estimated from a black-body radiation model proposed by Raj [4], which are also listed in Table 4.1. In all cases, the temperature-dependent conductivities follow an Arrhenius relation (see Chapter 4.3.2). Fig. 1(b) (as well as Table 4.2) shows that the activation energy is lower for specimens measured in reduced atmospheres (Ar and Ar + 5 mol. % $H_2$). Consequently, the conductivity can be increased substantially to trigger flash events at much lower temperatures in reduced atmospheres (Ar and Ar + 5 mol. % $H_2$).

In fact, it is well documented that the electric conductivity of (dense) polycrystalline ZnO specimens would increase with decreasing oxygen partial pressures [5]. Increases of the conductivities of ZnO in $H_2$ have also been reported [6,7]. First-principle calculations [8-10] further suggested that the hydrogen interstitials could be shallow donors; thus, the incorporation of hydrogen into ZnO may further increase the conductivity by doping in addition to the simple reduction effects to further lower the onset flash sintering temperature.

While the initial densities of all green specimens were around 62 %, the final densities after the flash sintering are 64.0%, 69.0%, 97.5% and 94.8%, for

specimens flash-sintered in Ar + 5 mol. % $H_2$, Ar, Air and $O_2$, respectively, for ~ 30 seconds with the experimental conditions of $E$ = 300 V/cm and $I_{max}$ = 1 A (Table 4.1). This suggests that although the ZnO specimens have been successfully sintered to high densities in Air and $O_2$, the densification was limited for specimens sintered in Ar and Ar + 5 mol. % $H_2$ under this specific set of experimental conditions. The estimated specimen temperatures at the activated states (the steady state after the onset flash) from the Raj model [4] were 1083 ºC and 1169 ºC, respectively, for specimens flash-sintered in Air and $O_2$, respectively; however, estimated specimen temperatures were only 783 ºC and 943 ºC, for specimens sintered in Ar + 5 mol. % $H_2$ and Ar, respectively (Table 4.1). The significantly lower specimen temperatures for the two latter cases explain the low densification in Ar + 5 mol. % $H_2$ and Ar with the specific experimental conditions of $E$ = 300 V/cm and $I_{max}$ = 1 A (Table 4.1).

### 4.3.2. Application of thermal runaway model in different atmosphere

Based on the measurements conducted on high-purity ZnO powder specimens before the occurrence of the “flash” events in all four different atmospheres, we plotted the logarithmic conductivity vs. the reciprocal of the specimen (absolute) temperature curves in Fig. 4.1(b) in the main text, which are virtually linear lines. Thus, the measured temperature-dependent conductivities follow an empirical Arrhenius equation:

$$\sigma(T) = \sigma_0 \cdot e^{-\frac{h}{kT}}, \tag{4.1}$$

where $h$ is the activation enthalpy, $k$ is the Boltzmann constant, and $\sigma_0$ is a constant. The parameters $h$ and $\sigma_0$ in Eq. (4.1) can be obtained by linear regressions of $\ln[\sigma(T)]$ vs. $1/kT$ for each of the four cases; the obtained results are listed in Table 4.2 and used subsequently in a thermal runaway model to predict the onset flash temperatures.

A thermal runaway model was proposed independently in two prior studies and successfully applied to ZnO [Chapter 3] and 3YSZ [11], respectively, to predict the onset flash sintering temperatures in air. This phenomenological thermal runaway model explained how the flash sintering starts in at least these two specific systems (but not how densification occurs). This model has been discussed in the Chapter 2 and subsequently we apply it to analyze the data collected in the new flash sintering experiments of ZnO conducted in different atmospheres.

This model, using the measured conductivity vs. temperature functions, can predict the thermal runaway temperatures that are consistent with the observed onset flash sintering (furnace) temperatures for experiments conducted in all four atmospheres with high accuracies, as shown in the Fig. 4.2. Thus, this thermal runaway model (discussed in the Chapter 2) quantitatively demonstrates that the decreases in the onset flash sintering temperatures in Ar and Ar + 5 mol. % $H_2$ are the results of the increased conductivities at lower temperatures (Fig. 4.1(b)) in the reduced atmospheres (Fig. 4.1(b)) [5-7] while the incorporation hydrogen interstitials as shallow donors [8-10] may help further.

Using an Arrhenius temperature-dependent conductivity function (Eq. (3.2)) and the parameters obtained from fitting the measured conductivities of the high-purity ZnO powder specimens in the four different atmospheres (Table 4.2), we calculated the differentiate heat generation rates (the left side of Eq. (2.8) in Chapter 2) vs. specimen temperature curves for ZnO powder specimens in these four different atmospheres and plotted them as the (black, blue, pink and red) dotted lines in Fig. 4.2. In the same figure, we also plotted the differentiate heat generation rate ($\alpha$) vs. specimen temperature curve calculated based on the specific specimen geometry and $E$ = 300 V/cm, assuming the heat dissipation was dominated by the black-body radiation (as a simplification), as represented by the grey solid line in Fig. 4.2.

Thus, the intercepts of the curves of differentiate heat generation and dissipation rates (dotted and solid lines) in Fig. 4.2 represent the thermal runaway conditions indicated by Eq. (2.8) in Chapter 2, above which more heat is generated than that can be dissipated, leading to unstable temperature rises or the onset of the flash events. Subsequently, we further estimated the furnace temperatures ($T_F$) at the onset of the flash (thermal runaway) events from the predicted specimen temperatures (the intercepts in Fig. 4.2 using the Raj model [4] and reported them, along with experimentally-measured $T_F$, in the four panels in Fig. 4.2.

On one hand, the accurate agreements between the predicted and observed $T_F$ values support that the flash indeed starts as thermal runaway events. This model-experiment agreement (Fig. 4.2) has further testified

quantitatively and powerfully that the reduced onset flash sintering temperatures were results of the significant increased conductivities in reducing atmospheres and/or a hydrogen environment (as shown in Fig. 4.1(b)).

On the other hand, the somewhat surprisingly accurate agreements between the predicted and observed $T_F$ values, which are with 1 °C for all four cases, are in part due to the facts that the two mostly significant errors of the models are largely canceled when predicting $T_F$. First, we measured the conductivities of the powder specimens in situ in the same furnace for conducting the flash sintering experiments; thus, any errors resulted from the temperature measurements of the furnace are canceled. Second, the most significant approximation of this model is the use of a simple black-body radiation model to estimate the heat dissipation, which ignore the heat conduction and convention contributions that can often be important. However, the black-body radiation model was used twice to estimate the specimen temperature at the thermal runaway and then the furnace temperature from the estimated specimen. Thus, an over (or under) estimation will occur twice with opposite signs in estimating the final $T_F$, where the error is partially canceled each other, resulting a more accurate estimation of the $T_F$ (than that of $T_S$). Finally, the exponential nature of the thermal runaway also makes the prediction less sensitive to other errors.

Finally, we should note that for the experiment conducted in Ar + 5 mol. % $H_2$, the prediction from the simple Arrhenius extrapolation (the red dotted line in Fig. 4.2) would suggest the flash would not have been sustained (in contrast to the three other cases) since the heat generation would fall below the heat

dissipation line shortly after the interception. In real experiment, the flash was sustained in Ar + 5 mol. % $H_2$; this discrepancy can be readily understood, as explained subsequently. In Ar + 5 mol. % $H_2$, a chemical equilibrium can often be hindered at low temperatures due to the slow kinetics of reduction and incorporating hydrogen into ZnO. After the onset of flash, more hydrogen can react with and/or be incorporated into ZnO to further enhance the conductivity beyond the simple Arrhenius extrapolation or the red dotted line in Fig. 4.2. Thus, the flash sintering can be sustained (with additional increases of the conductivities beyond the simple Arrhenius extrapolation, as indicated by the red error in Fig. 4.2); nonetheless, achieving a high density requires a high applied field/current, as discussed in the next section.

### 4.3.3. Achieving >97% relative density at furnace temperature of <120 ºC

To further reduce the onset flash sintering temperature and simultaneously increase the densification, we conducted four additional flash sintering experiments of ZnO powder specimens in Ar + 5 mol. % $H_2$ at higher applied electrical fields ($E$ = 500 V/cm and 1000 V/cm) with a greater maximum current limit ($I_{max}$ = 4 A or $J_{max}$ = 153 mA/mm$^2$). Two specimens were prepared for each condition.

Fig. 4.3 shows the electric powder density vs. furnace temperature curves for the flash sintering of ZnO powder specimens in Ar + 5 mol. % $H_2$ with the experimental conditions of $E$ = 500 or 1000 V/cm and $I_{max}$ = 4 A; the relevant results are also summarized in Table 4.1. Specifically, the onset of flash

temperatures were measured in the range of 110 to 130 ºC (with ~20 ºC specimen-to-specimen variations) with the higher applied electric fields. We observed that the Pt sputtered on the specimen was melted after flash sintering (the melting temperature of Pt is 1772 ºC), so the actual specimen temperature should be higher than that (Fig. 4.4). The final sintered densities were measured to be in the range of ~90-98 % of the theoretical density. Two best specimens achieved >97 % of the theoretical density.

It is interesting to note that the onset flash sintering temperature is almost the same with the applied electric field of 500 V/cm or 1000 V/cm. Presumably, at such lower temperatures, the kinetics for the reduction reaction of ZnO with the hydrogen gas, as well as the possible incorporation of hydrogen interstitials, is limited. Thus, a higher applied electric field will not help further, and the flash will not start until reaching certain minimum temperature (~110-130 ºC) when the ZnO can be partially reduced to have sufficient conductivity. This hypothesis is consistent with experimental observations (Fig. 4.3). In addition, this evidence is also consistent with the earlier report [11].

Fig. 4.5 shows the microstructures of the fractured surfaces of the flash-sintered specimens (with the experimental conditions: $E$ = 500 V/cm and 1000 V/cm; $I_{max}$ = 4A; 30 seconds). The grain sizes were measured to be 1.0 ± 0.3 μm at the anode side and 0.9 ± 0.3 μm at the cathode side, respectively, for the specimens flash-sintered at 500 V/cm. The grain sizes were measured to be 1.4 ± 0.5 μm at the anode side and 1.3 ± 0.4 μm at the cathode side, respectively, for the specimens flash-sintered at 1000 V/cm. It is interesting to note that the grain

sizes are virtually identical at the anode and cathode sides in the current cases. This differs from prior report of the specimens flash-sintered at a lower applied electric field of $E$ = 300 $Vcm^{-1}$ in air, where an abnormal grain growth and/or coarsening at anode-side was observed [3]. This is presumably due to a reduction effect in Ar + 5 mol. % $H_2$ that offsets the selected grain boundary oxidation at the anode size in air, as proposed as the underlying mechanism for the anode-side grain boundary (complexion [12]) transition and abnormal grain growth in the prior study [3].

### 4.4. Conclusions

In summary, this study demonstrated the onset flash sintering temperature of ZnO can be significantly decreased in reducing atmospheres. This discovery of significant dependence of flash sintering behaviors on atmosphere suggests a new method to control flash sintering via controlling the sintering atmosphere. A set of experimental conditions have been found, enabling the high-purity ZnO powder specimens to be flashed sintered to > 97% of the theoretical density with fine grain sizes of ~ 1 μm in ~30 seconds at furnace temperatures of <120 ºC in Ar + 5 mol. % $H_2$. The significant decreases in the onset flash sintering temperatures in reduced atmospheres can be well explained from increased conductivities of ZnO, as quantitatively supported by a thermal runaway model detailed in the chapter 2 & 3.

Chapter 4, in full, is a reprint of the material “Promoting the flash sintering of ZnO in reduced atmospheres to achieve nearly full densities at furnace

temperatures of <120 ºC” as it appears in the Scripta Materialia, Yuanyao Zhang, Jian Luo, Scripta Materialia, 2015, 106, 26-29. The dissertation author was the primary investigator and author of this paper. All experiments and data analysis were performed by the author.

Table 4.1 Summary of the key experimental results of the flash sintering of ZnO in different atmospheres. The specimen temperatures ($T_S$) were estimated from the Raj model [4].

| Flash Sintering Conditions | Atmosphere | Sintered Relative Density | Before the Flash (Onset Flash) | | In the Flash State |
|---|---|---|---|---|---|
| | | | Furnace Temperature ($T_F$, ºC) | Estimated Specimen Temperature ($T_S$, ºC) | |
| $E$ = 300 V/cm, $I_{max}$= 1A | Ar + 5 mol.% $H_2$ | 64.0% | 185 | 305 | 783 |
| | Ar | 69.0% | 236 | 341 | 943 |
| | Air | 97.5% | 590 | 624 | 1083 |
| | $O_2$ | 94.8% | 611 | 639 | 1169 |
| $E$ = 500 V/cm, $I_{max}$= 4A | Ar + 5 mol. % $H_2$ | 97.4% | 108 | 240 | > 1772 |
| | | 90.1% | 127 | 275 | > 1772 |
| $E$ = 1000 V/cm, $I_{max}$= 4A | | 97.7% | 116 | - | > 1772 |
| | | 93.0% | 120 | - | > 1772 |

Table 4.2 The *h* and $\sigma_0$ values in Eq.4.1 obtained by Arrhenius fittings of the temperature-dependent conductivities of the ZnO powder specimens measured in four different atmospheres (as shown in Fig. 4.1(b)) and the corresponding correlation factors.

| **Atmosphere** | **$\sigma_0$ (S/cm)** | **Activation Enthalpy (eV)** | **Correction Factor ($R^2$)** |
|---|---|---|---|
| Ar + 5 mol. % $H_2$ | 0.0454 ± 0.0012 | 0.298 ± 0.001 | 99.99% |
| Ar | 0.1804 ± 0.0196 | 0.384 ± 0.006 | 99.89% |
| Air | 7768 ± 1935 | 1.395 ± 0.020 | 99.84% |
| $O_2$ | 584 ± 320 | 1.218 ± 0.048 | 99.74% |

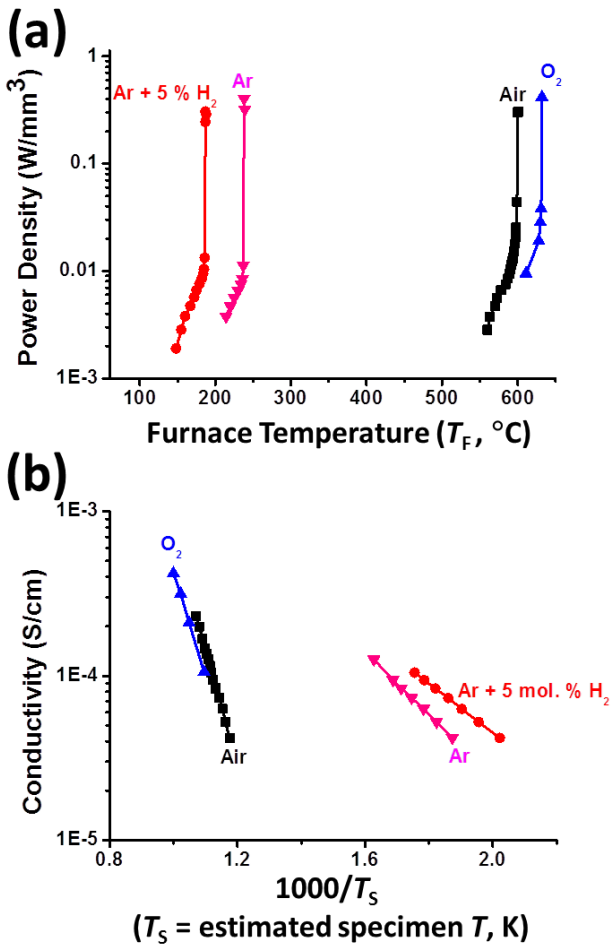


Figure 4.1 (a) Measured electric power dissipation vs. furnace temperature curves for the flash sintering of ZnO in four different atmospheres. (b) Measured conductivity vs. the reciprocal of the estimated specimen temperature curves.

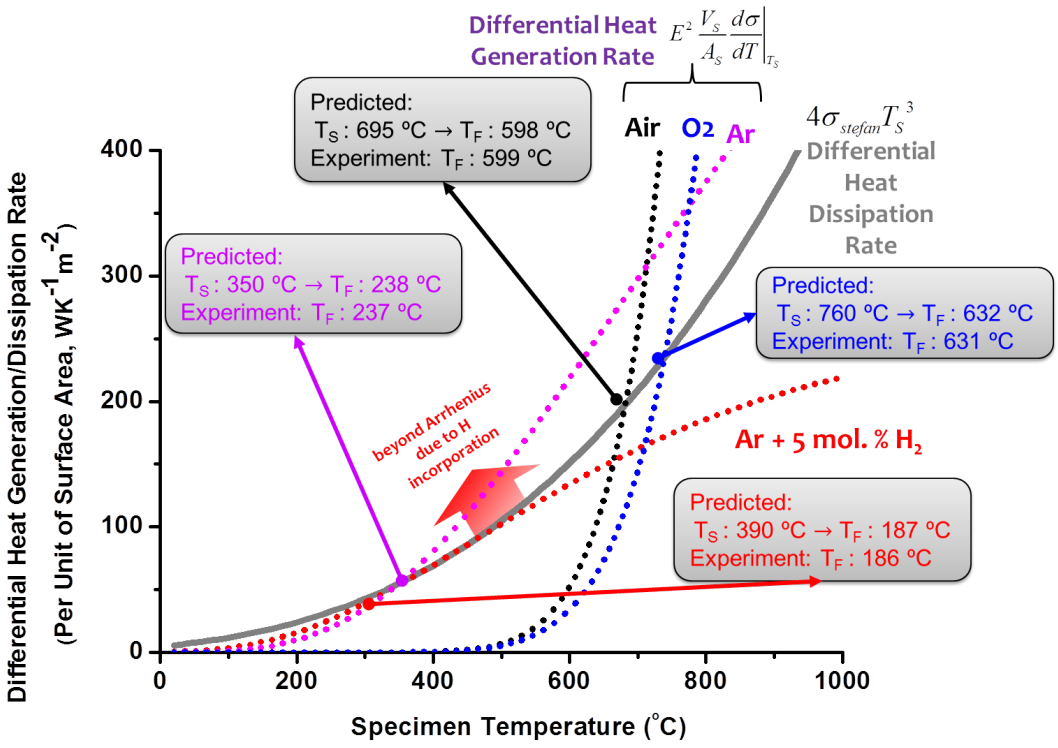


Figure 4.2 Computed differential heat generation rates vs. specimen temperature curves for the ZnO powder specimens in four different atmospheres (represented by the black, blue, pink, and red dotted lines, respectively), along with the computed differential heat dissipation rate vs. specimen temperature curve (represented by the grey solid line). The intercepts of the solid and dotted lines represent the specimen temperatures ($T_S$) for the onsets of thermal runaway, above which more heat is generated than that can be dissipated. The furnace temperatures ($T_F$) at the onset thermal runaway were then estimated based on the Raj model [4], which agree with experimentally-measured onset flash sintering temperatures for all four cases. It is important to note that for the experiment conducted in Ar + 5 mol. % $H_2$, the conductivity may be further enhanced beyond that is predicted from the simple Arrhenius extrapolation since more hydrogen can be incorporated into ZnO after the onset of flash to further enhance the conductivity beyond the red dotted line; see text for elaboration.

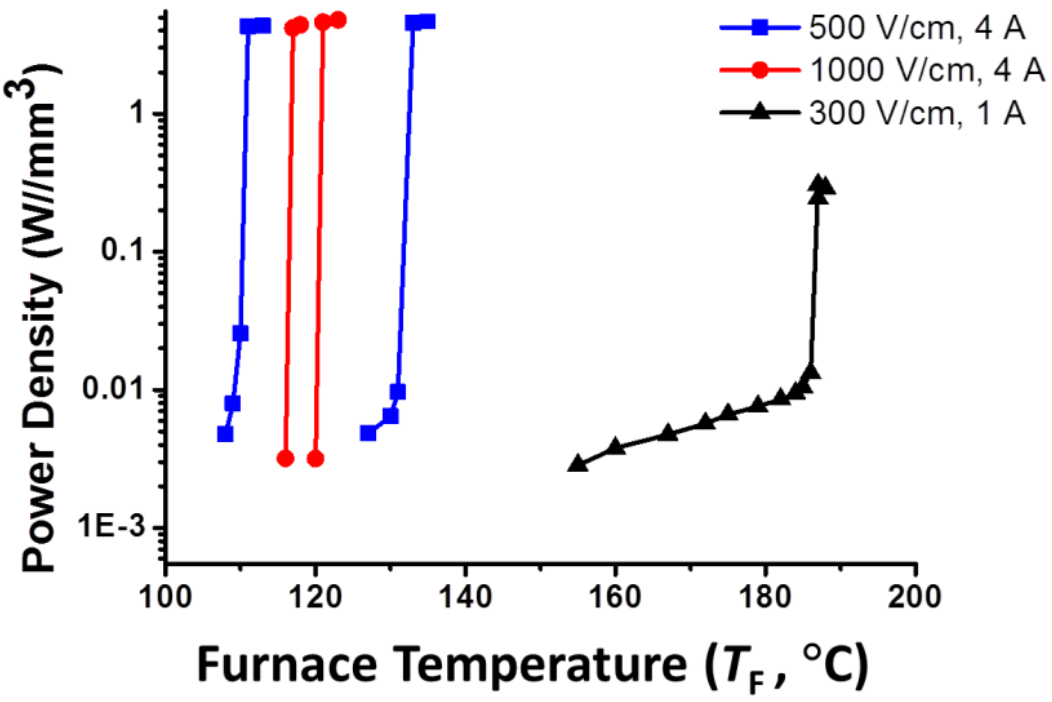


Figure 4.3 Measured electric power dissipation vs. furnace temperature curves for the flash sintering of ZnO in Ar + 5 mol. % $H_2$ with different applied electric fields.

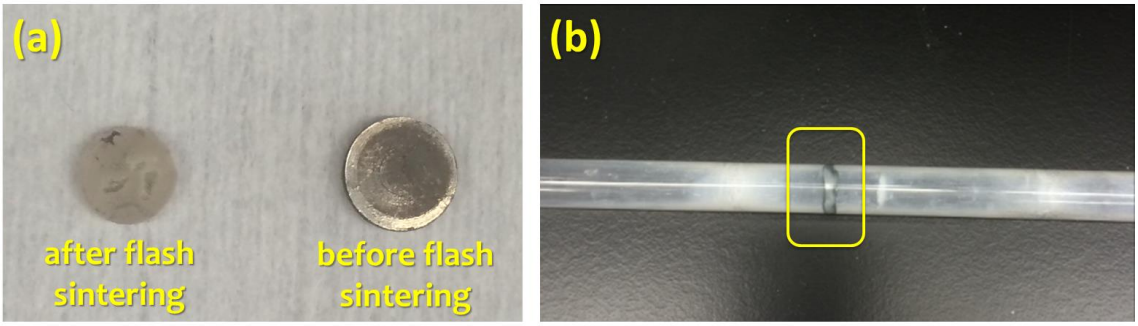


Figure 4.4 Images of (a) a specimen before and after flash sintering, indicating the Pt electrode sputtered on the specimen melted and (b) the surrounding tube after the flash sintering, where the residue of melted Pt was evident.

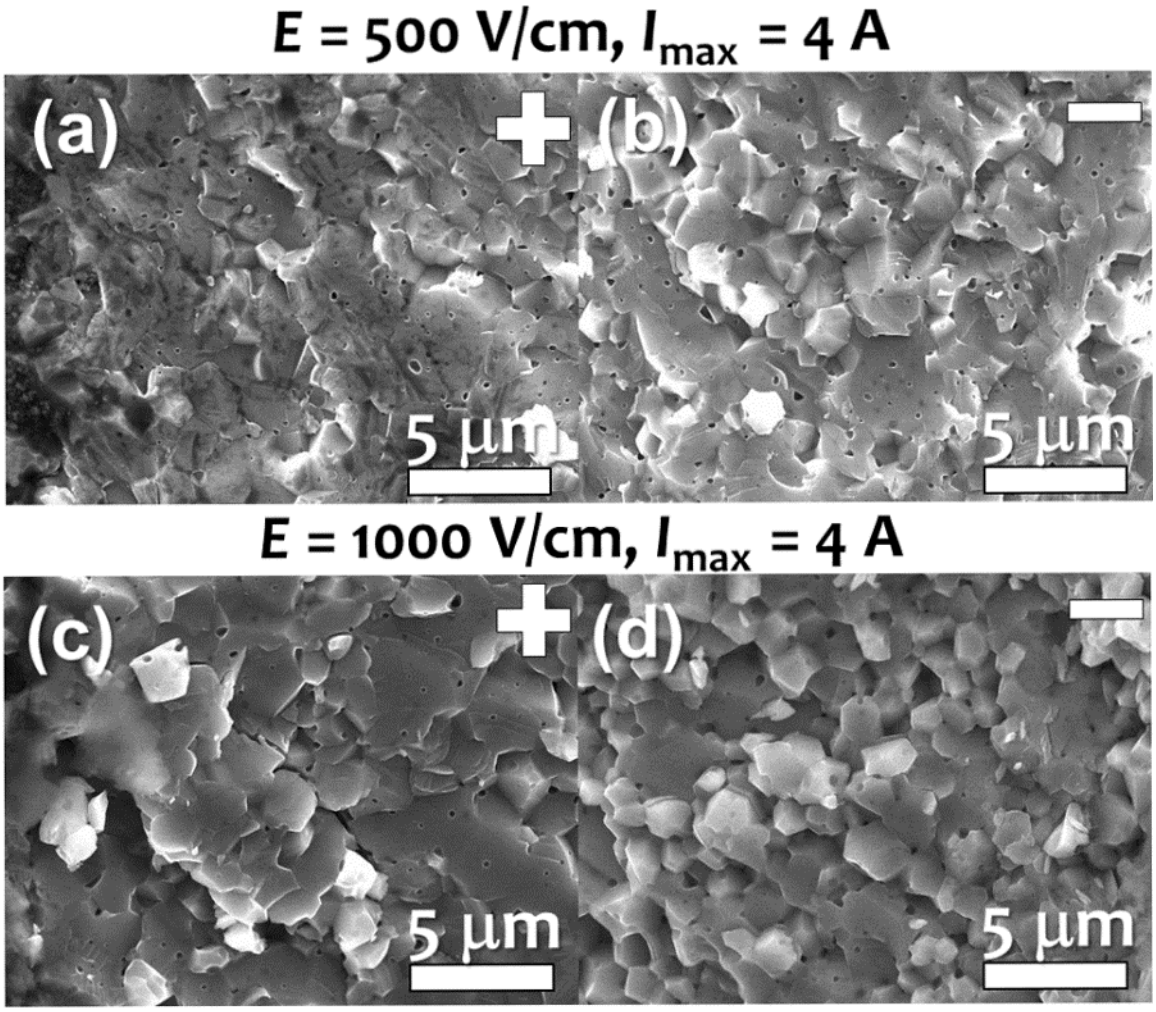


Figure 4.5 SEM micrographs of the (a, c) anode and (b, d) cathode sides of the fractured surfaces of flash-sintered ZnO specimens, where the initial applied electric field was set to be (a, b) 500 V/cm and (c, d) 1000 V/cm, respectively.

**References:**

[1] J. A. Down, and V. M. Sglavo, J. Am. Ceram. Soc. 96 (2013) 1342-1344.

[2] C. Schmerbauch, J. Gonzalez-Julian, R. Roeder, C. Ronning, and O. Guillon, J. Am. Ceram. Soc. 97 (2014) 1728-1735.

[3] Y. Zhang, J.I. Jung, and J. Luo, Acta Mater. 94 (2015) 87-100.

[4] R. Raj, J. Eur. Ceram. Soc. 32 (2012) 2293-2301.

[5] J. Lee, J. H. Hwang, J. J. Mashek, T. O. Mason, A. E. Miller, and R. W. Siegel, J. Mater. Res. 10 (1995) 2295-2300.

[6] S. J. Baik, J. H. Jang, C. H. Lee, W. Y. Cho, and K. S. Lim, Appl. Phys. Lett. 70 (1997) 3516-3518.

[7] S. Kohiki, M. Nishitani, T. Wada, and T. Hirao, Appl. Phys. Lett. 64 (1994) 2876-2878.

[8] C. G. Van de Walle, and J. Neugebauer, Nature 423 (2003) 626-528.

[9] C. G. Van de Walle, Phys. Status Solidi B 235 (2003) 89-95.

[10] A. Janotti, and C. G. Van de Walle, Nat. Mater. 6 (2007) 44-47.

[11] R.I. Todd, E. Zapata-Solvas, R.S. Bonilla, T. Sneddon, and P.R. Wilshaw, J. Eur. Ceram. Soc. 35 (2015) 1865-1877.

[12] P.R. Cantwell, M. Tang, S.J. Dillon, J. Luo, G.S. Rohrer, and M.P. Harmer, Acta Mater. 62 (2014) 1-48.

# Chapter 5. Effects of phase and doping on flash sintering of TiO2

## 5.1. Introduction

Raj and co-workers invented “flash sintering” as a novel sintering technology that enables rapid densification at low furnace temperatures [1,2]. Recent studies showed that flash sintering could be applied to a variety of materials, including nominally-pure oxides of ZnO [3-5], $ZrO_2$ [6], $TiO_2$ [7], and $Y_2O_3$ [8], as well as $Y_2O_3$-doped $ZrO_2$ [9], $Bi_2O_3$-doped ZnO [4], MgO-doped $Al_2O_3$ [10], $MnO_2$-doped $SnO_2$ [11], $Gd_2O_3$-doped $CeO_2$ [12], and SiC-$Al_2O_3$-$Y_2O_3$ composites [13]. In a typical flash sintering experiment, an (initially-constant) electric field is applied to a specimen that is placed in a furnace; then, the furnace temperature is increased at a constant ramp rate, until the occurrence of an “flash” event with a sudden increase of the electric current, leading to an abrupt rise in the specimen temperature; after a few seconds, the power control switches from a constant-voltage to a constant-current mode with a pre-set maximum current that limits the steady-state temperature during the sintering; the specimen is typically kept for a few seconds at this steady state before the sintering is completed.

Recently, we proposed that the onset flash occurs as a coupled thermal and electric runaway [3, 4]. We further developed a quantitative model that can accurately predict the onset flash temperatures, where we used ZnO in several different oxidizing and reducing atmospheres as the model systems to test and

validate this proposed model [3, 4]. Similar thermal runaway models have been proposed by Todd et al [14]. and by Dong and Chen [15,16], which are based on the same physical concepts but used somewhat different mathematical approaches to solve the thermal runaway conditions (noting that the reports [14,15] from both groups were submitted after the initial submission, but before the publication, of our first report of this quantitative thermal runaway model [4]; thus, all three models [4,14,15] have been developed independently).

Jha and Raj first reported the flash sintering of nominally-pure rutile $TiO_2$ [7]. In this study, we further investigated the flash sintering of both rutile and anatase $TiO_2$ specimens, including nominally-pure (undoped) specimens as well as representative cation (V) and anion (N) doped specimens with approximately identical starting particle sizes and green densities. Specifically, we showed that six $TiO_2$ specimens have different temperature-dependent conductivities, leading to different onset flash sintering temperatures. We have further demonstrated that the coupled thermal and electric runaway temperatures predicted from our prior quantitative model [4] agree with the observed onset flash temperatures within <5 °C for all six cases, which critically supports our prior model [4]. Finally, we also demonstrated that the initial phase and doping can critically affect the microstructural development during the flash sintering.

### 5.2. Experimental

Anatase (99.98% purity, ~30 nm particle size) and rutile (99.9% purity, ~30 nm particle size) powders were purchased from US Research

Nanomaterials. Inc (Houston, TX, USA). To prepare V-doped powders, we adopted a well-established procedure to make $TiO_2$-supported $V_2O_5$ monolayer catalysts [17,18]. Specifically, the pure anatase or rutile powder was mixed with an aqueous solution of $NH_4VO_3$ and $NH_4OH$ and dried in oven at 85 °C for 12 hours. Then, the mixed powders were annealed at 220 °C for 3 hours (to remove moisture), at 450 °C for 3 hours in an open container, and at 500 °C for 4 hours in a closed container; the annealed powders were subsequently air quenched.

N-doped $TiO_2$ powders were prepared by annealing $TiO_2$ powders in flowing ammonia following a surface nitridation procedure in Ref. [19]. Specifically, the pure anatase or rutile powder was placed in a tube furnace and purged with argon for 1 h. The powders were annealed at 250 °C for 1 h to remove moisture, before the furnace temperature was raised to 450 °C and the flowing gas was switched to ammonia. Subsequently, the specimens were annealed in flowing ammonia isothermally for 7 hours and cooled in furnace with flowing argon.

Six different powders, including un-doped, N-doped, and V-doped anatase and rutile, were used to prepare specimens for flash sintering experiments. All powders were uniaxially pressed at ~200 MPa to make green specimens with the approximate dimensions: *D* (diameter) = 6.4 mm and *H* (height) = 1 mm. The average bulk densities of the green specimens were measured to be ~45 % of the theoretical density. The relatively low green densities were due two reasons, as follows. First, the green specimens were pressed at a relatively low pressure of 200 MPa to make sure the specimen surfaces were flat and specimens are

homogenous. Second, we used nanosized powders, which also contributed to the low green densities. However, we emphasize that the low green densities should not influence the comparison of the flash sintering results because all six specimens had roughly identical green densities. Pt electrodes were sputtered on both sides of green specimens using a Denton Discovery 18 sputtering system and the surrounding areas were slightly grounded. The specimens were placed in a horizontal tube furnace and attached with Pt wires on both sides. In the flash sintering experiments, an initially-constant electric field of 500 V/cm was applied, and the specimens were heated with a constant ramp rate of 5°C per minute. In each individual experiment, a flash event occurred, after which the electric power source switched from the constant-voltage control mode to the constant-current control mode with a pre-set maximum value of $I_{max}$ = 0.5 A (corresponding to an estimated current density of $J_{max} \approx 20$ mA/mm$^2$). Subsequently, the furnace and the power supply were shut down ~30 seconds after the current reached the maximum value, and the specimens were cooled in the furnace. Final bulk densities were measured by the standard Archimedes method. The microstructures were characterized by a FEI ultra-high resolution scanning electron microscope (SEM, Hillsboro, OR, USA). The specimens were characterized by X-ray diffraction (XRD) using a Rigaku (Tokyo, Japan) RU 200-BH diffractometer.

As we will show later, all anatase specimens were converted to the rutile phase after the flash sintering, but they are often referred to as un-doped, V-

doped and N-doped anatase specimens (based on the starting phase) to differentiate them from those specimens prepared by the rutile powders.

## 5.3. Results and discussion

### 5.3.1. Specimen conductivities and their effects on onset flash sintering

Fig. 5.1(a) displays the electric power density vs. the furnace temperature ($T_F$) curves for the six specimens (i.e., un-doped, N-doped, and V-doped anatase and rutile) during the flash sintering experiments. Fig. 5.1 (b) shows the Arrhenius plots of measured conductivities of the same six specimens, where specimen temperatures were estimated from the black-body radiation model following the work of Raj [20]. There is a clear correlation between the measured specimen conductivities (Fig. 5.1a) and flash sintering behaviors (Fig. 5.1b); higher conductivities lead to the occurrence of flash sintering at lower temperatures.

As shown in Fig. 5.1 and summarized in Table 5.1, the onset flash sintering temperature of undoped anatase (768 °C) was appreciably lower than that of undoped rutile (831 °C). The cation doping of vanadium (V) consistently reduced the onset flash sintering temperatures of both rutile and anatase specimens (Fig. 1(a)) by substantially increasing the conductivities (Fig. 5.1(b)). Specifically, V doping reduced the onset flash sintering temperature of the anatase specimen by >100 °C from 768 °C to 665 °C, and it reduced the onset flash sintering temperature of the rutile specimen by >150 °C from 831 °C to 672 °C. Interestingly, the effects of anionic doping of nitrogen (N) were different for

anatase and rutile specimens; N doping increased the onset flash sintering temperature of the anatase specimen by ~50 °C, from 768 °C to 818 °C, but decreased the onset flash sintering temperature of the rutile specimen by ~57 °C, from 831 °C to 774 °C.

The effects of phase and doping on changing conductivities and subsequently onset flash sintering temperatures are worthy some further discussion. According to our model (that will be discussed in detail below), the onset flash sintering temperature depends solely on the temperature-dependent conductivities of the actual specimens, which in turn depend on both the intrinsic bulk conductivities as well as the surface and grain boundary conductivities, particle sizes, and porosity. Anatase has higher conductivities than rutile so that the flash sintering of anatase specimens started at lower temperatures. Cation doping with V (that is typically an electron donor for $TiO_2$) will increase the conductivities of both anatase and rutile substantially, promoting the flash sintering in both materials. N doping has opposite effects on anatase and rutile; it increases the rutile conductivities (promoting the flash sintering) but decreases the anatase conductivities (deferring the flash sintering). This may be explained by different surface vs. bulk doping effects; further investigations are warranted to clarify the exact mechanisms.

### 5.3.2. The coupled thermal and electric runaway model for predicting the onset flash sintering temperatures

Although the effects of starting phase and doping on the conductivities of $TiO_2$ specimens are rather complex, this study demonstrated that the measured conductivities can be used to predict the coupled thermal and electric runaway temperatures using a recently-developed quantitative model [3,4] that agree well with the observed onset flash sintering temperatures in all six cases, as follows. In this model [3,4], the rise of specimen temperature is determined by the energy conservation law. The specific conditions for stable and unstable temperature rises are elaborated as described in Chapter 2.

The equation (2.8) in Chapter 2 can be solved graphically by plotting $E^2V_S(d\sigma/dT)_{T_S}$ and $4\sigma_{\text{Stefan}}T_S^3A_s$ vs. $T_S$ curves and finding their intersections to obtain the specimen temperature ($T_S$) at the onset flash/thermal runaway, as shown in Fig. 2 for the six cases of $TiO_2$ based systems in this study as well as for ZnO based systems in two prior studies [3, 4]. Subsequently, the corresponding furnace temperature ($T_F$) can be solved from $T_S$ using Eq. (3.1). It is worth noting that the thermal runaway models proposed slightly later by Todd et al. [14] and by Dong and Chen [15, 16] were essentially based on the same physical concepts as this (our prior) model [3, 4], although the specific mathematical approaches (the specific equations and methods used) to solve the onset flash sintering (thermal runaway) temperatures are somewhat different.

Fig. 5.2 shows the computed differential heat generation rates ( $E^2V_S(d\sigma/dT)_{T_S}$ ) vs. specimen temperature ($T_S$) curves for the six $TiO_2$ specimens, which were calculated based on the Arrhenius fitting of the

conductivities shown in Fig. 5.1(b). In Fig. 5.2, we also plot the computed differential heat dissipation rate ($4\sigma_{\text{Stefan}}T_S^3A_s$) vs. specimen temperature curve (the grey solid line). The intersections of the solid and dotted/dashed lines represent the specimen temperatures ($T_S$) at the occurrences of coupled thermal and electric runaways; subsequently, the corresponding furnace temperatures ($T_{F,0}^{(\text{predicted})}$) were estimated using Eq. (3.1), assuming ideal black body radiation. These predicted furnace temperatures ($T_{F,0}^{(\text{predicted})}$) are consistent with observed onset flash temperatures ($T_{F,0}^{(\text{exp})}$) within 5 °C for all six cases (Fig. 5.2 and Table 5.1).

The excellent agreements to somewhat surprisingly-high precisions (<5 °C in these six cases) are due to several factors discussed in the prior report, [4] e.g., the errors of temperature measurements by the thermocouple were largely canceled since we used the conductivities that were measured *in situ* for the prediction. The exponential dependence of conductivities on temperature also made the prediction less sensitive to other errors. The predicted $T_{F,0}^{(\text{predicted})}$ values are lower than the observed onset flash temperatures for all six cases, which are likely due to the non-linearity in Fig. 5.1(b) (that is presumably due to the partial sintering of $TiO_2$ specimens before the onset of flash); thus, the extrapolations underestimated the specimen conductivities slightly in general because of the concave curvatures in Fig. 5.1(b). Nonetheless, the excellent agreements between predicted $T_{F,0}^{(\text{predicted})}$ and observed $T_{F,0}^{(\text{exp})}$ for all six cases provided a further strong support for the recently-developed quantitative model

for predicting onset flash temperatures [3, 4], and attested that the flashes also start as coupled thermal and electric runaway for these six $TiO_2$ based specimens with different starting phase and doping.

### 5.3.3. Densification

The relative densities after flash sintering and estimated specimen temperatures in the steady states (during the ~30 seconds' sintering after the current reached the maximum value) are listed in Table 5.1. The densities of undoped anatase and rutile specimens after ~ 30 seconds of flash sintering were 95% and 97%, respectively, of the theoretical density of the rutile phase. The final density of the specimen that was made of the undoped anatase powder was slightly lower than that made of the undoped rutile powder initially, which may be related to the anatase-to-rutile phase transformation that is associated with a volumetric shrinkage. The anionic doping of N reduced the final densities to 92% (for the anatase specimen) and 87% (for the rutile specimen), respectively, while the estimated temperatures in steady states are comparable (Table 5.1). The cationic doping of V reduced the onset flash sintering temperatures of the anatase and rutile specimens substantially; the estimated temperature in the steady state is 992 °C for the V-doped anatase specimen (being lower than that for the undoped anatase specimen), which resulted in a lower relative density of 86 %; in contrast, the estimated temperature in the steady state for the V-doped rutile specimen is 1078 °C, which is similar to that for the undoped rutile

specimen; thus, the flash-sintered V-doped rutile specimen also has a high relative density of ~96 %.

### 5.3.4. Phase transformation during flash sintering for anatase specimens

XRD patterns in Fig. 5.3 show that all three anatase specimens transferred to the rutile phase after the flash sintering. For brevity, these specimens are still called as un-doped, V-doped, and N-doped anatase specimens (according to the phase in initial powders before flash sintering), to differentiate them from the specimens prepared by un-doped, V-doped, and N-doped rutile powders.

### 5.3.5. Microstructures

Fig. 5.4 shows the microstructures of the fractured surfaces of the six flash-sintered specimens. Although the undoped anatase and rutile specimens (noting they both contain the rutile phase after flash sintering) have similar estimated temperatures in their steady states, their microstructures are different. The flash-sintered undoped anatase specimen have (clustered) secondary particles of 1.11 (mean) ± 0.12 (one standard deviation) μm, which are composed of smaller primary grains, the boundaries of which are not clearly distinguishable in the SEM image (Fig. 5.4a) so that we cannot measure the exact grain size; this meatball-like microstructure (with hierarchical primary and secondary particles/grains at two different length scales) is presumably due the anatase-to rutile phase transformation that created extra porosity [21]. In

contrast, the undoped rutile specimen has a (relatively uniform) grain size of 0.46 ± 0.08 μm after the flash sintering. We note that we did not observe any significant difference in the agglomeration in the starting powders; thus, we attribute clustered (meatball-like) structures in Fig. 5.3 to the anatase-to-rutile phase transformation that created extra porosity. A similar sintered microstructure was observed for $Al_2O_3$ and attributed to a similar phase transformation mechanism in a prior study [21].

The grain sizes of the V-doped anatase and rutile specimens, respectively, are 1.10 ± 0.27 μm and 1.04 ± 0.29 μm, respectively. The grain size of N-doped anatase is 0.38 ± 0.05 μm, with a meatball-like microstructure. The N-doped rutile specimen has a substantially smaller grain size of 0.21 ± 0.05 μm after the flash sintering, which is related to the low relative density of ~ 87%.

### 5.4. Conclusions

In summary, we investigated the flash sintering of six $TiO_2$ based specimens with different doping (un-doped, V-doped vs. N-doped) and initial phases (anatase vs. rutile). In all six cases, the coupled thermal and electric runaway temperatures predicted from the measured specimen conductivities agree well with the observed onset flash temperatures within <5 °C, supporting a recently-developed quantitative model [3, 4]. The doping and initial phases also appreciably affect the densification and microstructural development during the flash sintering.

Chapter 5, in full, is a reprint of the material “Effects of Phase and Doping on Flash Sintering of $TiO_2$” as it appears in the Journal of Ceramic Society of Japan, Yuanyao Zhang, Jiuyuan Nie, Jian Luo, Journal of Ceramic Society of Japan, 2016, 124, 296-300. The dissertation author was the primary investigator and author of this paper. All experiments and data analysis were performed by the author except for the powder specimen preparation.

Table 5.1 Summary of key results of the flash sintering of $TiO_2$.

| Starting Phase | Doping | Observed Onset Flash Temperature ($T_{F,0}^{(exp)}$, °C) | Predicted Thermal Runway Temperature ($T_{F,0}^{(predicted)}$, °C) | Estimated Steady-State Specimen Temperature ($T_S^{(ss)}$, °C) | Final Relative Density (%) | Final Grain Size (mean ± STD, $\mu$m) |
|---|---|---|---|---|---|---|
| Anatase | undoped | 768 | 766 | 1039 | 95 | 1.11 ± 0.12 |
| | V-doped | 665 | 661 | 992 | 86 | 1.10 ± 0.27 |
| | N-doped | 818 | 815 | 1077 | 92 | 0.38 ± 0.05 |
| | | | | | | |
| Rutile | undoped | 831 | 827 | 1064 | 97 | 0.46 ± 0.08 |
| | V-doped | 672 | 670 | 1078 | 96 | 1.04 ± 0.29 |
| | N-doped | 774 | 773 | 1061 | 87 | 0.21 ± 0.05 |

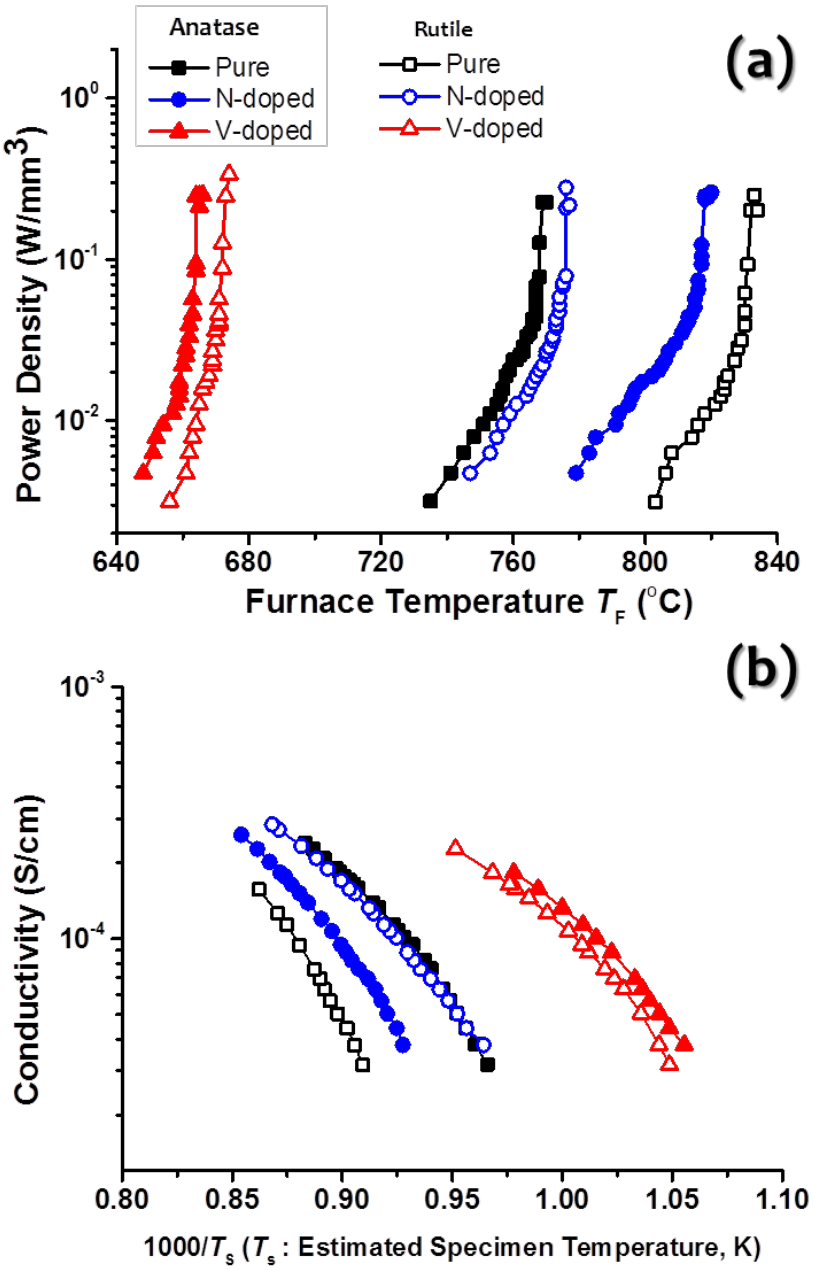


Figure 5.1 (a) Measured electric power dissipation vs. furnace temperature curves for the flash sintering of six different $TiO_2$ specimens. (b) Measured conductivity vs. the reciprocal of the estimated specimen temperature curves.

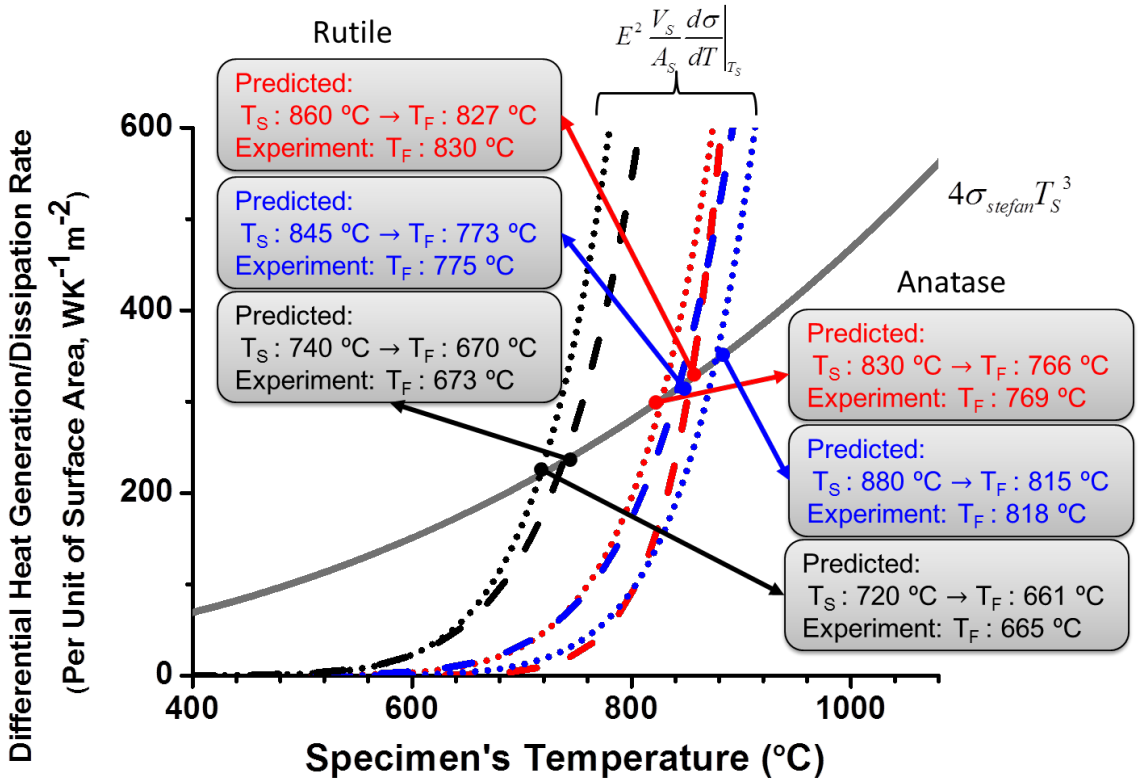


Figure 5.2 Computed differential heat generation rates vs. specimen temperature curves for the six $TiO_2$ specimens, along with the computed differential heat dissipation rate vs. specimen temperature curve (represented by the solid grey line). The anatase specimens are represented by dotted dashed lines, whereas the rutile specimens are represented by dashed lines. The intersections of the two types of curves represent the predicted coupled thermal and electric runaway conditions; see text, as well as the original article [4] that proposed this model, for elaboration.

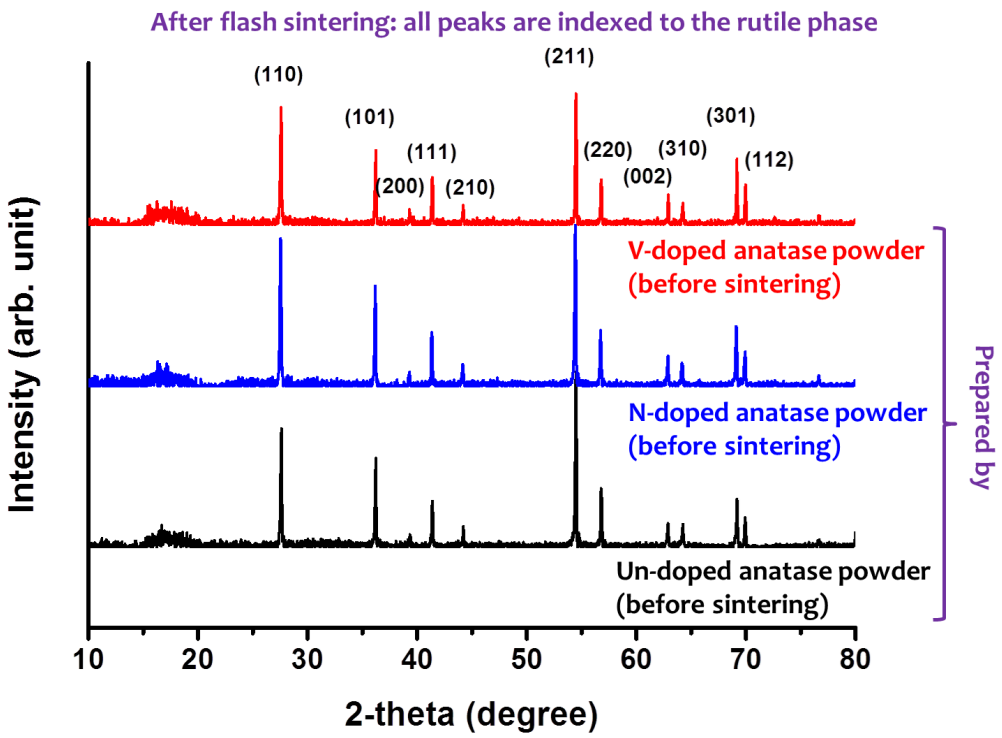


Figure 5.3 XRD patterns of three flash-sintered specimens prepared with un-doped, V-doped and N-doped anatase powders, showing that all specimens were converted to the rutile phase after the flash sintering. For brevity, these specimens are still referred to as un-doped, V-doped and N-doped anatase specimens in text (to differentiate them from the specimens prepared by un-doped, V-doped and N-doped rutile powders).

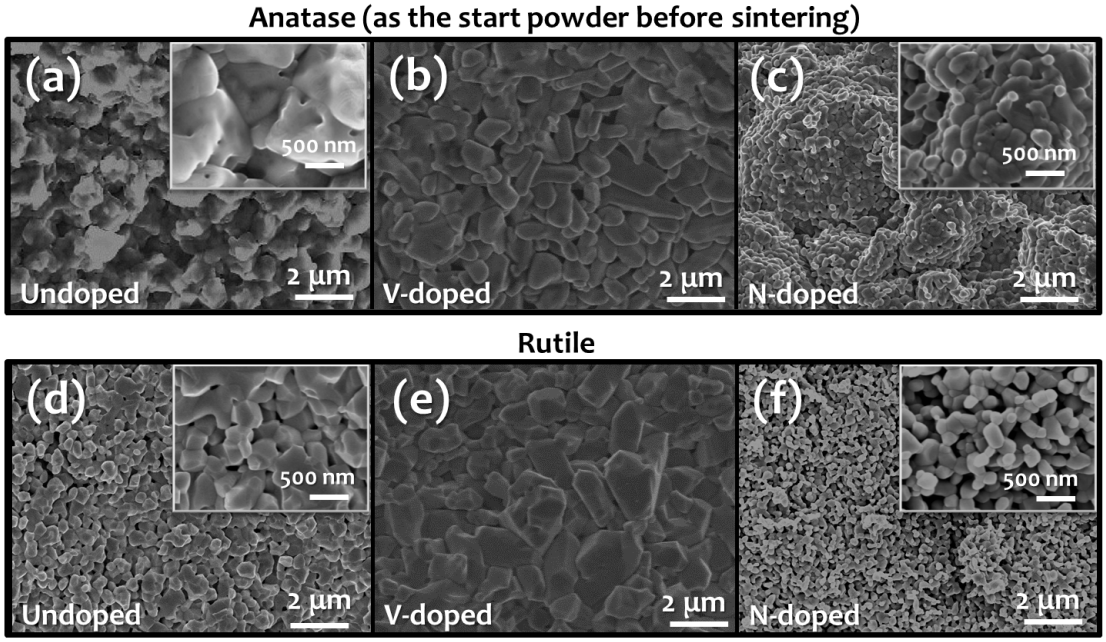


Figure 5.4 SEM images of representative microstructures of the fractured surfaces of the flash-sintered specimens that were prepared using (a) un-doped, (b) V-doped, and (c) N-doped anatase powders, as well as (d) un-doped, (e) V-doped, and (f) N-doped rutile powders. All specimens are rutile after the flash sintering.

**References:**

[1] M. Cologna, B. Rashkova, and R. Raj, J. Am. Ceram. Soc., 93 (2010) 3556-3559.

[2] R. Raj, M. Cologna, and J. S. C. Francis, J. Am. Ceram. Soc., 94 (2011) 1941-1965.

[3] Y. Zhang and J. Luo, Scr. Mater., 106 (2015) 26-29.

[4] Y. Zhang, J.-I. Jung, and J. Luo, Acta Mater., 94 (2015) 87-100.

[5] C. Schmerbauch, J. Gonzalez-Julian, R. Roeder, C. Ronning, and O. Guillon, J. Am. Ceram. Soc., 97 (2014) 1728-1735.

[6] J. S. C. Francis and R. Raj, J. Am. Ceram. Soc., 95 (2012) 138-146.

[7] S. K. Jha and R. Raj, J. Am. Ceram. Soc., 97 (2014) 527-534.

[8] H. Yoshida, Y. Sakka, T. Yamamoto, J.-M. Lebrun, and R. Raj, J. Eur. Ceram. Soc., 34 (2014) 991-1000.

[9] M. Cologna, A. L. G. Prette, and R. Raj, J. Am. Ceram. Soc., 94 (2011) 316-319.

[10] M. Cologna, J. S. C. Francis, and R. Raj, J. Eur. Ceram. Soc., 31 (2011) 2827-2837.

[11] R. Muccillo and E. N. S. Muccillo, J. Eur. Ceram. Soc., 34 (2014) 915-923.

[12] X. Hao, Y. Liu, Z. Wang, J. Qiao, and K. Sun, J. Power Sources, 210 (2012) 86-91.

[13] E. Zapata-Solvas, S. Bonilla, P. R. Wilshaw, and R. I. Todd, J. Eur. Ceram. Soc., 33 (2013) 2811-2816.

[14] R. I. Todd, E. Zapata-Solvas, R. S. Bonilla, T. Sneddon, and P. R. Wilshaw, J. Eur. Ceram. Soc., 35 (2015) 1865-1877.

[15] Y. Dong and I. W. Chen, J. Am. Ceram. Soc., 98 (2015) 2333-2335.

[16] Y. Dong and I. W. Chen, J. Am. Ceram. Soc. 98 (2015) 3624-3627.

[17] H. Qian and J. Luo, Acta Mater., 56 (2008) 4702-4714.

[18] H. J. Qian and J. Luo, Appl. Phys. Lett., 91 (2007) 061909.

[19] M. Samiee and J. Luo, J. Power Sources, 245 (2014) 594-598.

[20] R. Raj, J. Eur. Ceram. Soc., 32 (2012) 2293-2301.

[21] D. W. Kim, T. G. Kim, and K. S. Hong, J. Am. Ceram. Soc., 81 (1998) 1692-1694.

# Chapter 6. The densification mechanisms in flash sintering of ZnO

## 6.1. Introduction

Flash sintering, which was invented by Raj and his colleagues in 2010 [1], has caught great interests. It has several technological advantages, such as low furnace temperatures and high densification rates (short sintering duration), thereby being an energy-saving sintering technology. Moreover, flash sintering could be applied to numerous materials with broad range of applications, including fuel cells [2-4], sensors [5-6], structure ceramics [7-8], and solid electrolytes for applications in lithium or sodium batteries [9].

In a typical flash sintering experiment, an electrical field is applied to a specimen that is heated at constant ramp rate in a furnace; a flash occurs at a particular temperature with abrupt increase the specimen conductivity and temperature; subsequently, the electronic control switches to a constant current mode with a pre-set maximum current that sets the steady-state specimen temperature and densification completes in a few seconds.

While flash sintering has many technological advantages and potential applications, a systematic understanding of underlying mechanisms is crucial for the further development of this new sintering method and the selection of materials and processing recipes. Specifically, three key scientific questions should be answered. First, how does a flash start? Second, what are the mechanisms for rapid densifications? Third, what are the electric field/current effects on sintering and microstructural development?

Some prior independent studies from different groups [5, 6, 10-12] suggest the flash starts as a coupled electric and thermal runaway, at least for a range of materials systems investigated. We should point out that these models does not rule out that possibilities that in certain materials systems, a thermal runaway may occur as a consequence of an avalanche of non-equilibrium defects or first-order bulk phase or interfacial phase-like (complexion) transition that result in an abrupt increase in specimen conductivity, while in the majority of cases that have been examined [5, 6, 10-12], the thermal runaways are triggered by an exponentially increasing conductivity with increasing temperature.

Raj's analysis showed that estimated specimen temperature from Joule heating was not high enough to be responsible for the rapid density densification observed in $Y_2O_3$-stabilized $ZrO_2$ systems [13], thereby implying possible other effects avalanche of non-equilibrium Frenkel pairs. Majidi and van Benthem reported that the shrinkage of particle agglomerates under noncontacting electric filed, which could exclude effects of joule heating, was observed in an in-situ STEM [14].

This study focuses on the second question to use ZnO as a model system to probe probing the rapid densification mechanisms in flash sintering. In-situ shrinkage measurements of flash sintering were conducted in a modified dilatometer; the densification rates and grain growth are comparable with those obtained from rapid thermal annealing (RTA) experiments with similar heating profiles (without electric flied/current). Additional controlled flash sintering experiments, where will limit either the maximum current or effective ramping

rates electronically to probe the sintering mechanisms, suggest that both Joule heating and ultra-fast heating rate play critical roles for the rapid densifications in flash sintering.

## 6.2. Experimental

### 6.2.1. Green pellet

The procedure of making green specimen have been described in chapter 4, [15], and is just briefly summarized it here. High-purity ZnO powders (>99.99%, purchased from Sigma Aldrich) with 0.5 wt. % of a binder were grounded and uniaxially pressed at ~300 MPa to make pellets with dimensions of *D* (diameter) = 6.4 mm and *H* (height) ≈ 1 mm or 3 mm for RTA or flash sintering, respectively. After burning out the binder, platinum was sputtered on both sides of the green specimens and surrounding areas were slightly grounded by SiC paper.

### 6.2.2. Sintering

#### 6.2.2.1. Conventional flash sintering

The electroded specimens were placed in a dilatometer (DIL 402 PC, Netzsch, Boston, MA, USA) and were attached to two flatted Pt foils on both sides to apply electric field. The high-purity alumina push rod with a minor pressure of ~9.55 KPa was (to ensure a good contact with the specimen) to measure the shrinkage of the specimen with the resolution of ~8 nm. Conventional flash sintering was conducted on one set of specimens, where a

voltage of 300 V/cm was applied initially, until a flash event occurs and the current reaches a preset maximum value ($I_{max}$ = 0.5, 0.75 or 1 A; corresponding to estimated maximum current densities: $J_{max} \approx$ 20, 30, or 39 mA/mm$^2$, respectively); after that point, the power source switched from voltage to current control mode. The electric power source and furnace were shut down with a pre-set duration after the current reaches the $I_{max}$ and the specimens were cooled down within the furnace.

#### 6.2.2.2. Controlled Flash Sintering

In a flash sintering experiment with a controlled effective ramping rate, an electroded specimen was placed in a dilatometer with the same experimental configuration and an initially constant electric field of 300 V/cm. However, in this experiment, maximum current limit was initially set to be 0.05 A; after the flash, the current limit was held for 100 sec and then increased by 0.1 A per step; the process was repeated for seven steps until reaching 0.75 A. Then, the electric power source and furnace were shut down and the specimen was cooled down within the furnace.

#### 6.2.2.3. Conventional Sintering

One specimen without electrode was sintered in dilatometer up to 1200 °C with a heating rate of 5 °C/min.

#### 6.2.2.4. Rapid Thermal Annealing

Specimens without electrode were placed on a Pt foil in the rapid thermal annealing equipment (AG Associates Heat Pulse 610). The heating ramp rate was set 200 °C per second; the specimens were then held (sintered) isothermally at 1000 °C and 1100 °C, respectively, for 0, 5, 10, 15, 20, 25, and 30 sec, respectively.

### 6.2.3. Characterization

Final bulk densities were measured by the standard Archimedes method if density is greater than 90%; otherwise, the density was calculated by weight and volume. The microstructure was determined by the field emission environmental scanning electron microscope (SEM, Philips XL30). Grain sizes were measured at the fracture surfaces using a standard intercept method from the SEM micrographs. Electric conductivity after flash sintering was measured by digital multimeter (Tektronix DMM 4050, Beaverton, OR, USA) with a heating rate of 10 °C/min up to 1200 °C in the same configuration in dilatometer.

## 6.3. Results

### 6.3.1. Conventional flash sintering results

Fig. 6.1 shows the relationship between power density and furnace temperature, where three specimens were flash sintered with current limits of 0.5, 0.75, and 1 A, respectively. The onset flash sintering temperature was around 570 °C (where the minor differences among them were due to specimen-to-specimen variations). The measured linear shrinkage vs. furnace temperature

curves were shown in the Fig. 6.2, where results from three flash sintering experiments with current limits of 0.5, 0.75, and 1 A, respectively, as well as a conventional sintering experiment without applied electric filed, are shown. The linear shrinkages after flash sintering were 11.8%, 14.8%, and 17.6%, respectively, for the specimens with current limits of 0.5, 0.75, and 1 A, respectively. In comparison, the density was measured to be 17.4% for conventional sintered specimen, quenched from a much higher furnace temperature of 1200 °C. Relative densities of all green specimens were ~60% (± 1%). After flash sintering, the relative densities reached 88.5%, 94.4%, and 97.2%, respectively, when the current limits were set to 0.5, 0.75, 1 A, respectively (Table 6.1).

Using a flash-sintered specimen at the current limit of 0.75 A as an example, Fig. 6.3 illustrates representative voltage, current, power density, estimated specimen temperature (from the power density and black body radiation model [14]), specimen conductivity (calculated from the measured voltage and current), linear shrinkage, for the time duration of 40 sec, from 10 sec before the flash to 30 sec after the flash. After the occurrence of the flash, a sudden increase in current (to the pre-set $I_{max}$) and drop in voltage took place within ~ 1 sec, accompanying with an increase in the power density (Joule heating) and estimated specimen temperature. At the same time, the specimen conductivity increased, largely due to the Joule heating and Arrhenius dependent specimen conductivity. Most shrinkage occurred within ~20 sec after the occurrence of the flash. After the flash, current was kept at a constant level of

pre-set $I_{max}$ because the power supply was in current-control mode; how the voltage dropped gradually (in the steady-state or Stage III of the Raj's terminology [16]), especially in the first 20 sec because of the densification of the specimen (see Fig. 6.3f). Noting that the estimated specimen temperature ($T_S$) was calculated from the black body radiation model [14] using the volume and surface area calculated/estimated from measured linear shrinkages. The maximum point in the estimated temperature in Fig. 6.3(e) is likely an artifact because we assumed an instantaneous heat generation and dissipation balance, while in reality, there will be a delay in achieving the stead state so that the actual heating rate should be slower that that shown in Fig. 6.3(d).

Fig. 6.4 shows SEM cross-sectional images of specimens after flash sintering. (a) – (f) represent specimens, quenched after 5, 20, and 30 sec of imitation of flash, respectively, where the current limits were set to be 0.5 A and 0.75 A, respectively. Grain size are 0.14 (mean) ± 0.04 (one standard deviation) μm, 0.19 ± 0.06 μm and 0.31 ± 0.10 μm for the flash sintered specimen with current limit of 0.5 A with holding time of 5, 20 and 30 sec after current reached maximum, respectively. Within increasing current limit to 0.75 A, grain size are increased to 0.26 ± 0.08 μm, 0.40 ± 0.15 μm and 1.03 ± 0.34 after 5, 20, and 30 sec when current reached maximum, respectively. Grain size increases dramatically with increasing holding time, especially on the specimens of current limit at 0.75 A with holding time of 20 and 30 sec; relative density only changes ~2% but grain size is ~ 2.5X larger. Comparison of grain size in fig. 6.4 (c), (f)

and (h), they represent specimens after flash sintering with different current limit but same holding time. Grain sizes are 0.31 ± 0.10 μm, 1.03 ± 0.34 μm and 1.92 ± 0.55 μm for the specimen at current limit of 0.5, 0.75 and 1A, respectively. The main reason is that estimated specimen temperatures in these specimens are 1050 °C, 1160 °C and 1390 °C for current limit of 0.5, 0.75 and 1A, respectively (Table 6.1). Fig. 6.4 (g) shows microstructure of specimen after controlled flash sintering (please refer to Fig. 6.5 and next section for the specific scheme) and grain size is 0.40 ± 0.10 μm.

### 6.3.2. Controlled flash sintering

Comparison between conventional flash sintering (black, square symbol) and controlled flash sintering (red, round symbol) was shown in fig. 6.5. It illustrates current, power density, linear shrinkage, electric filed, and estimated specimen temperature in fig. 6.5 (a) – (e), respectively, from 10 sec before the flash to 30 sec or 730 sec after the flash in conventional flash sintering and controlled flash sintering, respectively. The steps in fig. 6.5 (a) represent holding time in each step for controlled flash sintering since it was in current control mode. The electric filed (calculated by voltage and actual specimen thickness measured by dilatometer in situ) continuously decreases with current increasing. The final electric filed in controlled flash sintering specimen is lower than conventional flash sintering, and it leads the power density smaller [fig. 6.5 (b)], thus estimated specimen temperature is lower [fig. 6.5 (e)]. The possible reason could be conductivity increased during sintering process because of specimen

densification, so the electric field (voltage) is lower in controlled flash sintering than conventional flash sintering. The final linear shrinkage and relative density in controlled flash sintering are also smaller than conventional flash sintering, at 13.0% vs. 17.6% of linear shrinkage and 86.7% vs. 94.4% of relative density for controlled flash sintering and conventional flash sintering, respectively (Table 6.1).

### 6.3.3. Rapid thermal annealing

Relative density and grain size of specimen after rapid thermal annealing (RTA) at temperature of 1000 °C and 1100 °C were summarized in Table 6.2. The relative density reached more than 90% in the first 10 sec at annealing temperature of 1100 °C, and then the relative density increased slowly from 10 sec to 30 sec. Nonetheless, grain size didn't change much in the first 10 sec, but it increased rapidly from 10 sec to 30 sec at sintering temperature of 1100 °C. This is a normal phenomenon in sintering, grain growth occurs severely when relative density reaches >90% [17]. Both of relative density and grain size increased continuously at annealing temperature of 1000 °C, but relative density is still lower than 90% after isothermal sintering of 30 sec. Fracture surface of the specimen annealed at 1000 °C and 1100 °C was shown in the Fig. 6.6 (a) – (g) and Fig. 6.6 (a*) – (g*), respectively, for isothermal sintering time from 0 to 30 sec, respectively. The results of grain size and relative density after RTA were summarized in Table 6.2.

## 6.4. Discussion

### 6.4.1. The onset flash sintering temperature

Previous reports from several different groups [5, 6, 10 – 12] suggested that the onset flash sintering is resulted from a coupled electric and thermal runaway. In one model discussed in prior chapters [5, 6], the rise of specimen temperature is determined by the energy conservation law. The specific flash conditions for stable and unstable temperature rises are discussed briefly as follows. First, the necessary and sufficient conditions for a stable temperature rise are:

$$\sigma(T_S)E^2V_S = \dot{Q}(T_S, T_F) \tag{6.1}$$

and

$$E^2V_S \left.\frac{d\sigma}{dT}\right|_{T_S} \le \frac{\partial \dot{Q}(T_S, T_F)}{\partial T_S}, \tag{6.2}$$

where $E$ is the electrical field, $V_S$ is the volume of the specimen, $T_S$ and $T_F$ are the specimen (S) and furnace (F) temperatures, respectively, and $\sigma(T_S)$ is the specimen conductivity. In Eq. (6.1), the left side, $\sigma(T_S)E^2V_S$, is the rate of heat generation from joule heating, whereas the right side, $\dot{Q}(T_S, T_F)$, represents the rate of heat dissipation from the specimen. Eq. (6.2) represents the condition for a stable temperature rise, whereas an unstable temperature rise will occur if

$$E^2V_S \left.\frac{d\sigma}{dT}\right|_{T_S} > \frac{\partial \dot{Q}(T_S, T_F)}{\partial T_S}. \tag{6.3}$$

Eq. (6.3) suggests a graphical construction method to find the thermal runaway (= flash) conditions, as schematically illustrated in Fig. 6.7. For a case where black body radiation is the dominant heat dissipation mechanism, a simple analytic form can be obtained:

$$\frac{\partial \dot{Q}(T_S, T_F)}{\partial T_S} \equiv \alpha = 4\sigma_{Stefan} T_S^3 A_S \tag{6.4}$$

where $A_S$ is the surface area of the specimen, and $\sigma_{Stefan}$ = 5.67 $\times$ $10^{-8}$ W/m$^2$K$^4$. More explanation and details have been described in earlier reports [5 – 6]. Using specimen of current limit at 0.75 A as an example, we plotted the conductivity vs. specimen temperature in the fig. 6.7 (a) and applied the thermal runaway model mentioned above in our new experiment results. The computed differential heat generation rates per unit area ( $E^2 \frac{V_S}{A_S} \frac{d\sigma}{dT}\Big|_{T_S}$ ) and differential heat dissipation rate per unit area ( $4\sigma_{stefan} T_S^3$ ) vs. specimen temperature ($T_S$) curves were shown in fig. 6.7 (b). There is only five degrees difference between model prediction and experiment results, and the reason of excellent agreement has been discussed in prior report [5-6] and chapters.

### 6.4.2. Relationship between current limits and densification

In conventional flash sintering experiment (section 6.3.1), specimen with a higher current limit would have larger linear shrinkage and higher relative density in a same initial applied electric field and same holding time after imitation of

flash. Current limit determines how much additional energy from power source applied on the specimen via Joule heating, which also determines the ΔT (temperature difference between specimen temperature and furnace temperature). The onset flash sintering temperatures are the same because of same electric filed applied initially (minor difference because of specimen-to-specimen variation), thus specimen temperature in steady state after flash depends on the current limit (Table 6.1). In general, higher current limit leads higher specimen temperature and more densification, so it implies that the Joule heating is at least one important factor.

### 6.4.3. Relationship between heating rate and densification

Comparison between controlled flash sintering and conventional flash sintering, the linear shrinkage and relative density after sintering in controlled flash sintering are lower (Table 6.1 and Fig. 6.6), though the total energy per unit volume from Joule heating in controlled flash sintering (131.2 W/mm$^3$) is larger than conventional flash sintering (20.0 W/mm$^3$). One major difference between controlled flash sintering and conventional flash sintering is limitation of heating rate, where ΔT is determined by current limit, thus heating rate ($dT/dt$) in controlled flash sintering is lower than conventional flash sintering. We suggest that a high heating rate ($dT/dt$) is a critical factor that leads to fast densification. Our hypothesis is that a high heating rate ($dT/dt$) can help to achieve fast densification for the following reasons.

Firstly, high heating rate prevents initial coarsening to keep a high densification driving force. Densification rate strongly depends on the grain size [18], and it could be expressed as $p \propto \frac{1}{d^n}$, where *p* is densification rate, d is grain size and n depends on whether the densification rate is controlled by lattice diffusion (n=3) or by grain boundary diffusion (n=4). From this equation, if grain size doubled, the densification rate would reduce 8 times (lattice diffusion) or 16 times (grain boundary diffusion). From our experimental results, grain size reached 0.40 ± 0.10 μm with relative density of 86.7% in controlled flash sintering, whereas, 0.26 ± 0.08 μm with relative density of 78.3%, 0.40 ± 0.15 μm with relative density of 93.5% and 1.03 ± 0.34 μm with relative density of 94.4% in conventional flash sintering at current limit of 0.75 A after 5, 20 and 30 sec of imitation of flash, respectively. Density increased ~15% when grain size is increased from 0.26 μm to 0.4 μm, however, density only changed < 1% when grain size reached > 0.4 μm (we also aware that densification rate is related to relative density, but grain size is more important with an exponential of -3 or -4). In controlled flash sintering, the enlarged grain size (~ 0.4 μm) could decrease densification rate, thus relative density is also smaller. Secondly, it is possible that high heating rate (d*T*/d*t*) produces non-equilibrium defects, with possible influences of the field/current.

### 6.4.4. Comparison of flash sintering and rapid thermal annealing

First of all, we assume that the shrinkage is isotropic during densification with 12.5 – 16.5% in radius direction measured from caliper after cooling down to room temperature and 14.8% in thickness direction measured from dilatometer in situ for the specimen of current limit at 0.75 A; 13.8 – 14.9% in radius direction and 11.8% in thickness direction for the specimen of current limit at 0.5 A. The variation of shrinkage in radius direction is results from ununiformed grounded surround area before sintering (to remove the Pt sputtered on surround area), measurement error, and slightly deformed (totally less than 0.2 mm). We convert linear shrinkage to relative density to calculate time-dependent density ($\rho$) by the equation of $\rho = \left( \frac{L_f}{L(t)} \right)^3 \cdot \rho_f$ [18], where $L_f$ is the final length of the specimen, $L(t)$ is the time-dependent length measured from dilatometer, and $\rho_f$ is the final density. Fig. 6.8 (a) shows comparison of four relative density vs. sintering time curves between two flash sintering experiments with the current limits of 0.75 A and 0.5 A, respectively, and two rapid thermal annealing experiments at 1100 °C and 1000 °C, respectively. The time-dependent density of flash sintering specimen is calculated by the equation mentioned above from time-dependent shrinkage measured by dilatometer. The time-dependent density of rapid thermal annealed specimens is measured from fourteen different specimens.

The time-dependent density curves in these two different sintering methods are similar. Although the estimated specimen temperature in flash sintering is slightly higher than rapid thermal annealing (1160 °C in $I_{max}$ = 0.75 A vs. 1100 °C in RTA, and 1050 °C in $I_{max}$ = 0.5 A vs. 1000 °C in RTA), the

densification rate in RTA at 1100 °C is the highest, flash sintering of current limit at 0.75 A and 0.5 A are the second and third, and RTA at 1000 °C is the lowest. In RTA at 1100 °C, relative density reached more than 90% in 10 sec comparing with 15 sec in flash sintering with current limit of 0.75 A. There are some points we want to discuss below:

Firstly, specimen temperature in flash sintering could be over estimated since we only included radiation in specimen temperature estimation and ignored thermal conduction or others. If we estimated specimen temperature from electric conductivity after flash sintering (assume that electric conductivity follows Arrhenius relation (fig. 6.9) and ignore microstructure evolution during re-annealing), the estimated specimen temperature for the specimens at current limit of 0.5 A and 0.75 A are 920 °C and 1040 °C. We used the measured conductivity in steady state during flash sintering to calculate specimen temperature based on the fitting results of conductivity after flash sintering (fig. 6.9). There is about 120 - 130 °C difference between specimen temperature estimated from black body radiation model and electric conductivity. The temperature estimation from electric conductivity might be underestimated because of microstructure evolution, which makes the measured electric conductivity during re-annealing is higher than conductivity in steady state in flash sintering as space layer might be formed at grain boundary during the specimen cooling after flash sintering. ZnO is a very promising material for varistor and electrons accumulated at grain boundaries and formed a space charge layer, which makes the conductivity increased, if we don’t control the

cooling rate [19]. In industry application, the cooling rate for ZnO based varistor is usually at 150 °C/hour, however, the cooling rate of specimen after flash sintering is much higher from > 1000 °C to ~600 °C (furnace temperature) in seconds when we turn off the power source. So the conductivity after flash sintering might be overestimated, so specimen temperature could be underestimated. In general, the estimated specimen temperature for specimen with current limit of 0.75 A and 0.5 A are ranged from 1040 °C to 1160 °C and 920 °C to 1050 °C, respectively. However, we cannot know the exact specimen temperature in flash sintering; all the estimation should have errors, and we want to know the effects of electric filed in densification, so these temperature estimation errors is in tolerance.

Secondly, from the grain size comparison, it supported our hypothesis that temperature comparison between flash sintering at current limit of 0.75 A and RTA at 1100 °C is fair, as well as, flash sintering at current limit of 0.5 A and RTA at 1000 °C. Fig. 6.8 (b) shows the comparison of grain size vs. sintering time between flash sintering at current limit of 0.75 A and 0.5 A and rapid thermal annealing at 1100 °C and 1000 °C. In flash sintering experiment, the electric power was cut off after 5, 20 and 30 sec when current reached maximum and specimens were cooled down in furnace. In RTA experiment, specimens were cooled down in the equipment from pre-set sintering temperature to room temperature in less than 2 minute. Grain size of specimen after flash sintering at current limit of 0.75 A is almost the same as specimen after RTA at 1100 °C; grain size between specimen after flash sintering at current limit of 0.5 A and RTA at 1000 °C are also similar in all time scales. Minor grain size difference

also supports that specimen temperature is similar (FS $I_{max}$ = 0.75 A vs. RTA 1100 °C and FS $I_{max}$ = 0.75 A vs. RTA 1000 °C); otherwise, grain size would have obvious difference, such as ~ 3 times difference between flash sintering of current limit at 0.75 A and 0.5 A with estimated temperature difference of 110 °C, ~ 3 times difference in RTA with sintering temperature difference of 100 °C.

Comparing densification rate in flash sintering of current limit at 0.75 A and 0.5 A, they are almost the same in the first 15 seconds. The density of specimen in current limit of 0.75 A continuously increases after 15 sec, however, it doesn't change much in specimen of current limit of 0.5 A. Although the estimated temperature in current limit of 0.75 A is higher than 0.5 A, the densification rate is almost the same in the first 15 sec. The possible reason is that small grain size at beginning leads high densification rate. The densification rate become slower after 15 sec because of enlarged grain size, and then temperature becomes the dominate effect since estimated specimen temperature in current limit of 0.75 A is 100 degree higher than current limit of 0.5A.

From our results, relative density could reach more than 95% when the specimen temperature reaches 1100 °C, no matter how the specimen temperature reached (conventional sintering, flash sintering and RTA). However, if the specimen temperature is ~1000 °C, the relative densities in these three sintering methods (flash sintering, conventional sintering, and RTA) are all lower than 90%. Specimen temperature is the main effect in densification, higher temperature and higher densification no matter with or without electric field. We cannot make a conclusion that electric field has no effect in flash sintering, and it

is not a main reason in densification at least in ZnO system. Unlike YSZ or other ion conductor, where electric field affect ion movement [20] and it might accelerate densification, ZnO is a semiconductor, where electron moves under electric field and it has little effect on densification. Lots of interesting phenomena was observed under electric field in earlier reports, such as phase transformation [21], but it is hard to connect these specific phenomena with densification mechanism. Anomalous elastic volume expansions of ~3% in flash sintering of 8YSZ was reported within an in situ X-ray diffraction measurement [22], and it is an evidence that electric field make contributions in densification.

### 6.5. Conclusions

In this report, we discussed the mechanisms of densification in flash sintering by comparing densification rate in different current limits, heating rate and mimicking flash sintering temperature profile in rapid thermal annealing that excludes the electric field effect. Specimen temperature or the additional heat from joule heating, and rapid heating profile are the main effects of densification, though we do aware that electric field could make contributions in densification, they are not main effects at least in ZnO system.

Chapter 6, in full, is currently in preparation for submission for publication “Probing the densification mechanisms during flash sintering of ZnO” Yuanyao Zhang, Jiuyuan Nie, Jonathan Michael Chanm, Jian Luo. The dissertation author was the primary investigator and author of this paper. All experiments and data

analysis were performed by the author except for the powder specimen preparation.

Table 6.1 Summary of the key experimental results of the flash sintering of ZnO in different current limit. Grain size was measured in the middle part of specimens' cross-section. Estimated specimen temperature was calculated by blackbody radiation model.

| Flash Sintering Condition ($E$ = 300 V/cm) | Before Sintering | After Sintering | | | | |
|---|---|---|---|---|---|---|
| | Relative Density | Shrinkage | Density ($g/cm^3$) | Relative Density | Grain Size (μm) | Estimated Temperature (°C) |
| $I_{max}$ = 0.5 A, 30 sec | 58.3% | 11.8% | 5.12 | 88.5% | 0.31 ± 0.10 | 1050 |
| $I_{max}$ = 0.75 A, 30 sec | 61.2% | 14.8% | 5.30 | 94.4% | 1.03 ± 0.34 | 1160 |
| $I_{max}$ = 1 A, 30 sec | 58.1% | 17.6% | 5.45 | 97.2% | 1.92 ± 0.55 | 1390 |
| $I_{max}$ = 0.5 A, 5 sec | 58.9% | 3.5% | 3.56 | 63.5% | 0.14 ± 0.04 | - |
| $I_{max}$ = 0.5 A, 20 sec | 59.6% | 9.3% | 4.30 | 76.6% | 0.19 ± 0.06 | - |
| $I_{max}$ = 0.75 A, 5 sec | 58.3% | 9.7% | 4.39 | 78.3% | 0.26 ± 0.08 | - |
| $I_{max}$ = 0.75 A, 20 sec | 59.5% | 15.9% | 5.25 | 93.5% | 0.40 ± 0.15 | - |
| 0.05 A – 0.75 A rate of 0.1 A per 100 sec (Controlled Flash sintering) | 58.6% | 13.0% | 4.86 | 86.7% | 0.40 ± 0.10 | - |

Table 6.2 Summary of the key experimental results of the rapid thermal annealing of ZnO. Relative density less than 90% was measured from weight and volume, above 90% was measured from Archimedes method.

| Annealing Temperature | | Annealing Time (sec) | | | | | | |
|---|---|---|---|---|---|---|---|---|
| | | 0 | 5 | 10 | 15 | 20 | 25 | 30 |
| 1000 °C | Density | 63.70% | 59.80% | 70.06% | 75.74% | 83.00% | 84.16% | 87.21% |
| | Grain Size (nm) | 126 ± 48 | 102 ± 40 | 166 ± 49 | 148 ± 55 | 226 ± 67 | 293 ± 86 | 453 ± 130 |
| 1100 °C | Density | 65.60% | 75.80% | 92.60% | 93.20% | 94.00% | 95.50% | 95.00% |
| | Grain Size (nm) | 220 ± 80 | 175 ±44 | 523 ± 142 | 338 ± 140 | 666 ± 220 | 941 ± 326 | 980 ± 254 |

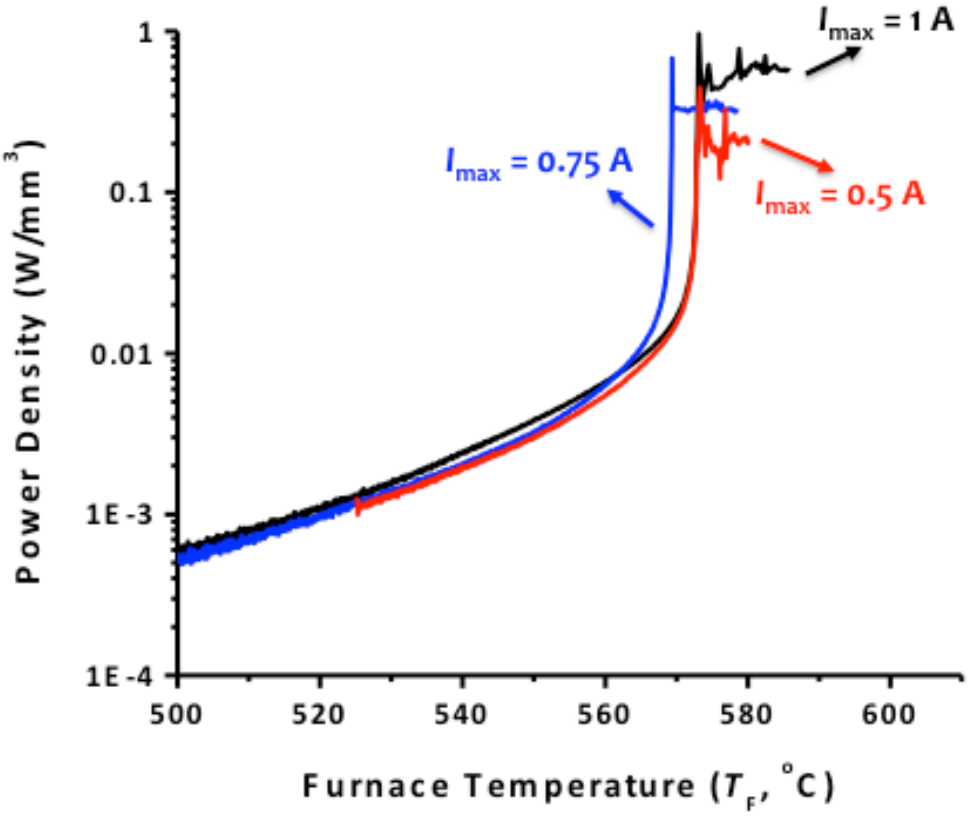


Figure 6.1 Measured electric power dissipation vs. furnace temperature curves for flash sintering of ZnO, where the current limits were set to be 0.5 A, 0.75 A, and 1 A, respectively.

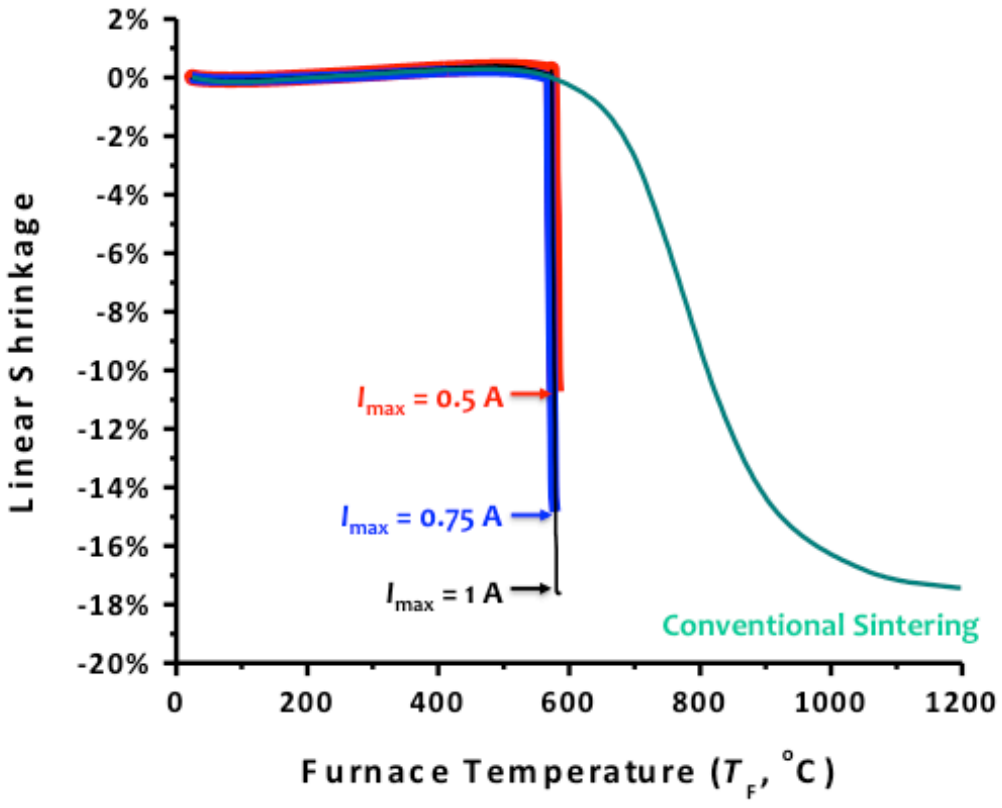


Figure 6.2 Measured linear shrinkage vs. furnace temperature curves for flash sintering as well as conventional sintering.

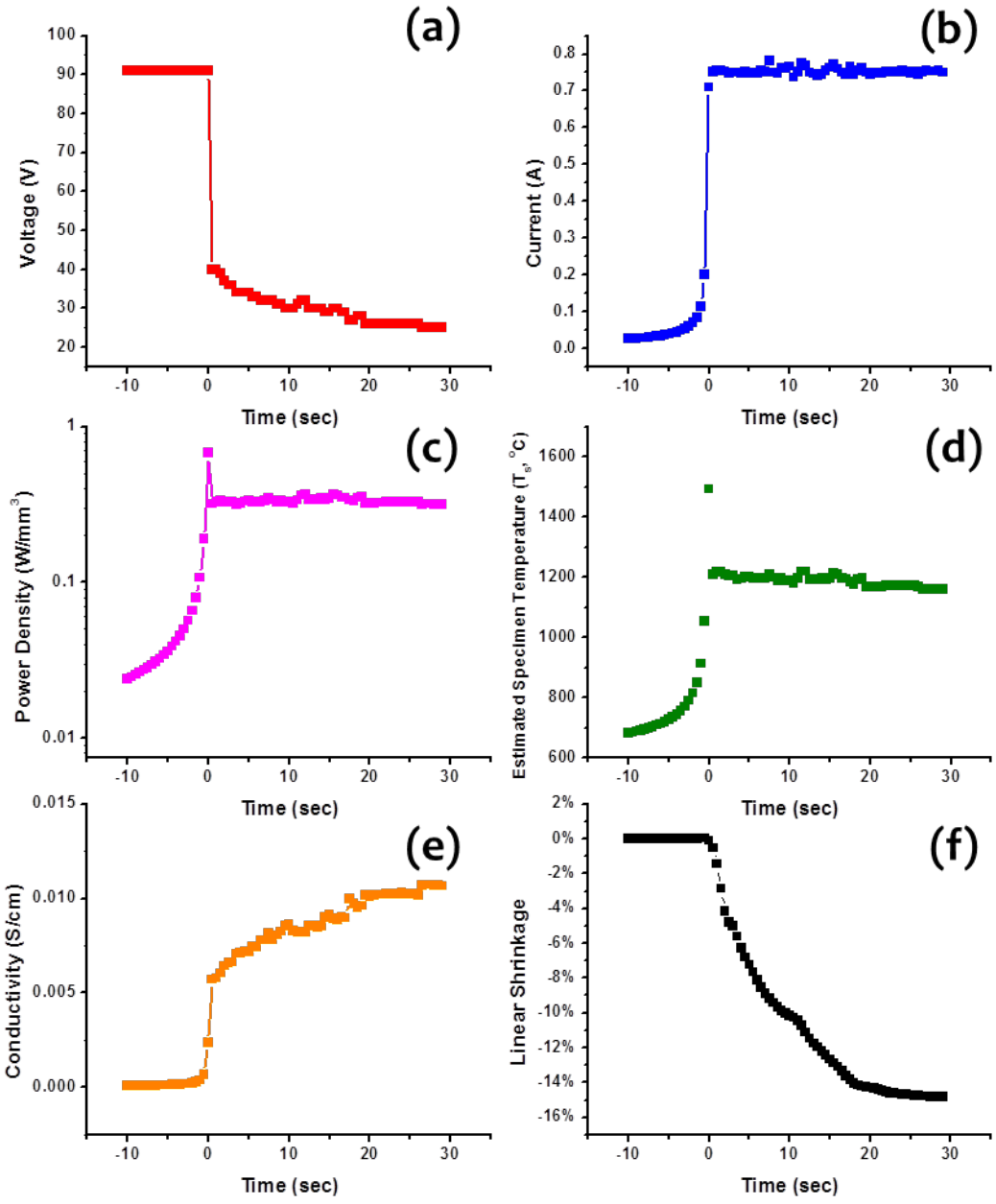


Figure 6.3 An example of a representative flash sintering processing ($I_{max}$ = 0.75 A), showing the (a) voltage, (b) current, (c) power density, (d) estimated specimen temperature, (e) specimen conductivity and (f) linear shrinkage vs. time curves for an approximated duration of 40 sec (from 10 sec before to 30 sec after the occurrence from of the flash).

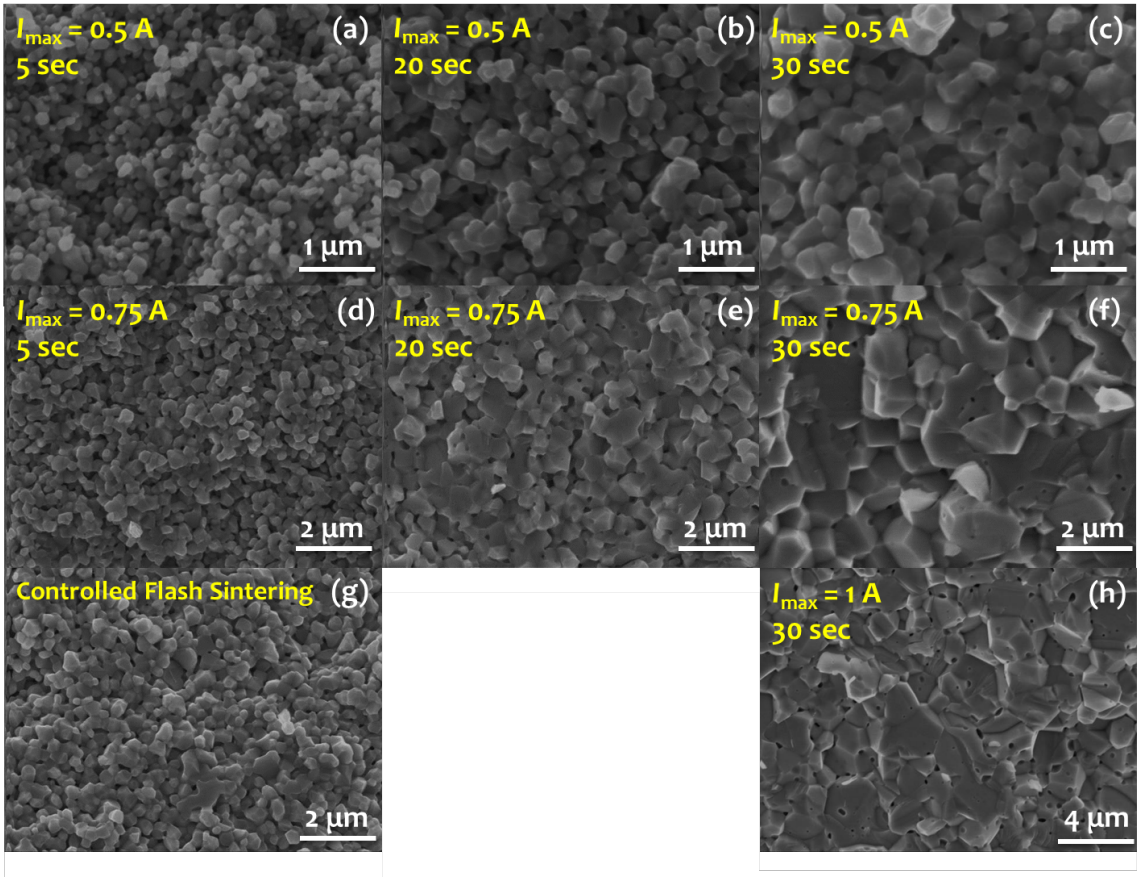


Figure 6.4 Representative cross-sectional SEM images. (a) – (f) Flash sintered ZnO specimens, quenched after 5, 20, and 30 sec, respectively, after the imitation of flash, where the current limits were set to be 0.5 A and 0.75 A, respectively. (g) “Controlled” flash sintering (please refer to Fig. 6 and related text for the specific scheme). (h) A flash sintered ZnO specimen after 30 sec, where the current limit was set to be 1 A.

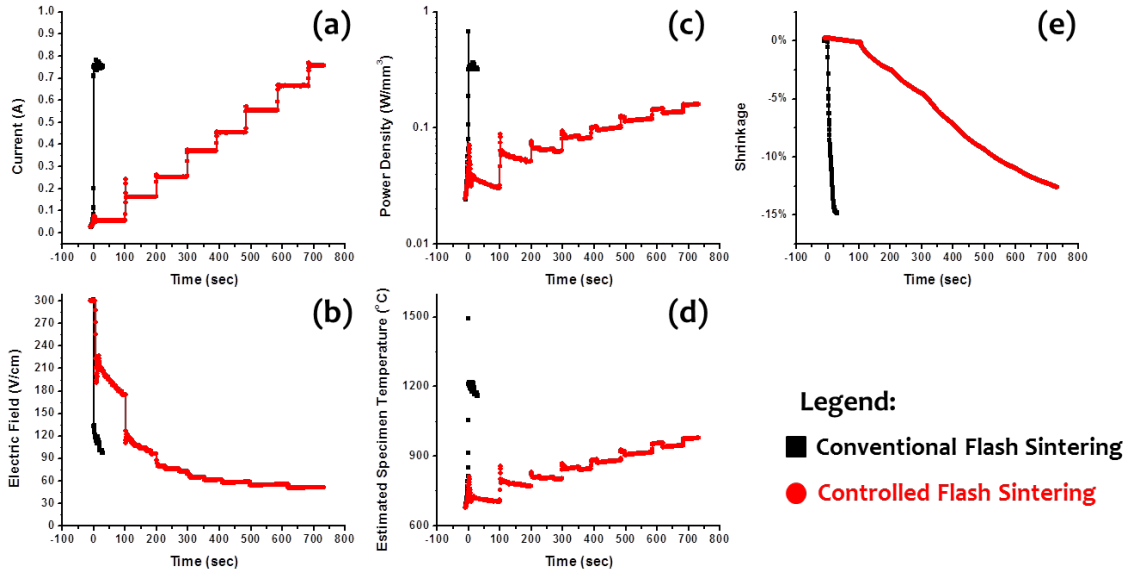


Figure 6.5 Comparison of a “normal” flash sintering (black, square symbols) and a “controlled” flash sintering (red, round symbols): the measured (a) current, (d) electric filed, (c) power density, (d) estimated specimen temperature, and (e) linear shrinkage, respectively, vs. the time curves.

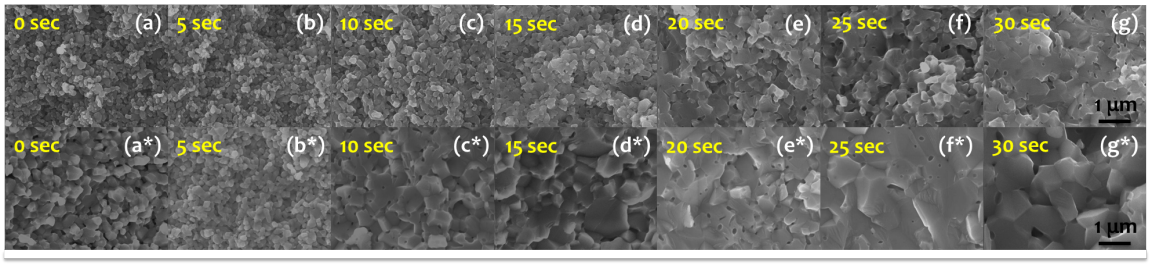


Figure 6.6 Cross-sectional SEM images of rapid thermal annealed ZnO specimens. At 1000 °C for (a) 0, (b) 5, (c) 10, (d) 15, (e) 20, (f) 25, and (g) 30 sec, respectively, and at 1000 °C for ($a^*$) 0, ($b^*$) 5, ($c^*$) 10, ($d^*$) 15, ($e^*$) 20, ($f^*$) 25, and ($g^*$) 30 sec, respectively. All the scale bars are 1 μm.

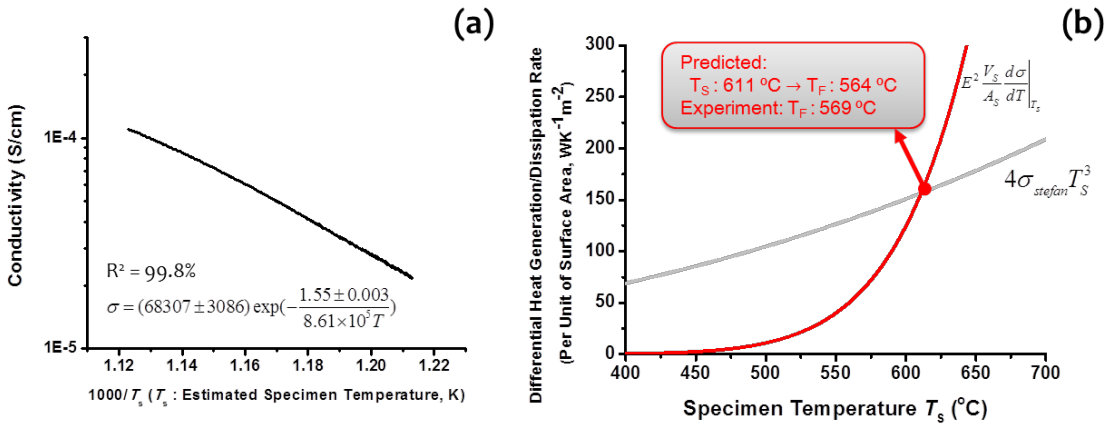


Figure 6.7 (a) Measured conductivity vs. the reciprocal of the estimated specimen temperature curve (before the flash). (b) Computed differential heat generation and dissipation rates per unit area vs. specimen temperature curves. The thermal runaway (flash) condition is determined by the intersection of the heat generation and dissipation rates curves.

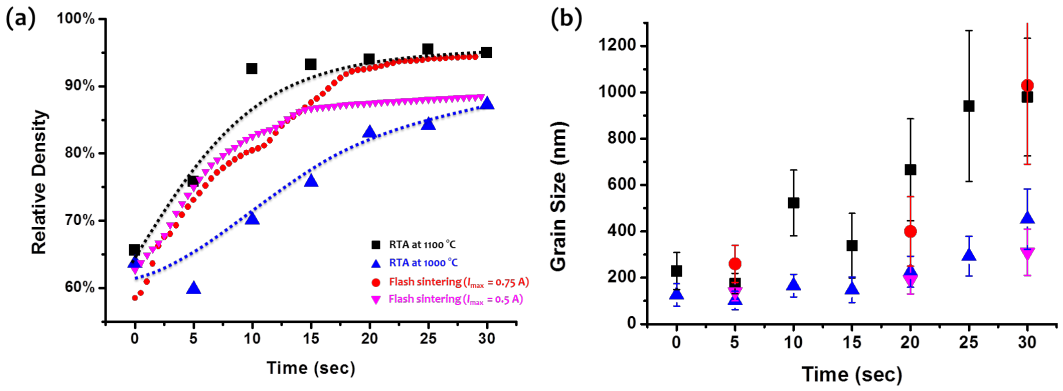


Figure 6.8 Comparison of four relative density (a) and grain size (b) vs. sintering time curves. Two flash sintering experiments with the current limits of 0.75 A and 0.5 A, respectively, and two rapid thermal annealing experiments at 1100 °C and 1000 °C, respectively.

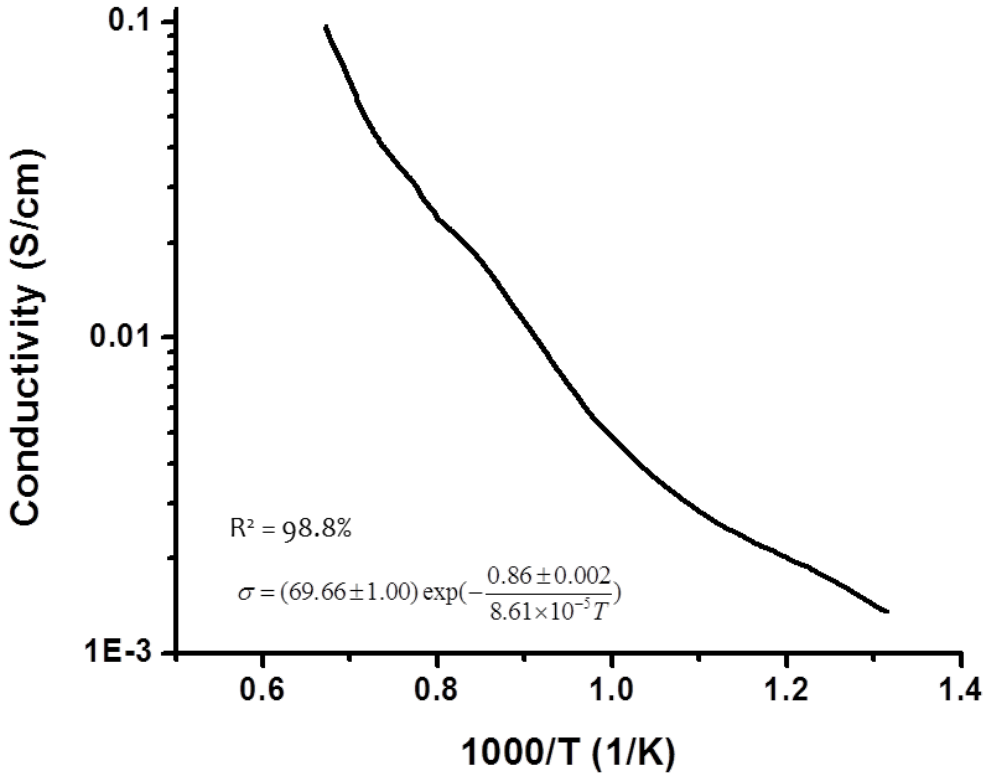


Figure 6.9 Measured conductivity of specimen after flash sintering vs. reciprocal specimen temperature.

**References:**

[1] M. Cologna, B. Rashkova, R. Raj, J. Am. Ceram. Soc. 93 (2010) 3556-3559

[2] M. Cologna, A. L. G. Prette, R. Raj, J. Am. Ceram. Soc. 94 (2011) 316-319,

[3] A. Gaur, V. M. Sglavo. J. Mater. Sci. 49 (2014) 6321-6332

[4] X. Hao, Y. Liu, Z. Wang, J. Qiao, K. Sun, J. Power Sources 210 (2012) 86-91

[5] Y. Zhang, J. Jung and J. Luo, Acta Mater., 94(2015) 87-100

[6] Y. Zhang, J. Nie, and J. Luo, J. Ceram. Soc. of Japan, 124 (2016) 296-300

[7] E. Zapata-Solvas, S. Bonilla, P.R. Wilshaw, and R.I. Todd, J. Euro. Ceram. Soc. 33 (2013) 2811–2816

[8] Salvatore Grasso, Theo Saunders, Harshit Porwal, Omar Cedillos-Barraza, Daniel Doni Jayaseelan, William E. Lee, and Mike John Reece, J. Am. Ceram. Soc., 97 (2014) 2405–2408

[9] Lorena Batista Caliman, Renaud Bouchet, Douglas Gouvea, Priscillia Soudant, and Marlu César Steilb, J. Euro. Cera. Soc., 36 (2016) 1253–1260

[10] R.I. Todd, E. Zapata-Solvas, R.S. Bonilla, and T. Sneddon, P.R. Wilshaw J. Euro. Cera. Soc., 35 (2015) 1865-

[11] Y. Dong and I.-W Chen, J. Am. Ceram. Soc., 98 (2015) 3624-3627.

[12] João Gustavo Pereira da Silva, Hazim Ali Al-Qureshi, Frerich Keil, Rolf Janssen, J. Euro. Cera. Soc., 36, (2016) 1261-1267.

[13] Rishi Raj, J. Euro. Cera. Soc., 32 (2012) 2293–2301

[14] Hasti Majidi and Klaus van Benthem, Phy. Rev, Letter, 114 (2015) 195503 1-5

[15] Y. Zhang and J. Luo, Scr. Mater., 106 (2015) 26-29

[16] S.K. Jha, J.M. Lebrun, K.C. Seymour, W.M. Kriven, and R. Raj, J. Euro. Cera. Soc., 36 (2016) 257–261

[17] S.L. Kang, Sintering: Densification, Grain Growth and Microstructure, Elsevier, 2005, Charpter 5.

[18] Jenqdaw Wang and Rishi Raj, J. Am. Ceram. Soc., 73 (1990) 1172-1175

[19] T. K. Gupta, W. G. Carlson, J of Materials Science 20 (1985) 3487-3500

[20] Seung-Wan Kim, Suk-Joong L. Kang, and I-Wei Chen, J. Am. Ceram. Soc., 96 (2013)1398–1406

[21] S.K. Jhaa, J.M. Lebruna, K.C. Seymourb, W.M. Krivenb, and R. Raj, J. Euro. Cera. Soc., 36 (2016) 257-261

[22] E. K. Akdogan, I. Savklıyıldız, H. Bicer, W. Paxton, F. Toksoy, Z. Zhong, and T. Tsakalakos, J. of App. Phy., 113 (2013) 233503

# Chapter 7. Observation of an unusual case of triple-line instability

## 7.1. Introduction

It is well known in the classical physical metallurgy that the ratio of the grain boundary (GB) energy ($\gamma_{gb}$) and surface energies ($\gamma_s$) is approximately 1/3 (in the range of 0.2 to 0.5) for most pure metals [1]. In multicomponent alloys, adsorption (segregation) of the solutes (or impurities) can often reduce both $\gamma_{gb}$ and $\gamma_S$ according to the Gibbs adsorption theory [2]. The Rice-Wang model for GB embrittlement suggests that adsorption reduces $2\gamma_S$ more than $\gamma_{gb}$, resulting in a decrease in the work of adhesion ($2\gamma_S$ - $\gamma_{gb}$ assuming isotropic $\gamma_S$, which represents the difference in the equilibrium interfacial energies; it differs from, but is correlated with, the actual work of separation) [3]. This also implies that adsorption would likely increase the ratio of $\gamma_{gb}/\gamma_S$. Practically, it is uncommon (but theoretically possible) to observe cases where $\gamma_{gb}/\gamma_S > 1$. Thermodynamically, the ratio of $\gamma_{gb}/\gamma_S$ must be < 2; otherwise, a GB is no longer stable and will spontaneously separate to two free surfaces.

A series of recent *Viewpoint* articles emphasized the importance of understanding and controlling triple lines/junctions (*a.k.a.* triple-grain junctions in a polycrystal where three GBs meet) [4-6]. Thermodynamically, if $\gamma_{gb}/\gamma_s > \sqrt{3} \approx 1.73$, a triple line is no longer stable (for isotropic $\gamma$'s and ignoring torques and triple-junction line energies), as shown in Fig. 7.1. This may be viewed as a case of triple-line wetting by a vapor phase, but it is more complex than a usual case

of wetting since the triple-grain junction line is replaced with three new triple lines in addition to the formation of three new solid-gas surfaces (Fig. 7.1). This letter reports such a case of triple-line instability; here, the critically large ratio of $\gamma_{gb}/\gamma_S$ is likely induced by the strong interfacial adsorption of Bi, along with S impurities, in electrodeposited Ni. The occurrence of this unusual high-temperature capillary phenomenon can significantly affect the microstructural stability and corrosion resistance.

## 7.2. Experimental

For the first batch of experiments, electrodeposited Ni foils were prepared following a pulsed electrodeposition procedure [7] with minor modifications. Prior to electrodepostion, the Cu substrates and Pt counter electrode were ground with SiC films (up to 800 grits), fine polished by 1.0-μm $Al_2O_3$ colloidal suspensions, and cleaned in acetone. A bath composed of $NiSO_4 \cdot 6H_2O$ (300 g/L), $NiCl_2 \cdot 6H_2O$ (45 g/L) and $H_3BO_3$ (45 g/L), with additives of saccharine (5 g/L) and sodium lauryl sulfonate (0.25 g/L), was used. Each deposition was conducted for 30 min with continuous stirring, and the bath temperature was maintained at 65 ± 1 °C. The effective current density was kept at 0.1 A/cm$^2$ (by using an “on” time of 5 ms with the current density of 0.4 A/cm$^2$, followed by an “off” time of 15 ms, periodically). The thickness of the electrodeposited Ni was ~40 μm (Fig. 7.2). The as-deposited specimens were characterized by X-ray diffraction (XRD) using a Rigaku (Tokyo, Japan) RU-200BH diffractometer operating at 40kV and 100 mA, which revealed no impurity phase (Fig. 7.2). After the electrodeposition, the Cu

substrates were dissolved in aqueous solutions containing $CrO_3$ (250 g/L) and sulfuric acid (15 cc/L), and free-standing electrodeposited Ni foils were used in the subsequent experiments.

In the second batch of controlled experiments, two sets of high-purity Ni specimens (99.9945 at. %; purchased from Alfa Aesar), with and without pre-treatment to dope S, were used to determine the effects of impurities. The S-doped specimen was made by annealing high-purity Ni in a covered container together with S powder (without direct contact) at 400 °C for 1 h in a horizontal tube furnace flowing under Ar + 5 (mol.) % $H_2$; subsequently, surface S residuals were ground off and annealed again at 600 °C for 1 h in Ar + 5 % $H_2$ to homogenize the S. All specimens were slightly ground, fine polished and cleaned prior to additional experiments.

Subsequently, the Ni specimens and a small amount of Bi powder were placed on the opposite sides of a covered alumina boat (without direct contact), and isothermally annealed at the desired temperature for 4 h in a flowing Ar + 5 % $H_2$ gas. For comparison, Ni specimens were also annealed at identical conditions without Bi powder/vapor. The annealed specimens were characterized by using a Philips XL30 field emission scanning electron microscope (SEM).

### 7.3. Results and discussion

Fig. 7.3 shows SEM images of selected representative surfaces of the electrodeposited Ni specimens annealed in the Bi vapor at various temperatures. After annealing at 700 °C, all 230 triple junctions examined were stable (*a.k.a.*

free of open channels; Fig. 7.3(a) and (b)). After annealing at 800 °C, open channels were observed to form at 20 out of 89 (or ~23% of) triple junctions examined (Fig. 7.3 (c) and (d); Fig 7.4). After annealing at 900 °C, open channels were observed to form at 85 out of 326 (or ~26% of) triple junctions examined (Fig. 7.3 (e) and (f); Fig. 7.5). These open channels have dimensions ranging from 200 nm to 1 μm (Fig. 7.3 (d) & (f); Figs. 7.4-Fig.7.5); further careful examination with SEM cannot determine the bottoms of the channels, indicating they are deep (beyond the SEM depth of field). They represent a case of triple-line instability at the annealing temperature, as schematically illustrated in Fig. 7.1. Moreover, this triple-line instability is likely anisotropic since it was only observed at ~1/4 of triple junctions on the surfaces. Grooving at GBs and surface faceting were also evident (Fig. 7.3; Figs. 7.4-Fig.7.5). In contrast, all the 363 triple junctions examined were stable in the electrodeposited Ni specimens annealed at 700-900 °C without the Bi powder/vapor, as shown in Fig. 7.6 and summarized in Table 7.1. This comparison implies that the occurrence of the triple-line instability was induced by the presence of the Bi vapor; presumably, Bi atoms adsorb/segregate at both surfaces and GBs at the annealing temperature.

It is well known that electrodeposited Ni has a low purity (~99.5 %) [8, 9]. Thus, a second batch of experiments using high-purity Ni was conducted. Surprisingly, SEM micrographs showed that all 75 triple junctions examined in the high-purity Ni specimens annealed at 800 and 900 °C in Bi vapors were stable (free of open channels), as shown in Fig. 7.7 and Table 7.1, despite the occurrence of some grooving and faceting (Fig. 7.7). This result suggests that the

presence of impurities in electrodeposited Ni was important for the occurrence of this triple-line instability.

Since S is known as a major impurity element in electrodoposited Ni that strongly segregates to both surfaces and GBs [8, 9], we hypothesize that the presence of S impurities (as a co-dopant in addition to Bi) is essential for the occurrence of this triple-line instability. Indeed, similar triple-line instability was observed in a high-purity Ni specimen that was pre doped with S (using the procedure described above) and subsequently annealed in the Bi vapor at 900 °C (Fig. 7.8 and Fig. 7.9). The dimensions of these open channels was greater (> 1 μm; Fig. 4), and it occurred at a smaller fraction (~7.5%) of the triple junctions; these might have resulted from the larger grain size and inhomogeneous S distribution. Nonetheless, this controlled experiment suggested that S co-doping could induce triple-line instability. Although no prior study investigated the effects of impurities on triple-line wetting/instability, a recent study did reveal the presence of minor impurities in Ni can significantly change GB wetting and liquid metal penetration behaviors in Ni-Bi (the primary phases are underlined) [10].

This unusual phenomenon of triple-line instability (wetting by a gas phase) is likely related to the formation of a bilayer complexion (a type of “2-D interfacial phases” that was more rigorously named as “complexions” to emphasize that they are not “phases” according to the rigorous Gibbs definition [11-15]; it is important to differentiate complexions, which are interfacial chemical/structural states that are *thermodynamically two-dimensional*, from precipitated thin layers of secondary bulk/3-D phases at GBs) that was recently observed in Ni-Bi [16],

as well as in Cu-Bi [17] and Si-Au [18]. The atomic structure of this bilayer complexion in Ni-Bi is schematically illustrated in Fig. 7.10; specifically, one monolayer of Bi adsorbs on each of the Ni grain surfaces strongly, and the two adsorbed Bi layers bonded weakly. In a phenomenological thermodynamic model that is schematically illustrated in Fig. 7.10 [16] (the basic concepts of which were verified by quantum-mechanical calculations [19, 20]), the excess free energy of a general Ni GB with bilayer adsorption of Bi can be expressed as:

$$\gamma_{gb}^{(bilayer)} = 2\gamma_S^{(mono-Bi)} - \Delta\gamma^{(Bi-Bi)} + \Delta\gamma^{(re.)}, \tag{7.1}$$

where $\gamma_S^{(mono-Bi)}$ is the excess free energy of a free surface with a monolayer adsorption of Bi, $\Delta\gamma^{(Bi-Bi)}$ represents the bonding energies (per unit area) between two adsorbed Bi layers, and $\Delta\gamma^{(re.)}$ represents the effects of relaxation and reconstruction. Since Ni-Bi bonds are strong and Bi-Bi bonds are weak, there is little relaxation ( $\Delta\gamma^{(re.)}$ is likely relatively small and equilibrium $\gamma_S \approx \gamma_S^{(mono-Bi)}$ ). Thus, to the first order of approximation, we estimate:

$$\frac{\gamma_{gb}}{\gamma_S} \approx 2 - \frac{\Delta\gamma^{(Bi-Bi)}}{\gamma_S}. \tag{7.2}$$

Since the Bi-Bi bonds are weak, $\Delta\gamma^{(Bi-Bi)}$ is small; consequently, $\gamma_{gb}/\gamma_S$ can be critically large.

However, no triple-line instability in the high-purity Ni specimens implies that $\gamma_{gb}/\gamma_S$ should still be less than $\sqrt{3}$ for Bi-doped Ni (Fig. 7.1 and Fig. 7.3). Unstable triple-lines were only observed in Bi and S co-doped Ni, where both S

and Bi are known to strongly segregate at surfaces and GBs. The presence of S impurities (co-dopants) can further reduce the GB and surface energy of Bi-doped Ni according to the Gibbs isotherm:

$$\frac{d\gamma}{d\mu^{(S)}} \approx -\Gamma^{(S)}, \tag{7.3}$$

where $\mu^{(S)}$ and $\Gamma^{(S)}$, respectively, are the chemical potential and GB excess, respectively, of S. $\gamma$ can be either surface or GB energy. Analogous to the Rice-Wang model of GB embrittlement (assuming $\Gamma_{gb}^{(S)} \approx 2\Gamma_S^{(S)}$, which is an approximation here), segregation of the S co-dopants will reduce $2\gamma_S$ more than $\gamma_{gb}$ because the surface segregation enthalpy is generally greater (more negative) than GB segregation enthalpy. Thus, it is possible that co-segregation of S further increases the ratio of $\gamma_{gb}/\gamma_S$ to $> \sim\sqrt{3}$ to induce triple-line instability.

In the current case, open channels were only observed at a fraction of triple lines/junctions (Table 7.1), which can be explained by anisotropy in the interfacial energies (both $\gamma_{gb}$ and $\gamma_S$). For an isotropic case, the value of $\gamma_{gb}/\gamma_S$ can be measured by the dihedral angles at GB grooves. Unfortunately, the faceting and anisotropy make such quantitative measurements infeasible in the current case. Nonetheless, severe grooving was observed (Figs. 7.8 and 7.9), indicating large $\gamma_{gb}/\gamma_S$ ratios. A large $\gamma_{gb}/\gamma_S$ ratio is correlated with a low GB cohesion and severe GB embrittlement. In fact, it is known that both S and Bi cause significant GB embrittlement of Ni [8, 9, 16, 19-21].

## 7.4. Conclusions

In summary, an unusual high-temperature capillary phenomenon of triple-line instability (wetting by a gas phase to form open channels) was reported. While triple-line wetting by liquid phases at high temperatures was observed for a small number of systems, including AlN-$Y_2O_3$ [22], $SrTiO_3$-$La_2O_3$ [23], ZnO-$Bi_2O_3$ [24], W-Ni [25] and Ni-Bi [16], this is the first report of triple-line wetting by a gas phase, which is rare because it requires a critically large $\gamma_{gb}/\gamma_S$ ratio ($\gamma_{gb}/\gamma_S > \sqrt{3}$ with an isotropic approximation, vs. $\gamma_{gb}/\gamma_S \approx 1/3$ for pure metals). This unusual triple-line instability is likely resulted from strong interfacial segregation of both Bi and S. Specifically, it could be explained from the formation of a unique bilayer complexion in Ni-Bi and the effects additional co-segregation of S. This phenomenon occurs concurrently with severe GB embrittlement [8, 9, 16, 19-21], and it can significantly impact on the microstructural stability and corrosion resistance.

Chapter 7, in full, is a reprint of the material “Observation of an unusual case of triple-line wetting by a gas phase” as it appears in the Scripta Materialia, Yuanyao Zhang, Jian Luo, Scripta Materialia, 2014, 88, 45-48. The dissertation author was the primary investigator and author of this paper. All experiments and data analysis were performed by the author.

Table 7.1 Summary of experimental observations of triple line instability.

| **Specimen** | **Temperature** | **Environment (Vapor)** | **No. of triple junctions examined** | **No. of open channels observed** | **Percentage of open channels** |
|---|---|---|---|---|---|
| **Electrodeposited Ni** | 700 °C | w/o Bi | 50 | 0 | 0% |
| | | w/ Bi | 230 | 0 | 0% |
| | 800 °C | w/o Bi | 70 | 0 | 0% |
| | | w/ Bi | 89 | 20 | ~22% |
| | 900 °C | w/o Bi | 243 | 0 | 0% |
| | | w/ Bi | 326 | 85 | ~26% |
| **High-Purity Ni w/o S** | 800 °C | w/ Bi | 35 | 0 | 0% |
| | 900 °C | w/ Bi | 40 | 0 | 0% |
| **High-Purity Ni pre doped w/ S** | 900 °C | w/ Bi | 80 | 6 | ~7.5% |

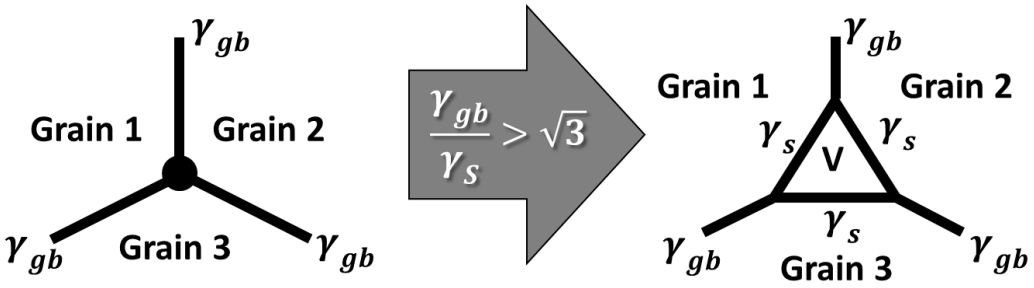


Figure 7.1 A triple-grain junction line is unstable if $\gamma_{gb}/\gamma_s > \sqrt{3}$ for a simplified case of isotropic interfacial energies. This instability condition ignores the contributions of triple-junction line energies because the open channels are > 100 nm in their dimensions, but the triple-junction line energies can be critically important during the nucleation stage of this instability.

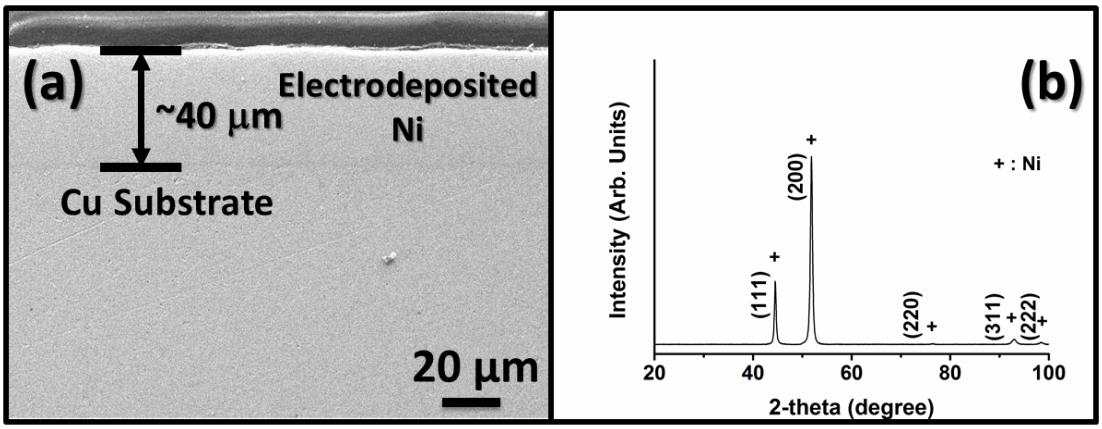


Figure 7.2 (a) A representative cross-sectional SEM micrograph of electrodeposited Ni on a Cu substrate. (b) An XRD pattern of an electrodeposited Ni foil. The grain size of the as-deposited Ni was calculated to be ~18 nm based on XRD peak broadening using the Scherrer Equation; a NIST $LaB_6$ standard specimen was measured to correct the instrumental line broadening effect.

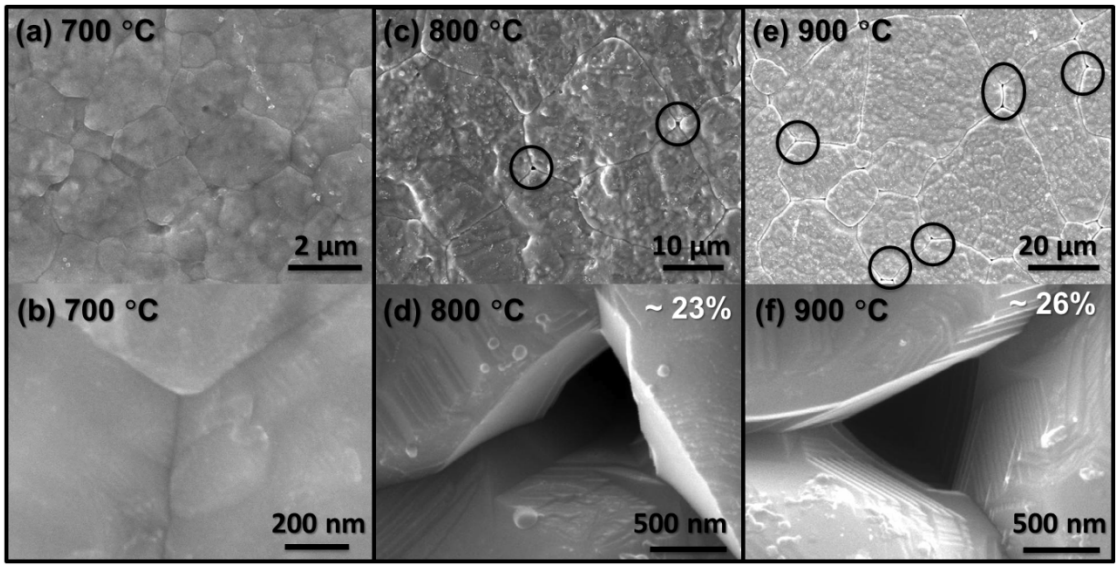


Figure 7.3 Representative secondary electron SEM micrographs of electrodeposited Ni specimens annealed in the Bi vapor at (a, b) 700 °C, (c, d) 800 °C, and (e, f) 900 °C, respectively, for 4 h. All triple junctions examined were stable at 700 °C; open channels were observed for ~1/4 of the triple junctions in specimens annealed at 800 °C and 900 °C.

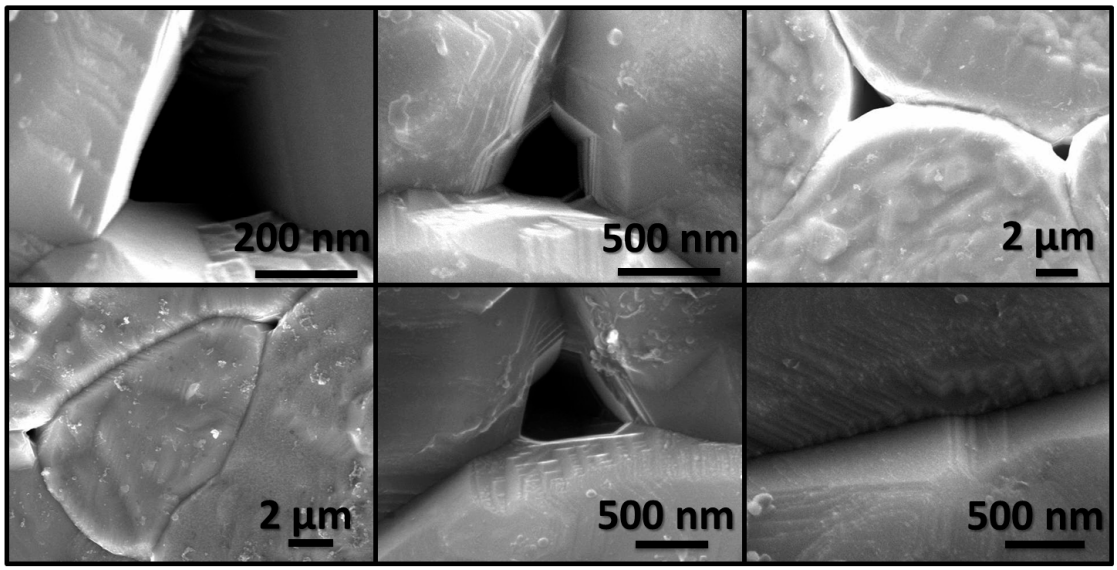


Figure 7.4 Additional SEM micrographs of the electrodeposited Ni specimen annealed in the Bi vapor at 800 °C.

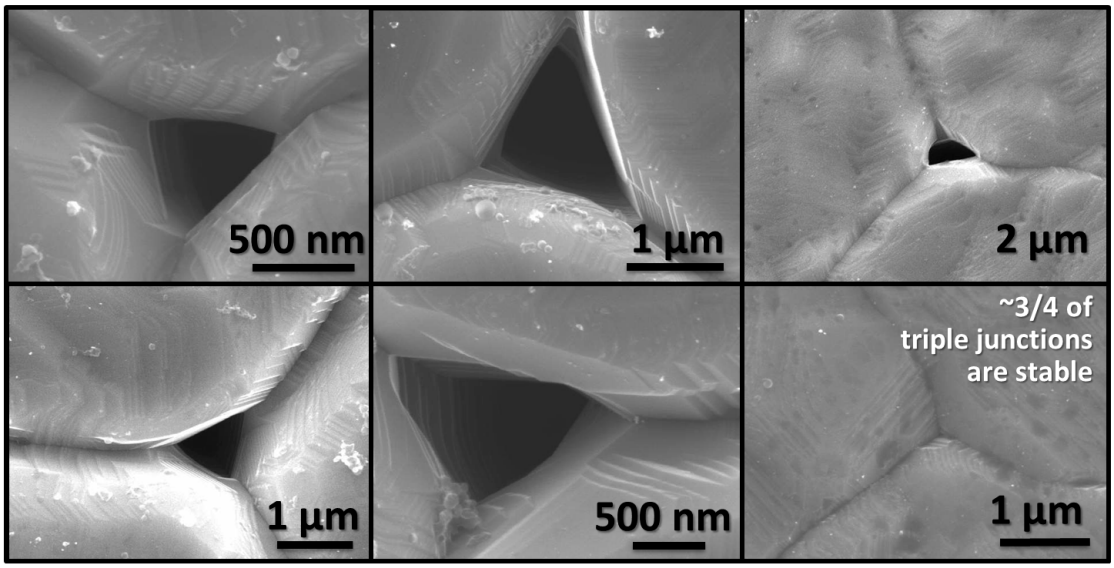


Figure 7.5 Additional SEM micrographs of the electrodeposited Ni specimen annealed in the Bi vapor at 900 °C.

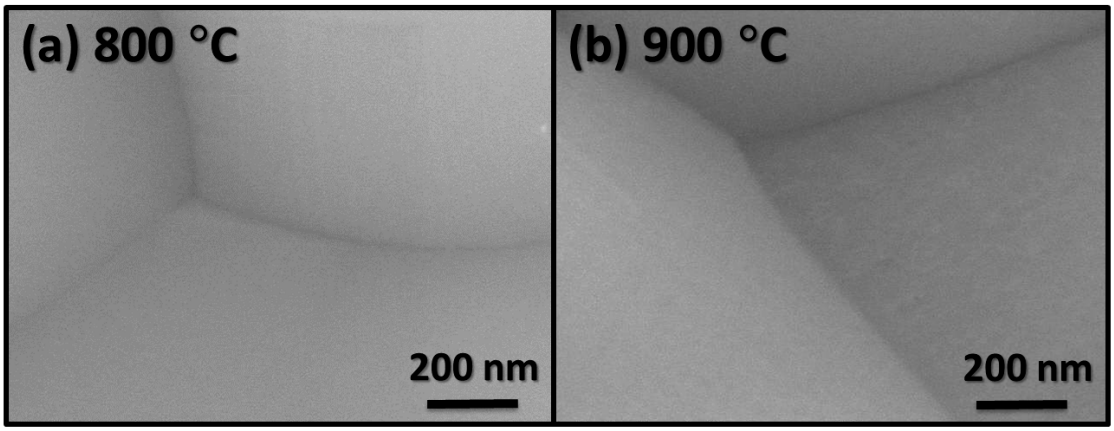


Figure 7.6 SEM micrographs of representative triple junctions in the electrodeposited Ni specimens annealed at (a) 800 °C and (b) and 900 °C, respectively, without Bi vapor; all triple junctions were stable (free of open channels).

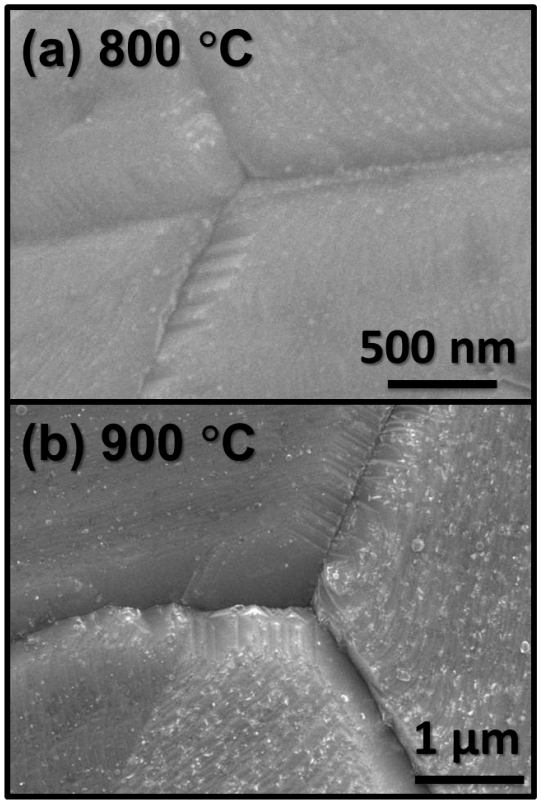


Figure 7.7 SEM micrographs of typical triple junctions of high-purity Ni specimens annealed in Bi vapors at (a) 800 °C and (b) 900 °C, respectively, in which all triple junctions examined were stable.

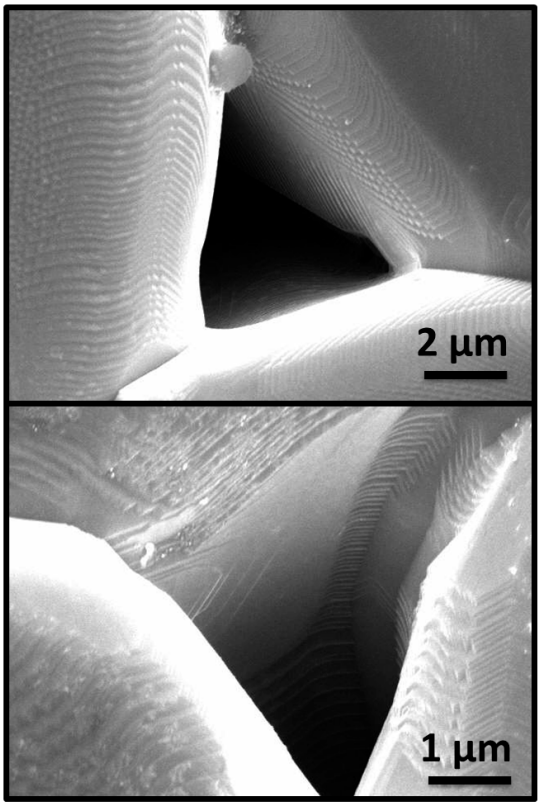


Figure 7.8 SEM micrographs of triple-line instability observed in a high-purity Ni specimen that was first doped with S in a pre-treatment and subsequently annealed in the Bi vapor at 900 °C.

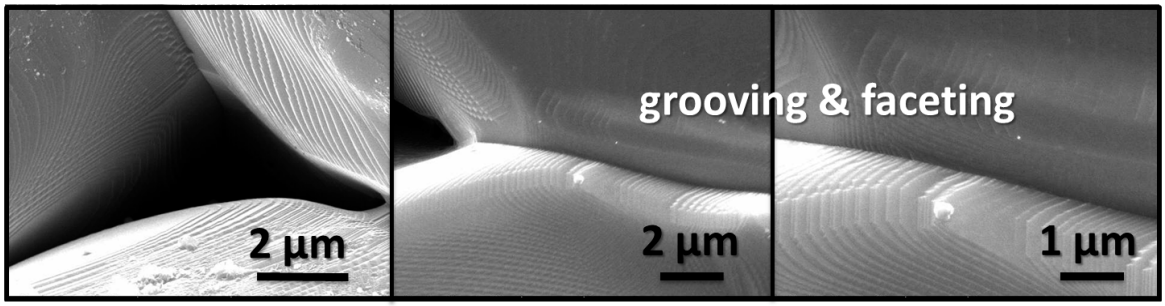


Figure 7.9 Additional SEM micrographs of a high-purity Ni specimen that was first doped with S in a pre-treatment and subsequently annealed in the Bi vapor at 900 °C.

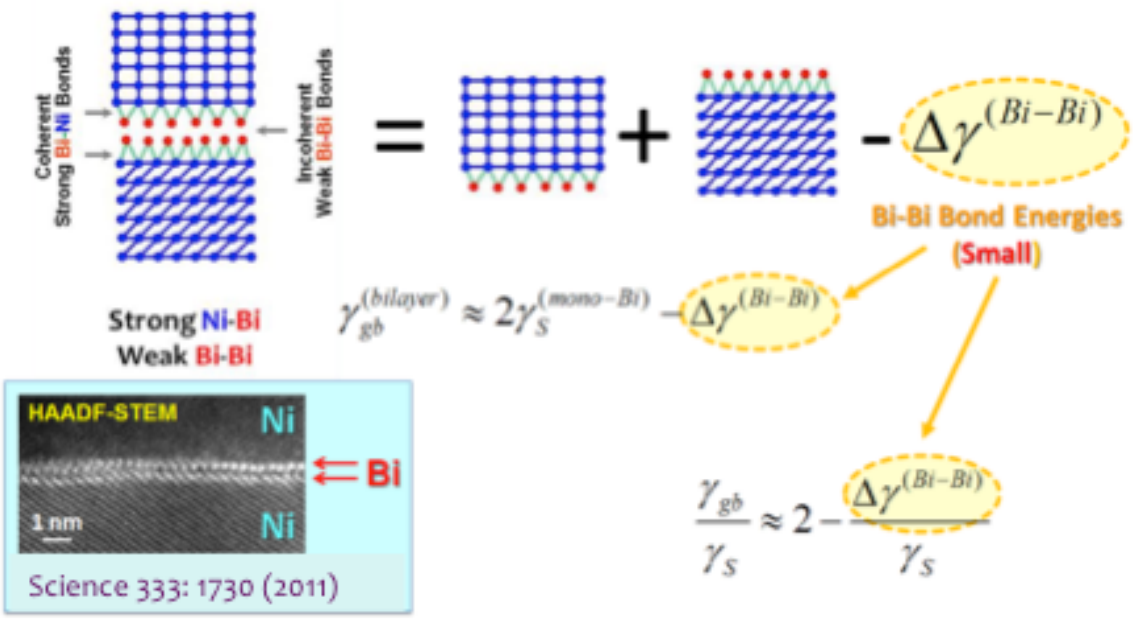


Figure 7.10 A phenomenological thermodynamic model for a bilayer complexion. A complexion is a true “2-D interfacial phase” or an equilibrium or metastable interfacial chemical/structural state that is thermodynamically two-dimensional formed ubiquitously at the general grain boundaries in Bi-doped Ni [16]. Here, the relaxation and reconstruction of the surfaces are ignored in a first-order approximation.

**References:**

[1] D. A. Porter and K. E. Easterling, Phase Transformation in Metals and Alloys, 2nd ed. CRC Press, Taylor & Francis Group, Boca Raton, Flordia, 1992.

[2] P. Wynblatt and D. Chatain, Metall. Mater. Trans. 37A (2006) 2595-2620.

[3] J. R. Rice and J.-S. Wang, Mater. Sci. Eng. A107 (1989) 23-40.

[4] A. H. King, Scripta Mater. 62 (2010) 889-893.

[5] G. Gottstein, L. S. Shvindlerman and B. Zhao, Scripta Mater. 62 (2010) 914-917.

[6] W. C. Carter, M. Baram, M. Drozdov and W. D. Kaplan, Scripta Mater. 62 (2010) 894-898.

[7] A. M. Elsherik and U. Erb, J. Mater. Sci. 30 (1995) 5743-5749.

[8] X. F. Zhang, T. Fujita, D. Pan, J. S. Yu, T. Sakurai and M. W. Chen, Mater. Sci. Eng. A 527 (2010) 2297-2304.

[9] Y. M. Wang, S. Cheng, Q. M. Wei, E. Ma, T. G. Nieh and A. Hamza, Scripta Mater. 51 (2004) 1023-1028.

[10] K. M. Asl and J. Luo, Acta Mater. 60 (2012) 149-165.

[11] P. R. Cantwell, M. Tang, S. J. Dillon, J. Luo, G. S. Rohrer and M. P. Harmer, Acta Mater. 62 (2014) 1-48.

[12] S. J. Dillon, M. Tang, W. C. Carter and M. P. Harmer, Acta Mater. 55 (2007) 6208-6218.

[13] M. P. Harmer, Science 332 (2011) 182-183.

[14] W. D. Kaplan, D. Chatain, P. Wynblatt and W. C. Carter, J. Mater. Sci. 48 (2013) 5681-5717.

[15] M. Tang, W. C. Carter and R. M. Cannon, Phys. Rev. B 73 (2006) 024102.

[16] J. Luo, H. Cheng, K. M. Asl, C. J. Kiely and M. P. Harmer, Science 333 (2011) 1730-1733.

[17] A. Kundu, K. M. Asl, J. Luo and M. P. Harmer, Scripta Mater. 68 (2013) 146-149.

[18] S. Ma, K. Meshinchi Asl, C. Tansarawiput, P. R. Cantwella, M. Qi, M. P. Harmer and J. Luo, Scripta Mater. 66 (2012) 203-206.

[19] J. Kang, G. C. Glatzmaier and S. H. Wei, Phys. Rev. Lett. 111 (2013) 055502.

[20] Q. Gao and M. Widom, arXiv:1312.3362 (2014).

[21] N. Marie, K. Wolski and M. Biscondi, Scripta Mater. 43 (2000) 943-949.

[22] G. Pezzotti, A. Nakahira and M. Tajika, J. Eur. Ceram. Soc. 20 (2000) 1319-1925.

[23] Y. Furukawa, O. Sakurai, K. Shinozaki and N. Mizutani, J. Ceram. Soc. Jpn. 104 (1996) 900-903.

[24] M. Elfwing, R. Osterlund and E. Olsson, J. Am. Ceram. Soc. 83 (2000) 2311-2314.

[25] V. K. Gupta, D. H. Yoon, H. M. Meyer III and J. Luo, Acta Mater. 55 (2007) 3131-3142.

## Chapter 8. Summary and future work

The focus of this research is to figure out the mechanisms of flash sintering, which is novel sintering technique that has huge advantages on energy efficient and cost effective. A systematic understanding of underlying mechanisms is crucial for the further development of this new sintering method and the selection of materials and processing recipes. We developed the quantitative model to predict onset flash sintering, and it could be an engineering tool to determine processing temperature in future application in industry. We tested our model in ZnO and $TiO_2$ based ceramic, in different starting grain size, different atmospheres, different dopants, and different starting phases. All of our predicted onset flash sintering temperature matches experiment observed onset flash sintering temperature. Another achievement is that high-purity ZnO powder specimens to be flashed sintered to > 97% of the theoretical density with fine grain sizes of ~ 1 μm in ~30 seconds at furnace temperatures of <120 ºC in Ar + 5 mol. % $H_2$, though the melting temperature of ZnO is 1975 ºC and conventional sintering temperature is > 1100 ºC with isothermal sintering for a few hours. In our sintering method, the furnace temperature is 10 times lower (120 ºC vs. 1100 ºC) and sintering processing time is 600 times shorter (30 sec vs. 5 hours). Furthermore, we also probe the mechanisms of densification in flash sintering, at least in ZnO system. Actual specimen temperature or the additional heat from Joule heating, and rapid heating profile are the main effects of densification,

though we do aware that electric field could make contributions in densification, they are not main effects at least in ZnO system. In addition, we observed some interesting phenomenon after flash sintering, such as enhanced coarsening and/or grain growth at the anode side, aligned growth of single-crystalline ZnO rods and fibers towards the anode direction, etc. These interesting microstructure evolution could be attributed to the electric field effect during flash sintering. Last but not the least, an unusual high-temperature capillary phenomenon of triple-line instability (wetting by a gas phase to form open channels) was reported. This is the first observation of triple-line wetting by a gas phase, which is rare because it requires a critically large $\gamma_{gb}/\gamma_S$ ratio ($\gamma_{gb}/\gamma_S > \sqrt{3}$ with an isotropic approximation, vs. $\gamma_{gb}/\gamma_S \approx 1/3$ for pure metals).

**In the first part** of this thesis, we developed of a model to predict the thermal runaway conditions that are coincidental with the observed onset flash temperatures in ZnO and $TiO_2$ based ceramic. The excellent agreements between the predicted thermal runaway temperatures and observed onset flash temperatures authenticate the key underlying hypothesis, i.e., the flash starts as a thermal runaway for at least ZnO single crystals and powder specimens without the need of introducing an avalanche of non-equilibrium defects, although some non-equilibrium defects may form after the onset of the flash to accelerate the sintering and affect microstructural development; the $Bi_2O_3$ doping leads to the formation of a bulk eutectic liquid or liquid-like interfacial complexion that causes

a discontinuous increase in conductivity to initiate the flash sintering in a similar mechanism.

This model has been tested in flash sintering of ZnO in different atmospheres (Air, Ar, Ar + 5 mol. % $H_2$ and $O_2$), the predicted onset flash sintering temperature and experimental observed onset flash sintering temperature has only 1 degree difference in all these four different situations. The conductivity of ZnO is strongly dependent on oxygen concentration, so the conductivity of ZnO in these four different atmospheres is different, thus onset flash sintering temperature is varied. However, our model could predict onset flash sintering temperature accurately in all these situations.

We further investigated the flash sintering of six $TiO_2$ based specimens with different dopants (un-doped, V-doped vs. N-doped) and initial phases (anatase vs. rutile). Since dopants and starting phase have effects on electric conductivity and microstructure, thus the onset flash sintering is different. In all six cases, the coupled thermal and electric runaway temperatures predicted from the measured specimen conductivities agree well with the observed onset flash temperatures within <5 °C, supporting our quantitative model.

**The second achievement** of my work is that ZnO could be flash sintered at furnace temperature <120 ºC in less than 30 seconds. We are also the first to report application of flash sintering in different atmosphere, and realize that onset flash sintering temperature could be strongly dependent on atmosphere. Specifically, sintering in an inert (reducing) Ar atmosphere decreased the onset

of flash sintering temperature (from 590 ºC in air) to 236 ºC. Sintering in a more reducing hydrogen atmosphere (Ar + 5 mol. % $H_2$) further lowered the onset of flash sintering temperature to 185 ºC. Consistently, sintering in pure $O_2$ increased the onset flash sintering temperature slightly (from 590 ºC in air) to 611 ºC. All these experiments are conducted with a constant electric field of 300 V/cm and current limit of 1 A. The dependence of the onset flash sintering temperature on the atmosphere can be explained from the increased conductivities of ZnO in reducing atmospheres. To further reduce the onset flash sintering temperature and simultaneously increase the densification, we conducted four additional flash sintering experiments of ZnO powder specimens in Ar + 5 mol. % $H_2$ at higher applied electrical fields ($E$ = 500 V/cm and 1000 V/cm) with a greater maximum current limit ($I_{max}$ = 4 A or $J_{max}$ = 153 mA/mm$^2$). Specifically, the onset of flash temperatures were measured in the range of 110 to 130 ºC (with ~20 ºC specimen-to-specimen variations) with the higher applied electric fields. The final sintered densities were measured to be in the range of ~90-98 % of the theoretical density. Two best specimens achieved >97 % of the theoretical density.

**The third achievement** is observation of interesting microstructure evolution after flash sintering. A particular intriguing and interesting observation of this study is represented by the anode-side abnormal grain growth and/or coarsening during the flash sintering of pure ZnO powder specimens (noting that here the term “abnormal grain growth” is used to represent a case of abruptly faster grain growth in the anode side with an overall bimodal grain size

distribution in the specimen); the measured grain sizes are substantially greater in the anode (+) side than those at the cathode (-) sides. When the maximum current was set to be 1 A ($J_{max} \approx 3.9$ A/cm$^2$), the average grain sizes of cathode (-) and anode (+) sides, respectively, were measured to be 0.4 ± <0.1 μm and 0.9 ± 0.1 μm. When the maximum current was set to be 4 A ($J_{max} \approx 15.4$ A/cm$^2$), the disparity increased further. The average grain sizes of the cathode and anode sides, respectively, were measured to be 3.5 ± 1.8 μm and 32.3 ± 5.6 μm, respectively. In this case, there was substantial grain growth at the cathode size (by approximately 8×) and excess grain growth at the anode side (by approximately 80×); in the final state, the grains are about 10× larger at the anode side. We propose that in the current case of ZnO, electrons accumulate at the anode size (due to the positive electric potential) and interact with surfaces and/or grain boundaries to enhance the interfacial transport rates via an oxidation reaction that increases the local cation vacancy concentration, which subsequently accelerates the coarsening of particles and/or grain growth during the flash sintering. However, the grain size after flash sintering in Ar + 5 mol. % $H_2$ is uniform between cathode and anode side even with a higher electric field of 500 V/cm and 1000 V/cm, and same current limit of 4 A ($J_{max} \approx 15.4$ A/cm$^2$) comparing with flash sintering condition in air. The grain sizes were measured to be 1.0 ± 0.3 μm at the anode side and 0.9 ± 0.3 μm at the cathode side, respectively, for the specimens flash-sintered at 500 V/cm. The grain sizes were measured to be 1.4 ± 0.5 μm at the anode side and 1.3 ± 0.4 μm at the cathode side, respectively, for the specimens flash-sintered at 1000 V/cm. This is

presumably due to a reduction effect in Ar + 5 mol. % $H_2$ that offsets the selected grain boundary oxidation at the anode size in air, as proposed as the underlying mechanism for the anode-side grain boundary.

At the high current density of $J_{max} \approx 15.4$ A/cm$^2$ ($I_{max} = 4$ A), the growth of aligned single-crystalline rods and fibers was observed in the pure ZnO powder specimen, which presumably occurred at the cracks. It should be pointed out that the growth of ZnO rods may be related to local melting at cracks (therefore liquid-phase growth locally). Nonetheless, it is interesting to note that the alignment of ZnO rods does show an electric field effect. It is also interesting to note that all ZnO fibers and rods grew towards to the anode direction.

**The fourth achievement** is that probing the densification mechanisms of flash sintering. Joule heating and rapid heating rate are the main effects in densification during flash sintering, at least for ZnO system. Using different current limits, which determine the specimen temperature in flash sintering, to figure out the relationship between densification rate and specimen temperature. It suggests that Joule heating is at least one important factor in densification. Moreover, we conducted a critical comparative study to show that rapid thermal annealing (RTA) and flash sintering conducted with similar T(t) profiles achieved similar densification and grain growth rates, which suggested that the heating profile is one controlling factor for fast densification for (at least) pure ZnO, while we do recognize the electric fields/currents can have appreciable influences on sintering and microstructural evolution.

From our results, relative density could reach more than 95% when the specimen temperature reaches 1100 °C, no matter how the specimen temperature reached (conventional sintering, flash sintering and RTA). However, if the specimen temperature is ~1000 °C, the relative densities in these three sintering methods (flash sintering, conventional sintering, and RTA) are all lower than 90%. Specimen temperature is the main effect in densification, higher temperature and higher densification no matter with or without electric field.

In addition, controlled flash sintering by limiting specimen temperature ramping rate (dT/dt) through limiting current ramping rate after flash was conducted. We demonstrated that the densification was lower if we slowed down the effective heating rate; even if the case of controlled flash sintering has more total Joule heating, the total densification is less. Thus, a high heating rate (dT/dt) must be a critical factor that leads to fast densification. We further hypothesize that a high heating rate (dT/dt) can affect the sintering kinetics by preventing initial coarsening to keep a high densification driving force and possibly producing non-equilibrium defects (with conceivable field/current influences).

More recently, we conducted a critical comparative study to show that rapid thermal annealing (RTA, with radioactive IR heating, using an ultra-high heating ramp rate 200 °C/sec) and flash sintering conducted with similar T(t) profiles achieved similar densification and grain growth rates, suggesting that the heating profile is one controlling factor for fast densification (at least) for pure ZnO.

**Last but not the least**, The Bi vapor penetrates along the triple lines in the electrodeposited Ni to form open channels at 800 and 900 °C. This is interpreted as a case of triple-line wetting by a gas phase, which has never been reported before. This unusual wetting phenomenon is related to the formation of a bilayer complexion and grain boundary embrittlement in the Ni-Bi system. Further controlled experiments using high-purity Ni specimens with and without S doping suggest that the presence of S impurities is essential for the occurrence of this wetting phenomenon. This discovery has practical importance for understanding and controlling the microstructural stability and corrosion resistance.

**For the future study**, the densification mechanisms of flash sintering should be further investigated besides ZnO system. There might be some difference between ion conductor and electron conductor, so the electric filed might have other effects on ion conductor materials, thus densification mechanisms in ion conductor materials might be different. Furthermore, the microstructure evolution under electric field could be further investigated. In addition, the final material's properties after flash sintering could be researched, as far as I know, no literature reports any comparison of materials properties between flash sintering and conventional sintering. But I believe that it is very important in future application of this sintering method.